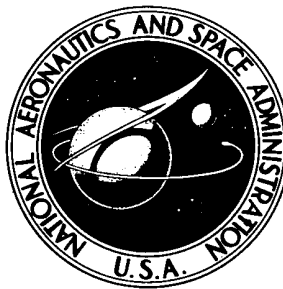


**NASA TECHNICAL NOTE**



**NASA TN D-7328**

**NASA TN D-7328**

**STEADY-STATE AND DYNAMIC PRESSURE  
PHENOMENA IN THE PROPULSION SYSTEM  
OF AN F-111A AIRPLANE**

*by Frank W. Burcham, Jr., Donald L. Hughes,  
and Jon K. Holzman*

*Flight Research Center  
Edwards, Calif. 93523*

1. Report No. NASA TN D-7328		2. Government Accession No.		3. Recipient's Catalog No.	
4. Title and Subtitle STEADY-STATE AND DYNAMIC PRESSURE PHENOMENA IN THE PROPULSION SYSTEM OF AN F-111A AIRPLANE				5. Report Date July 1973	
				6. Performing Organization Code	
7. Author(s) Frank W. Burcham, Jr., Donald L. Hughes, and Jon K. Holzman				8. Performing Organization Report No. H-741	
9. Performing Organization Name and Address NASA Flight Research Center P. O. Box 273 Edwards, California 93523				10. Work Unit No. 136-13-08-00-24	
				11. Contract or Grant No.	
12. Sponsoring Agency Name and Address National Aeronautics and Space Administration Washington, D. C. 20546				13. Type of Report and Period Covered Technical Note	
				14. Sponsoring Agency Code	
15. Supplementary Notes					
16. Abstract  <p>Flight tests were conducted with two F-111A airplanes to study the effects of steady-state and dynamic pressure phenomena on the propulsion system. Analysis of over 100 engine compressor stalls revealed that the stalls were caused by high levels of instantaneous distortion. In 73 percent of these stalls, the instantaneous circumferential distortion parameter, <math>K_\theta</math>, exhibited a peak just prior to stall higher than any previous peak. The <math>K_\theta</math> parameter was a better indicator of stall than the distortion factor, <math>K_D</math>, and the maximum-minus-minimum distortion parameter, <math>D</math>, was a poor indicator of stall. Inlet duct resonance occurred in both F-111A airplanes and is believed to have been caused by oscillations of the normal shock wave from an internal to an external position. The inlet performance of the two airplanes was similar in terms of pressure recovery, distortion, and turbulence, and there was good agreement between flight and wind-tunnel data up to a Mach number of approximately 1.8. Power spectral density plots of compressor face pressures showed generally increasing power levels with increasing Mach number. The frequency and amplitude of the inlet duct buzz data obtained in flight agreed reasonably well with both wind-tunnel and theoretical data.</p>					
17. Key Words (Suggested by Author(s)) Inlet dynamics Compressor stall Instantaneous distortion				18. Distribution Statement  Unclassified - Unlimited	
19. Security Classif. (of this report) Unclassified		20. Security Classif. (of this page) Unclassified		21. No. of Pages 98	
				22. Price* \$3.00	

	Page
INTRODUCTION . . . . .	1
SYMBOLS . . . . .	2
DESCRIPTION OF APPARATUS . . . . .	3
Airplanes . . . . .	3
Propulsion System . . . . .	4
Inlet . . . . .	4
Boundary-layer removal system . . . . .	4
Subsonic diffuser . . . . .	4
Engine . . . . .	5
INSTRUMENTATION . . . . .	5
DATA RECORDING . . . . .	6
DATA REDUCTION . . . . .	6
DATA ANALYSIS . . . . .	6
Instantaneous Parameters . . . . .	6
Pressure recovery . . . . .	7
Distortion factors . . . . .	7
Steady-State Parameters . . . . .	8
Statistical Parameters . . . . .	8
Turbulence factor . . . . .	8
Power spectral density . . . . .	8
Coherence . . . . .	9
Phase angle . . . . .	9
Calculation of statistical parameters . . . . .	9
ACCURACY . . . . .	9
Steady-State Parameters . . . . .	9
Dynamic Pressure Response . . . . .	10
Instantaneous Parameters . . . . .	10
TEST PROCEDURE . . . . .	11
DISCUSSION . . . . .	12
Inlet Performance . . . . .	12
Effect of Mach number . . . . .	12
Effect of angle of attack . . . . .	13
Effect of angle of sideslip . . . . .	13
Effect of mass flow ratio . . . . .	13
Effect of inlet spike and cone position . . . . .	13
Inlet Duct Resonance . . . . .	14
F-111A number 6 duct resonance . . . . .	14
F-111A number 12 duct resonance . . . . .	15
Inlet Duct Buzz . . . . .	16
Engine Compressor Stall . . . . .	17
Steady-state distortion at stall . . . . .	17
Instantaneous distortion at stall . . . . .	17
Comparison of distortion parameters . . . . .	18
Detailed analysis of stalls . . . . .	18
Usefulness of $K_\theta$ , $K_D$ , and $D$ as stall indicators . . . . .	18
Rotating stall . . . . .	19
Reasons for lack of correlation between distortion and stall . . . . .	19

	Page
Rotor Speed Frequencies . . . . .	20
CONCLUSIONS . . . . .	20
REFERENCES . . . . .	22

# STEADY-STATE AND DYNAMIC PRESSURE PHENOMENA IN THE PROPULSION SYSTEM OF AN F-111A AIRPLANE

Frank W. Burcham, Jr., Donald L. Hughes, and Jon K. Holzman  
Flight Research Center

## INTRODUCTION

The pressure phenomena in the propulsion system of supersonic aircraft have great influence on performance. Low levels of inlet pressure recovery result in reduced performance and range. Nonuniformities in pressure, both steady state and dynamic, may result in reduced performance, and in some cases they cause engine compressor stall. The resulting hammer shock waves and inlet buzz generate high structural loads in the inlet. In some aircraft configurations severe propulsion system-airframe interactions may occur. Pressure fluctuations in the engine may also have adverse effects on the aircraft, particularly in afterburning turbofan engines, where afterburner pressure fluctuations may propagate directly to the fan, where they may then affect the inlet flow.

The effects of steady-state pressure distortion are well known, but the importance of dynamic pressure fluctuations was not fully appreciated until Kimzey's work with the J93 engine (ref. 1), which showed that engine stall could occur at very low steady-state distortion levels if the pressure fluctuations were sufficiently severe. At that time the XB-70 airplane, powered by J93 engines, was being flight tested, and a limited number of dynamic pressure measurements were made in the inlet and at the engine compressor face (ref. 2). Early flight tests of the F-111A airplane, which is powered by afterburning turbofan engines, showed numerous compressor stalls at steady-state distortion levels well below the limits established from ground tests. Extensive tests of the TF30 engine in ground facilities using random turbulence generators (refs. 3 and 4) suggested that dynamic pressure fluctuations were causing the stalls. An airjet system at the NASA Lewis Research Center was used to study the effects of periodic and single pulse pressures on the TF30 engine (refs. 5 to 7).

In order to study these dynamic pressure phenomena in flight, the NASA Flight Research Center instrumented and flight tested an early model of the F-111A airplane (refs. 8 to 11). Miniature transducers were installed inside rakes in the inlet to permit adequate frequency response to study the dynamic pressure fluctuations. After these tests were completed, a new type of compressor face rake (ref. 12) was designed which improved the quality of the data. A follow-on program was flown with another early model of the F-111A airplane in which eight of these compressor face rakes were installed, and more accurate and complete data on the inlet were obtained (ref. 13).

This report summarizes the data obtained from both F-111A airplanes. It includes inlet pressure recovery, distortion, and turbulence factor data as functions of Mach number, angle of attack and sideslip, inlet airflow, and inlet geometry. Inlet duct resonances are analyzed, and inlet buzz is described. Engine stall tolerance is presented as a function of corrected airflow, power setting, and compressor bleed position using several distortion parameters. The effects of rotating stall and rotor speed harmonics are also shown.

## SYMBOLS

Physical quantities in this report are given in the International System of Units (SI) and parenthetically in U.S. Customary Units. The measurements were taken in U.S. Customary Units. Factors relating the two systems are presented in reference 14.

A	duct cross-sectional area, $m^2$ ( $in^2$ )
$A_n$	magnitude of Fourier coefficient (see p. 8)
D	maximum-minus-minimum distortion (see p. 7)
$d_o$	duct outer diameter, m (ft)
$d_r$	ring diameter, m (ft)
f	frequency, Hz
h	altitude, m (ft)
i	probe number on a ring
j	number of rings
$K_D$	Pratt & Whitney distortion factor (see p. 7)
$K_\theta$	Pratt & Whitney circumferential distortion factor (see p. 7)
k	number of pressure probes used
M	Mach number
$m/m_0$	mass flow ratio, $w_2/w_\infty$
$N_1$	low pressure compressor rotor speed, rps
$N_2$	high pressure compressor rotor speed, rps
n	integer counter
p	static pressure, $kN/m^2$ ( $lb/in^2$ )
$p_t$	total pressure, $kN/m^2$ ( $lb/in^2$ )
$\Delta p_t$	peak-to-peak total pressure, $kN/m^2$ ( $lb/in^2$ )
q	dynamic pressure, $0.7M^2 p$ , $kN/m^2$ ( $lb/in^2$ )
$Re_i$	Reynolds number index, $\delta/\theta^{1.24}$
r	ring number

$T_t$	total temperature, °K (°R)
$T_u$	turbulence factor (see p. 8)
$t$	time, sec
$w$	airflow, kg/sec (lb/sec)
$X/R$	ratio of distance between inlet cowl lip and spike tip to inlet cowl radius
$\alpha$	angle of attack, deg
$\beta$	angle of sideslip, positive for nose left, deg
$\delta$	ratio of inlet total pressure to standard day sea-level static pressure
$\eta$	total pressure recovery, $p_t/p_{t_\infty}$
$\theta$	ratio of total temperature to standard day sea-level temperature
$\theta_c$	inlet second conical ramp angle, deg
$\theta_i$	circumferential position of a probe, deg (see p. 8)
$\theta_r^-$	circumferential extent of low pressure, deg (see p. 7)

Subscripts:

av	average
max	maximum
min	minimum
peak	peak value
rms	root mean square
ss	steady state (time averaged)
2	compressor face
$\infty$	free stream

## DESCRIPTION OF APPARATUS

### Airplanes

The F-111A airplane (fig. 1) is a twin-engine multimiission tactical fighter with variable sweep wings. With the wings in the forward position, the airplane is capable of short

takeoff and landing and efficient subsonic cruise. With the wings swept, the airplane has supersonic dash capability at sea level and Mach 2.5 capability at altitudes of approximately 15,000 meters (49,000 feet).

The two F-111A airplanes used in these tests were both early models, numbers 6 and 12, and, particularly in their propulsion systems, were not representative of production F-111 airplanes. The only differences between the two airplanes of significance to these tests, which are discussed later, concerned the inlet.

### Propulsion System

The left propulsion system of the F-111A airplane, shown in figure 2, consists of an external compression inlet located under the fixed part of the wing (called the wing glove), a short subsonic diffuser, and an afterburning turbofan engine mounted in the aft fuselage. The engine is equipped with a blow-in-door ejector nozzle.

Inlet.— The air inlet, shown in figure 3, incorporates variable geometry and is an approximately  $90^\circ$  segment of a double cone axisymmetric inlet. The compression spike translates fore and aft with a maximum travel of 46 centimeters (18 inches). The spike consists of two conical ramps: The first ramp is fixed at  $12.5^\circ$ , and the second ramp (called the cone) is variable between  $10.5^\circ$  and  $24^\circ$ . Spike position and cone angle may be controlled independently.

At low speeds the spike is forward and the cone is fully collapsed, as shown in figure 4. At a Mach number of approximately 2.2, the spike is aft and the cone is fully expanded. This configuration is shown in figure 5. Positions of the inlet spike and cone were normally controlled by an automatic inlet control system as a function of local Mach number and engine airflow. Because of developmental changes, the controller schedules, shown in figure 6 for maximum afterburning, were different for the two airplanes. The pilot could move the left inlet spike and cone manually to any desired position on both airplanes.

Both sharp and blunt lip cowl configurations were tested. The sharp lip cowl (fig. 4) was used for all the F-111A number 12 flights. A cowl with a blunted lip (fig. 5) was installed on F-111A number 6 during the tests of this study. In addition to having a more rounded lip, the blunt lip cowl was drooped and cut back 5 centimeters (2 inches) over the inboard part, and it had a slightly larger capture area.

Boundary-layer removal system.— The F-111A inlet incorporated several regions of boundary-layer removal to prevent low energy air from entering the inlet. Fuselage, splitter plate, and wing glove bleed scoops are shown in figure 4. Air captured by these scoops was ducted aft to the engine compartment or dumped overboard. Porous bleed was present on the surface of the cone (figs. 4 and 5). This air was ducted overboard on the upper wing surface. The internal flow paths in the bleed ducts restricted the bleed flow for F-111A number 6 more than for F-111A number 12.

Subsonic diffuser.— The inlet subsonic diffuser, shown in figure 3, turns inboard and changes from a quarter circle near the cowl lip to a full circle at the compressor face in a relatively short length-to-diameter ratio of approximately 3. Vortex generators are installed to minimize wall separation and to improve the pressure distribution at the compressor face. The cross-sectional area distributions for the two airplanes are shown in figure 7. The area of the middle part of the F-111A number 12 duct was greater than in F-111A number 6



and consequently provided more gradual diffusion.

Engine.— Two TF30-P-1 afterburning turbofan engines provide the thrust for the F-111A airplanes tested. Rated thrust is approximately 80,000 newtons (18,500 pounds) with a nominal bypass ratio of 1.0. Rated airflow is 110 kilograms per second (240 pounds per second). Figure 8 is a schematic view of the engine. A three-stage fan and six-stage low pressure compressor are driven by a three-stage turbine at  $N_1$  speed. A seven-stage high pressure compressor is driven by a separate turbine at  $N_2$  speed. The overall compression ratio is 17 to 1.

A five-zone fully modulating afterburner is located in the combined fan and core streams. The primary nozzle area is varied with the degree of afterburning. A blow-in-door ejector nozzle admits external air at low speeds to control nozzle expansion.

The engines in both airplanes had been rematched to increase the compressor stall margin. A sixth-stage compressor bleed was available to further increase the stall margin of the compressor. These bleeds were usually opened by the pilot for supersonic tests.

## INSTRUMENTATION

Figure 9 shows the location of the pressure measurements in the left inlet and engine of the F-111A number 6 airplane. Inlet instrumentation for the F-111A number 12 tests was limited to the eight compressor face rakes. Table 1 lists measurements, sampling rates, and frequency responses for the two airplanes. The instrumentation in F-111A number 6 is described in detail in references 2, 8 to 11, and 15. Miniature transducers were located in the cone rakes, the shock position probe, the duct rakes, and the four diagonally oriented compressor face rakes. Conventional probes connected by tubes to remotely located transducers were installed in the cowl lip rakes, the horizontally and vertically oriented compressor face rakes, and the engine. Differential pressure transducers were used to measure all except internal engine pressures.

The miniature transducers gave good values for dynamic pressures but were subject to large zero shifts due to temperature, and their steady-state levels were not reliable. Reference 9 describes the technique used to correct the absolute levels of the dynamic transducers tested in F-111A number 6. For the F-111A number 12 flight tests, a new type of compressor face rake with in-flight nulling capability was used. The design, fabrication, and in-flight evaluation of these nulling rakes are described in reference 12. Figure 10 is a photograph of eight of these rakes installed on the engine. During the flight tests, the compressor face rakes were nulled by the pilot about once every 30 seconds and before and after each maneuver.

The frequency response of the pneumatic portion of all the inlet pressure measurements was determined. The response of the nulling compressor face rake was flat to 400 hertz, as shown in reference 12. The response of the other pressures is shown in reference 11.

Other instrumentation, also described in reference 11, was used to determine engine compressor speeds, airflow, total temperature, airplane Mach number, altitude, angle of attack and sideslip, inlet spike and cone position, and the reference pressure supplied to the differential transducers.

## DATA RECORDING

All the output signals from the instruments were filtered electrically prior to digitizing to remove high frequencies and to prevent aliasing (ref. 16). Compressor face pressures were filtered using an active Butterworth network with 18-decibel-per-octave rolloff. Cutoff began at approximately 200 hertz, as shown in figure 11.

The filtered signals were digitized by two pulse code modulation (PCM) systems. Each PCM system sampled each of 77 channels sequentially 200 times per second. The compressor face pressures were sampled 400 times per second by recording each pressure on two channels. On the F-111A number 12, 32 of the compressor face pressures were recorded on one PCM system and eight on the other.

Two of the compressor face pressures were also recorded on a wide-band frequency modulation system to permit analog analysis to much higher frequencies. These two channels were filtered, with cutoff beginning at 1000 hertz, prior to recording.

Outputs from the two PCM systems and the frequency modulation system were recorded on an onboard tape recorder. Part of the data were telemetered to the ground for real time data monitoring, flight control, and analysis.

## DATA REDUCTION

Flight tapes containing the digital data were processed by using digital computers. Zero corrections obtained from the nulling rakes were applied, and power supply voltage corrections were made. Calibrations were then applied to convert the digital PCM data into engineering units. Output data were available in the form of measured and calculated parameter listings, plots, and cross plots. The digital data were statistically analyzed by using the digital techniques discussed later. A special program was developed to calculate and plot the parameters of interest for compressor stall analysis. These parameters included pressure recovery, turbulence, and several different distortion parameters. Compressor face maps displaying instantaneous and time-averaged total pressure recovery and turbulence were also available, in addition to the time history plots.

Analog pressure data from the frequency modulation system and digital pressure data which had been converted to analog data were processed by using a hybrid spectrum analyzer. In some cases, this system was used for real time analysis of pressure spectra during flight.

## DATA ANALYSIS

Data in this report are described or analyzed in terms of calculated parameters which are instantaneous, steady state (time averaged), or statistical.

### Instantaneous Parameters

Parameters which are calculated from one sample of data from each pressure will be

termed instantaneous. These parameters are instantaneous pressure recovery and distortion.

Pressure recovery.— The total pressure probes at the compressor face were located at the centers of equal area rings. Therefore, instantaneous total pressure recovery at the compressor face was calculated by adding the instantaneous value of each pressure, dividing by the number of pressures, and dividing by the free-stream total pressure.

$$\eta_{2av} = \frac{1/k \sum_{n=1}^k (p_{t2})_n}{p_{t\infty}}$$

Distortion factors.— Several distortion factors were used to evaluate the engine's compressor stall tolerance. Those discussed in this report are  $D$ ,  $K_D$ , and  $K_\theta$ .

Maximum-minus-minimum distortion,  $D$ : The  $D$  parameter is commonly used because of the simplicity of the calculation.

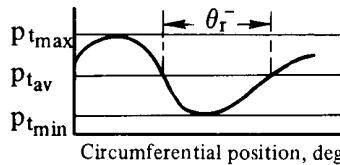
$$D = \frac{p_{tmax} - p_{tmin}}{p_{tav}}$$

Pratt & Whitney distortion factor,  $K_D$ : The distortion parameter  $K_D$  was derived by the engine manufacturer for the TF30 engine. It considers the circumferential extent of distortion and weights distortion near the hub more heavily than that at the tips of the blades.

$$K_D = \frac{\sum_{r=1}^j \left[ \left( \frac{p_{tav} - p_{tmin}}{p_{tav}} \right)_r \left( \frac{d_o}{d_r} \right)_r \theta_r^- \right]}{\sum_{r=1}^j \left( \frac{d_o}{d_r} \right)_r}$$

where

$\theta_r^-$  is the circumferential extent of the largest single pressure depression below  $p_{tav}$ , in degrees, for a particular ring (see sketch below)



All  $K_D$  values presented are adjusted to a Reynolds number index of 1.0, using data supplied by the engine manufacturer.

Pratt & Whitney circumferential distortion parameter,  $K_\theta$ : Further analysis of compressor stalls in the TF30 engine led the engine manufacturer to develop the  $K_\theta$  parameter (ref. 4).

$$K_{\theta} = \frac{\sum_{r=1}^j \left[ \left( \frac{A_n}{n^2} \right)_{\max} \right]_r \frac{p_{t2av}}{q_{av}} \frac{1}{d_r}}{\sum_{r=1}^j \frac{1}{d_r}}$$

The quantity  $A_n$  is the polar magnitude of the  $n^{\text{th}}$  harmonic coefficient, which is the largest in the Fourier series curve fit to the pressure data around the ring in the inlet,  $r$ .

As shown in reference 17, this may be simplified to a form more suitable for computation. For the F-111A rake installation of eight rakes with five probes each, this becomes:

$$K_{\theta} = \left( \frac{1}{4q_{av} \sum_{r=1}^5 \frac{1}{d_r}} \right) \sum_{r=1}^5 \left\{ \frac{1}{d_r} \left\{ \sum_{i=1}^8 [(p_{t2})_i \cos \theta_i]^2 + \sum_{i=1}^8 [(p_{t2})_i \sin \theta_i]^2 \right\} \right\}^{\frac{1}{2}}$$

where

$\theta_i$  is the circumferential position, in degrees, of the pressure probe

#### Steady-State Parameters

The instantaneous parameters displayed wide variations from sample to sample due to high frequency pressure fluctuation. Steady-state parameters were obtained by time averaging many instantaneous data samples, by fairing a smooth line through the data points on a time history or cross plot, or by using sensor installations with sufficient tubing lengths between the probe and the transducer to give frictional damping.

#### Statistical Parameters

The computation of the statistical parameters presented in this report required a considerable amount of data. The parameters are briefly described here; more rigorous definitions are presented in reference 16.

Turbulence factor.— The dynamic activity of a fluctuating pressure is indicated by the turbulence factor,  $Tu$ , which is defined as the standard deviation in total pressure level divided by the average total pressure.

$$Tu = \frac{[(p_{trms})^2 - (p_{tav})^2]^{\frac{1}{2}}}{p_{tav}}$$

Turbulence factor was calculated for each probe, and the average turbulence at the compressor face was determined by averaging the 40 values. The calculations were made from data lengths as short as 0.5 second, or 200 samples, in order to obtain a value immediately prior to stall. For steady-state conditions, up to 5 seconds of data were normally used.

Power spectral density.— Power spectral density is a useful means for detecting predominant frequencies in a fluctuating pressure. It is also useful for comparing data from separate sources, such as flight, wind-tunnel, and ground facility tests. The square root of

the area under the power spectral density curve is proportional to the turbulence factor.

Coherence.— The coherence function is a measure of the degree of interdependence between two pressures as a function of frequency, and therefore it gives an indication of the extent to which the pressure fluctuations at two probes arise at a common source. Coherence ranges from 1.0 (perfect interdependence) to 0 (no interdependence). Coherence values below 0.2 generally indicate no significant interdependence.

Phase angle.— The phase angle function provides an indication of the time delay between two pressures as a function of frequency. For example, two pressures with a common frequency are  $180^\circ$  out of phase at that frequency if at a given time one pressure is at a maximum while the other is at a minimum. The phase angle between pressures is meaningless unless coherence is significant (greater than 0.2).

Calculation of statistical parameters.— The spectral characteristics of the data were calculated by using the fast Fourier transform digital computer program described in reference 11. Wild data points were removed prior to detrending. Detrending was performed to make non-steady-state data more stationary (ref. 16) so that the random data analysis technique could be applied.

Whenever possible, 5.12 seconds of data were used for analysis. Therefore the pressure measurements sampled at 400 samples per second were analyzed with 2048 data points, and the parameters sampled at 200 samples per second were analyzed with 1024 points. In a few cases, data lengths as short as 1.28 seconds were used. In all cases, the number of digital smoothing windows used in the analysis was adjusted to maintain an equivalent 2.5-cycle filter bandwidth. Spectral parameters are valid up to one-half the sampling rate (ref. 16); however, some of the pressures were filtered to less than one-half the sampling rate because of the probe resonant frequencies (table 1).

Power spectral densities calculated from the analog recorded pressures were extended to 1000 hertz, even though probe response was not flat beyond about 400 hertz. Eight seconds of data were processed using an equivalent 2-cycle bandwidth filter.

## ACCURACY

### Steady-State Parameters

The accuracy of the various parameters for F-111A number 6 is given in reference 11. The accuracy of the data for F-111A number 12 is similar except for the compressor face pressures and the parameters calculated from them. Because of the in-flight nulling capability of the compressor face pressures, the accuracy of these parameters is:

Parameter	Estimated error
$p_{t_2}$	$\pm 1.0$ percent
$p_{t_{2av}}$	$\pm 1.0$ percent
$K_D$	$\pm 50$
$D$	$\pm 4$ percent
$K_\theta$	$\pm .05$

## Dynamic Pressure Response

Data system noise and cross talk can be ignored in the analysis of steady-state parameters, since these errors tend to average out. Dynamic analysis, however, is affected by these factors and by the instrument response and time lags introduced by the PCM system.

Instrument response is not a significant factor in this case. The miniature transducers have a usable frequency of at least 5000 hertz with 1 percent accuracy, and the response of the transducer in the compressor face rake was determined to be flat to approximately 400 hertz. The characteristics of the filter (fig. 11) would sharply attenuate frequencies above approximately 300 hertz.

System noise level was evaluated under realistic flight conditions by using pressure data obtained with the compressor face rakes in the null position. Under these conditions, vibration, power supply noise, and data system noise were all present in the same amounts as with the rakes in the normal position.

The noise level which resulted is shown on a power spectral density plot in figure 12. The data are normalized to a typical flight level of  $p_{t_{av}}$ . The noise level is two orders of magnitude below most of the flight data and therefore can usually be ignored. At flight conditions where pressure fluctuations are very small, however, the noise level can be significant, and in those cases the system noise floor is indicated. The spike at the  $N_1$  frequency is probably due to vibration picked up by the transducer.

System cross talk, in which one pressure signal affects other pressure signals, was evaluated when three of the eight compressor face rakes stuck in the null position because of low pressure in the system that actuated the nulling valves. This occurred at high Mach number during an inlet duct resonance, described later, which had a strong peak at approximately 22 hertz. The cross talk effects are evident in figure 13 on the nulled rakes but are more than two orders of magnitude below the actual pressures; and, in fact, except at the 22-hertz resonance frequency and the  $N_1$  frequency, the levels are near the system noise level. Therefore, cross talk errors are generally less than 1 percent, and can be expected to have negligible effect on most power spectral density plots.

There is a digitization error, or minimum resolution, for the pressures due to the use of a 9-bit PCM system which gives a maximum range of 511 counts for the full-scale range of each pressure, or approximately  $0.138 \text{ kN/m}^2$  ( $0.02 \text{ lb/in}^2$ ) per count. The level of pressure fluctuation which might not cause a change of at least 1 count is indicated in figure 13. It is higher than the general level of the nulled pressures but still well below the normal data level.

To summarize the dynamic errors considered so far, cross talk is not usually significant, and system noise and digitization errors are only significant for very low level signals. Such low level signals occur only under steady-state conditions at subsonic and low supersonic speeds and never prior to compressor stall.

## Instantaneous Parameters

To evaluate the accuracy of the instantaneous parameters, not only the accuracy of each pressure but also the possibility of phase shifts between pressures must be considered. The PCM systems sample the 77 channels on each system sequentially and assign the same time

to all the samples. However, it takes 0.005 second to complete 1 cycle, so the last parameter is actually sampled 0.005 second after the first parameter. Supercommutating the pressures by sampling each pressure twice per PCM cycle reduces the maximum time shift to 0.0025 second. However, at 200 hertz this time shift amounts to half of the cycle, or a  $180^\circ$  phase shift, which introduces an apparent out-of-phase condition when in fact an in-phase condition exists. Fortunately, at most flight conditions the power at higher frequencies is lower than the power at lower frequencies. The  $180^\circ$  phase shift for a 200-hertz fluctuation would occur only between the first and last pressures sampled, and for all other pressures the phase shift would be less than  $180^\circ$ .

An additional time shift existed in some cases because the eight pressures recorded on the second PCM system could shift as much as 0.0025 second from the 32 pressures recorded on the first PCM system. The shift was usually less than 0.0012 second, however, and resulted in only small additional errors. This time shift effect also introduces errors in the phase angle function between two pressures. However, this error can be completely corrected for by shifting the phase angle of each pressure by the amount appropriate for time shift at each frequency. This was done for the phase angle plots shown in later sections.

## TEST PROCEDURE

The primary objective of the flight program was to acquire inlet performance and engine stall data at high supersonic speeds. Flights generally consisted of subsonic climb to 9150 meters (30,000 feet), level acceleration to approximately  $M_\infty = 1.6$ , and climbing acceleration to the desired Mach number, as shown in figure 14. During the level and climbing acceleration, angle-of-attack and angle-of-sideslip pulses were performed and off-schedule inlet geometry excursions were made. At the desired test conditions, angle-of-attack, angle-of-sideslip, or off-schedule inlet operation maneuvers were used to initiate compressor stalls. Most of the stalls at supersonic speeds occurred at maximum afterburning or military (maximum nonafterburning) power settings.

Compressor stalls were initiated at subsonic speeds by expanding the cone to effectively choke the inlet. These stalls were induced at a variety of power settings, speeds, altitudes, and inlet spike and cone positions. Because it was easy to obtain these flight conditions, it was possible to investigate the repeatability of stall margins.

At supersonic speeds, the engine usually recovered from compressor stalls within approximately 1 second. If the source of the high distortion was reduced immediately, the engine recovered completely. If not, the engine usually stalled again and entered a hung-stall condition, causing inlet buzz to occur. Buzz usually continued until Mach number was reduced to approximately 1.4.

At subsonic speeds the engine usually did not recover from a compressor stall. Instead, it entered a rotating stall condition that persisted until engine speed decreased to nearly idle. The engine then recovered.

Compressor stalls were also initiated on the ground at static conditions by off-schedule operation of the inlet geometry. These stalls were performed after every flight to monitor the compressor stall margin at easily repeatable conditions.

## DISCUSSION

### Inlet Performance

The performance of the inlet of F-111A number 6 under steady-state conditions is described in reference 11. Steady-state data for F-111A number 12 are briefly reviewed here, with comparisons, where applicable, with F-111A number 6 data and wind-tunnel data. Inlet performance is described in terms of pressure recovery, distortion, and turbulence. One series of power spectral density plots is shown for the supersonic Mach number range.

Effect of Mach number.— The effect of airplane Mach number on inlet performance is shown in figures 15 and 16. Data were obtained during accelerations along the nominal profile shown in figure 14. The angle of attack flown is shown in figure 15(a), and turbulence, pressure recovery, and  $K_D$  and  $D$  parameters are presented in figures 15(b), 15(c), 15(d), and 15(e), respectively. The turbulence factor and the distortion parameters all decrease up to approximately  $M_\infty = 1.4$  because of the decreasing angle of attack, and recovery increases slightly. Above  $M_\infty = 1.4$ ,  $Tu$ ,  $K_D$ , and  $D$  increase and recovery decreases.

Flight values of pressure recovery are compared with wind-tunnel data from reference 18 in figure 15(c), and agreement is good up to a Mach number of 2.0. The data from F-111A number 6 agree fairly well with the data for F-111A number 12. The lower recovery for F-111A number 6 above  $M_\infty = 1.4$  may be due to its different duct shape and boundary-layer bleed.

Turbulence data for the test airplanes (fig. 15(b)) agree well. The value of the maximum probe (the probe with the highest turbulence) is generally 1 to 1.5 percent above the average of the 40 probes.

Steady-state and peak values of  $K_D$  and  $D$  are shown in figures 15(d) and 15(e). The maximum values of both parameters are considerably higher than the steady-state values because of pressure fluctuations. The wind-tunnel data shown in figure 15(e) agree reasonably well with the flight data at Mach numbers up to approximately 1.8. At Mach numbers above 1.8, the flight and wind-tunnel data disagree, probably because of inlet boundary-layer ingestion in the airplane that did not occur in the wind-tunnel model (ref. 11).

Power spectral density plots for several compressor face pressures are presented in figure 16. A pressure at the 12:00 rake near the hub is shown in figure 16(a). A continuous increase in power level with increasing Mach number is evident. At the lowest Mach number, the power level is near the system noise level and may not be valid.

In figure 16(b), which shows data for a 3:00 rake pressure, the data for  $M_\infty = 1.4$  and 1.6 group into one level; data for  $M_\infty = 1.8, 2.0$ , and 2.2 form a second level; and data for  $M_\infty = 2.4$  form a third level. A duct resonance at approximately 22 to 24 hertz is apparent at Mach 2.2 and 2.4. The rotor speed frequency is also evident at 145 to 160 hertz. Engine speed decreases with increasing Mach number. Figure 16(c) shows that the 7:30 rake trends are similar to the 12:00 rake trends shown in figure 16(a). Figure 16(d) shows that at the 10:30 rake there is a relatively high power level at all Mach numbers. This pressure is downstream of the inlet spike, and a high level of turbulence occurs at all Mach numbers.

In general, the power spectral density curves tend to be nearly flat when the power



levels are low, and to fall off with increasing frequency as the power levels rise. Power levels generally increase with increasing Mach number.

Effect of angle of attack.— Inlet recovery and distortion data obtained during accelerations along the nominal profile are shown in figure 17. The range of angle of attack is fairly small, but there is a definite trend for distortion to be a minimum at an angle of attack of approximately  $5^\circ$ . Pressure recovery effects are not large over the Mach number range shown, but recovery values are maximum at an angle of attack of approximately  $4^\circ$ .

The reduced inlet performance at the lower angles of attack was probably due to reduced precompression by the wing glove. At higher angles of attack, the poorer inlet performance was probably due to fuselage boundary-layer ingestion.

Effect of angle of sideslip.— The effects of nose-left sideslip on the performance of the left inlet at a Mach number of 2.0 are shown in figures 18(a) to 18(d). Recovery drops off rapidly, while turbulence and distortion increase rapidly with increasing sideslip. This high sensitivity is due to the ingestion of increasing amounts of fuselage boundary-layer air as the sideslip angle increases. The engine stalled at  $1.4^\circ$  of sideslip.

Effect of mass flow ratio.— The effect of mass flow ratio on inlet performance is shown in figure 19 for operation at  $M_\infty = 2.0$  with automatic inlet control. Mass flow changed as a result of throttle movements. As mass flow ratio increases, the inlet controller moves the spike and cone as shown. It is apparent that inlet recovery decreases and distortion increases with increasing mass flow ratio. Both average and maximum turbulence decrease and then increase as the mass flow ratio increases above 0.9. Wind-tunnel total pressure recovery data are higher than flight data, except at  $m/m_0 = 0.98$ , where they agree.

In figure 20 the effect of mass flow ratio on inlet performance with the inlet geometry fixed is shown for F-111A number 12 at  $M_\infty = 2.2$ . The wind-tunnel data for recovery are higher than the flight data. The distortion and turbulence data show a minimum value at  $m/m_0 \approx 0.96$  and a rapid increase for higher values of  $m/m_0$ . These data indicate supercritical inlet operation at values of  $m/m_0$  above 0.96, with additional turbulence resulting from the normal shock wave inside the cowl lip. The wind-tunnel recovery data indicated supercritical operation at  $m/m_0 \approx 1.0$ . The mass flow ratio for the onset of inlet buzz from the wind-tunnel data agrees well with the flight data.

Effect of inlet spike and cone position.— The off-schedule performance of the F-111A number 6 inlet is described in reference 10. The scheduled values for F-111A number 12 were different from scheduled values for F-111A number 6, and an example of the variation of inlet performance due to spike and cone movements is shown in figure 21. Cone angle was varied at four different spike positions. The scheduled position was  $\theta_c = 21^\circ$  and  $X/R = 1.71$ , indicated by the symbol in each plot. At  $X/R = 1.71$  and  $X/R = 1.74$ , the optimum cone angle is  $22^\circ$ , while for  $X/R = 1.79$  and  $X/R = 1.84$ , it is some angle less than  $20^\circ$ . The automatic scheduled cone position does not appear to be the optimum setting for  $X/R = 1.71$ , and small variations in  $X/R$  make large cone angle changes necessary to maintain optimum recovery and distortion values.

At subsonic conditions the spike position also has a significant effect on inlet performance, as shown in figure 22. In this case, data were obtained by expanding the cone at fixed spike positions until the engine stalled. For a given cone angle, the  $K_D$  is as much as twice as high at forward spike positions as at aft positions.

## Inlet Duct Resonance

An inlet duct resonance was observed in both airplanes. Because of differences in the inlet geometry and operating conditions, the resonances had different characteristics. There was a larger amount of instrumentation at the inlet on F-111A number 6, and its resonance will be discussed first.

F-111A number 6 duct resonance.— The duct resonance in F-111A number 6 occurred at Mach numbers between 1.8 and 2.1. The resonance was usually weak and could be detected only in power spectral density plots for the compressor face pressures. One of these plots is shown in figure 23(a), which shows data for a Mach number of 1.81. The resonant frequency at 29 hertz is evident in most of the pressures. At some flight conditions, however, the resonance became much stronger, as shown in figure 23(b) for data at Mach 2.0. A 28-hertz frequency was prominent on all pressures, and a harmonic at 56 hertz appears in some pressures. The power level of the pressures and the coherence and phase angle between a pressure in the strongest resonance area and the other pressures are presented in figure 24. The power map (fig. 24(a)) shows that most of the power is concentrated near the top of the compressor face. The coherence map (fig. 24(b)) indicates that coherence is high throughout the region of high resonance power. The phase angle map (fig. 24(c)) reveals that there is a phase shift of almost  $180^\circ$  between the upper inboard and upper outboard areas.

Time histories of four of the compressor face pressures are presented in figure 25. The 28-hertz frequency is obviously present on probes A and B, but for probes C and D, power spectral density plots are necessary to detect the resonant frequency. The out-of-phase relationship between probes A and B is evident in this figure as well as in figure 24(c), and suggests the possibility of high distortion during the resonance. Figure 26 shows the distortion factor,  $K_D$ , and the average pressure recovery,  $\eta_{2av}$ , as a function of time and shows instantaneous recovery maps at times of normal and high distortion. The resonant frequency is not evident in the pressure recovery curve, but is very evident in the  $K_D$  trace. As is shown in the Engine Compressor Stall section of this report, the peak values of  $K_D$  during this resonance are near the stall level. The instantaneous pressure recovery map taken at the peak  $K_D$  shows a very high recovery area in the upper outboard area and a low recovery area in the inboard area. This is in contrast to the map representing normal distortion.

It was found that the occurrence, strength, and frequency of the duct resonance were functions of inlet geometry position, engine airflow, and free-stream Mach number. The intensity of the resonance is plotted qualitatively on a plot of spike position versus cone angle in figure 27. The region of the strongest resonance exists at a particular combination of spike and cone settings. The inlet control system of F-111A number 6 automatically sets the spike and cone in this region between Mach numbers of 1.9 and 2.05 (see fig. 6); however, with the manual inlet control system the pilot could set the inlet geometry to off-schedule positions. With the spike in the position for strongest resonance, the minimum inlet area is slightly inside the cowl lip (figs. 5 and 7) and the cone position results in an inlet throat Mach number of about 1.0. This situation might permit the inlet terminal shock wave to oscillate between the normal external position and an abnormal internal position.

Power spectral density plots for the shock position probe static pressures, cowl lip rake total pressures, cowl lip rake static pressures, inlet duct total and static pressures, and fan duct total pressures are presented in figures 28(a), 28(b), 28(c), 28(d), 28(e), and 28(f), respectively. These plots show evidence of the resonant frequency everywhere except in the cowl lip total pressures on the inboard side of the inlet (fig. 28(b)). The resonance is extremely strong at the upper part of the inlet near the cone surface. A rake located in this

area shows a prominent separation and reattachment cycle, as can be seen in figure 29, which shows the static pressure at the rake base and the rake total pressure. The plot of distortion factor in figure 26 is repeated, and the direct effect on distortion is clearly discernible at the compressor face with the slight phase shift due to the duct transport time. The highest  $K_D$  peaks follow the lowest cowl lip rake pressure levels.

These results suggest that the normal shock oscillation occurs as shown in figure 30. The shock wave is inside and nearly stable at the lower part of the inlet, but it jumps from the internal to the external position at the top. The forward movement of the shock wave separates the boundary layer on the cone, causing the extreme fluctuations near the cone surface seen in figure 29. This separation generates additional oblique shock waves upstream of the normal shock, which momentarily result in high pressure recovery near the upper cowl lip. This combination of low energy separated flow inboard and high energy air outboard then flows down the duct and causes the low and high recovery areas at the compressor face seen in figure 26. As this is happening, the shock wave returns to the internal position. Numerous phase angle and coherence plots and studies of time histories that are not shown substantiate this explanation.

The resonance disappears from the pressure data at airplane Mach numbers below approximately 1.8, probably because the normal shock wave is stably positioned outside the duct. At Mach numbers between 2.1 and 2.2, the resonance does not occur except at reduced mass flow ratio. At the higher mass flow operating point, the normal shock appears to be inside the inlet (supercritical); and at lower mass flows, the normal shock is stable outside the inlet (subcritical operation). Only in the intermediate  $m/m_0$  range is the shock wave sufficiently unstable to sustain the resonance.

F-111A number 12 duct resonance.— The automatic inlet schedule positioned the spike farther aft for F-111A number 12 than for F-111A number 6 (figs. 6 and 27), and only weak resonance occurred in the Mach 1.8 to 2.05 range for F-111A number 12. However, at Mach numbers higher than those flown on F-111A number 6, the duct of F-111A number 12 developed a strong resonance with somewhat different characteristics. This resonance was first observed at Mach 2.25 as the inlet controller began to move the spike forward with the cone fully expanded (see fig. 6), and it continued to increase in intensity up to the maximum attained Mach number of 2.38. A power spectral density plot for typical compressor face pressures at  $M_\infty = 2.32$  is shown in figure 31. The resonant frequency at this Mach number is 23 hertz. The power level of the power spectral density plots at 23 hertz and the phase angle and coherence between the compressor face pressures and pressure B (which is located in the region of strongest resonance) are shown in figure 32. The power is concentrated in the 3:00 region (fig. 32(a)). The coherence map in figure 32(b) shows that coherence is closely related to the power. The phase angle map (fig. 32(c)) shows that most areas of the compressor face are nearly in phase with the pressure at B, but that a small area in the 1:30 region is out of phase by up to  $120^\circ$ .

Because a nearly in-phase condition exists for this resonance, the instantaneous inlet pressure recovery exhibits a 23-hertz fluctuation, while the distortion parameters  $K_D$  and  $K_\theta$  show only occasional effects. This is apparent in figure 33. The pressure recovery fluctuates approximately 1 percent (fig. 33(a)). Four pressure traces for this condition are shown in figure 33(b). Probe B is in the area of strongest resonance and shows the predominant 23-hertz fluctuation with recovery changes of  $\pm 5$  percent. Probes A and C show some evidence of the resonance, and probe A appears to be out of phase with probe B, as indicated in figure 32(c). Probe D shows essentially no resonance, as indicated in figure 32(b).

At higher Mach numbers, the resonance effects became less regular but more intense, as can be seen in figure 34 for data at  $M_\infty = 2.38$ . In figure 34(a), pressure recovery changes as much as  $\pm 2$  percent in 1 cycle, and distortion parameters show peaks that generally occur during rapid increases in the recovery. Pressure traces for the same probes for which pressures were presented in figure 33(b) are shown in figure 34(b) for the higher Mach number. Probes C and D show greater resonant fluctuations, and probe D shows strong resonant effects during the last 3 cycles shown. The observed increase in resonant intensity for 5 to 7 cycles, followed by a sudden shift back to weak resonance, was typical of the duct behavior at these conditions. The left engine did not stall during these conditions.

It appears that the normal shock in the F-111A number 12 inlet is unstable, as in the F-111A number 6 resonance, and that it oscillates in and out of the inlet at the resonant frequency. The resonance begins when the spike moves forward and places the minimum area near the cowl lip, just as in the F-111A number 6. There does not seem to be the severe separation in the F-111A number 12 resonance, although no cowl lip instrumentation was available. The differences between the two airplanes in duct shape, cowl lip shape, and boundary-layer bleed blockage probably account for the differences.

The frequency of the resonance in the two airplanes is similar. Figure 35 is a plot of the resonant frequency as a function of airplane Mach number. The frequency decreases with increasing Mach number for both airplanes. A more detailed analysis of the F-111A number 12 resonance would be difficult because of the lack of instrumentation upstream of the compressor face rakes. An analysis of the F-111A number 6 resonance based on a simple open-pipe formula is presented in reference 13.

### Inlet Duct Buzz

The mechanics of diffuser buzz have been known for some time, and many theories have been proposed to explain the phenomenon. However, no single theory accounts for all the characteristics of buzz. Several of these theories, including the vortex-sheet theory by Ferri, the positive-slope theory by Pearce, the organ-pipe theory by Dailey, and the Helmholtz resonator theory by Sterbentz and Evvard, are presented in reference 19 along with discussions of their specific applications.

A good example of the frequency associated with inlet duct buzz is shown in figure 36, a power spectral density plot of compressor face pressures during buzz at a Mach number of 1.4. It is obvious from this plot that the frequency of the buzz cycle is approximately 11 hertz and that all the pressures at the compressor face fluctuate at the same frequency. The cause of this phenomenon has been determined to be the unstable, subcritical inlet operation associated with fluctuating internal pressures. Inlet duct buzz is always associated with an inlet operating in an external compression mode with the shock pattern oscillating rapidly at the inlet duct entrance.

The inlet duct buzz data obtained in flight were compared with the various buzz theories mentioned in reference 19 and were found to correlate with the wind-tunnel and theoretical Helmholtz resonator data. The frequency and amplitude of the buzz pulsations for the wind-tunnel data and the theoretical data for a large volume Helmholtz resonator at a Mach number of 2.0 are given in references 20 and 21. In figure 37(a) the buzz frequency from the flight data is plotted as a function of mass flow ratio and compared with the data from reference 20. In figure 37(b) the buzz amplitude from the flight data is plotted as a function of mass flow ratio and compared with the data from reference 21. The buzz frequency and amplitude

from the flight data agree reasonably well with the wind-tunnel data and the theory, considering that the referenced data were all obtained at a Mach number of 2.0 and that the flight data were obtained over a range of Mach numbers.

### Engine Compressor Stall

More than 100 compressor stalls occurred during the flight tests of F-111A number 12. These occurred throughout the flight envelope shown in figure 14 and covered a range of power settings with compressor bleeds open and closed. Most of the stalls were intentionally induced. Both steady-state and instantaneous parameters were used in the stall analysis.

Steady-state distortion at stall.— Figure 38 summarizes the steady-state values of  $K_D$  prior to stall, plotted as a function of corrected airflow for all the stalls. Also shown is the engine manufacturer's estimate of the stall line. The average of the flight data agrees well with the estimate at high corrected airflows, but there is a large amount of scatter. At the lower corrected airflows typical of supersonic operation there is less scatter in  $K_{D_{ss}}$ , but the average of the data is higher than the estimate.

The steady-state values of  $K_\theta$  at stall are summarized in figure 39. There is again a large amount of scatter in the data. Values of  $K_D$  at stall increase with increasing corrected airflow, but because of the dynamic pressure term in the  $K_\theta$  formula,  $K_\theta$  values at stall decrease with increasing corrected airflow.

Instantaneous distortion at stall.— Steady-state distortion parameters like those in figures 38 and 39 are not applicable to cases in which large pressure fluctuations occur. This is illustrated in figure 40, which shows values of instantaneous and steady-state  $K_D$  versus time for a stall that occurred at a Mach number of 1.6 with a power setting of maximum afterburning. Note that the low response  $K_D$  is decreasing at the time that the stall occurred, but that the high response  $K_D$  shows a peak just prior to stall. The occurrence of a peak in the instantaneous distortion factor was observed in almost all the stalls encountered. This peak usually occurred approximately 15 to 20 milliseconds before the first indication of the stall hammer shock wave. The time lag is the time it took for the distorted flow to stall the compressor stages and for the resulting hammer shock wave to propagate back to the pressure rakes. Similar time lags were found in the ground facility tests of the TF30 engine described in references 4 and 6. Figure 41 shows the distribution of the time lag between the distortion peak and the hammer shock. In most cases, the delay was between 15 and 20 milliseconds.

The peak values of instantaneous  $K_D$  prior to stall are summarized in figure 42 as a function of corrected airflow. The values of  $K_{D_{peak}}$  are 500 to 600 higher than the  $K_{D_{ss}}$  values at stall. The data scatter is only slightly reduced from the  $K_{D_{ss}}$  plot.

Peak  $K_\theta$  values prior to stall, shown in figure 43, are 0.2 to 0.4 higher than the  $K_{\theta_{ss}}$  data. The effects of afterburning and compressor bleeds are best seen in figure 43. The compressor-bleed-open data are clearly above the bleeds-closed data at corrected airflows below 85 kilograms per second (190 pounds per second). The effects of afterburning are evident at corrected airflows above 95 kilograms per second (210 pounds per second), where the afterburning data are approximately 0.1 below the nonafterburning data.

The peak values of instantaneous  $D$  prior to stall are shown in figure 44. Extreme scatter in the data is evident. Other than a general increase in  $D_{peak}$  with increasing corrected

airflow, no trend can be seen.

Comparison of distortion parameters.— The instantaneous  $K_D$ ,  $D$ , and  $K_\theta$  distortion parameters for two subsonic compressor stalls are compared in figure 45. In the first case (fig. 45(a)), for a Mach number of 0.9 and the military power setting, the  $K_D$ ,  $D$ , and  $K_\theta$  parameters exhibit a peak 15 milliseconds prior to hammershock. For the  $K_D$  and  $K_\theta$  parameters, this peak is the highest that occurred, but the peak in  $D$  is lower than many previous peaks. Similar trends are apparent in figure 45(b) for a stall at a Mach number of 0.7 at a reduced power setting of about 80 percent of military. There are smaller fluctuations in the distortion parameters at the reduced power setting because of lower inlet airflow and turbulence. The stall occurs at lower values of  $K_D$  because the stall margin decreases with lower corrected airflows, as shown in figure 42.

Detailed analysis of stalls.— Figure 46 presents data for a stall induced by a forward movement of the inlet spike at  $M_\infty = 1.7$ . Figure 46(a) shows the average inlet pressure recovery and the distortion parameters. All three instantaneous distortion parameters show a peak at stall initiation; for  $K_D$  and  $K_\theta$  these peaks were higher than any previous peaks. Average recovery variation is small. Pressure traces at five significant locations are shown in figure 46(b). The  $K_D$  parameter is repeated to show the effects of these pressures on distortion. At the time of stall initiation, pressures at probes B and C are high, while the pressures on probes A, D, and E are low, resulting in the high distortion.

Compressor face maps showing average pressure recovery and turbulence prior to stall are shown in figure 46(c). The turbulence level of pressures at D and E is higher than at the other locations. Most of the outboard half of the inlet has a relatively constant pressure level and low turbulence. The inboard area exhibits a fairly strong gradient in total pressure with high turbulence values in the region of strong gradients. The average recovery map (fig. 46(c)) may be compared with the instantaneous maps (fig. 46(d)) taken near the stall initiation time. These maps show the development of high recovery (98 percent) in the 1:30 area and a movement of low recovery in the 9:00 area toward the engine hub. In the last two maps, the 86 percent recovery region has reached the hub and caused sufficiently high distortion to initiate a stall, as was also seen in figure 46(b).

At higher Mach numbers, flow conditions at the compressor face become more dynamic. The stall analyzed in figure 47 occurred at a Mach number of 2.22 in essentially stabilized flight, and it was not intentionally induced. Average pressure recovery and turbulence maps are shown in figure 47(a). The average distortion is not as high as in figure 46(c) at  $M_\infty = 1.7$ , but the turbulence is greater. Figure 47(b) shows the instantaneous pressure recovery and distortion factors. The pressure recovery dropped approximately 2 percent just prior to the stall, and there was a similar drop approximately 0.3 second earlier. Each of the three distortion parameters shows a sharp rise at stall initiation with a peak value above the highest previous peak. Representative pressure traces from five probes are presented in figure 47(c). At stall initiation probes A and B are increasing rapidly while probes C, D, and E are dropping rapidly. The instantaneous recovery maps shown in figure 47(d) show the rapid drop in recovery between the third and fourth maps in the inboard region and some increase in recovery in the upper outboard area. The fourth map has a higher  $K_\theta$  value than the fifth map but the fifth map has a higher  $K_D$ . The two stalls analyzed in this section are typical of most of the 100 stalls analyzed. These stalls were caused by high levels of instantaneous distortion generally caused by a simultaneous increase in pressure in the high pressure recovery area and a decrease in recovery in the low pressure recovery area.

Usefulness of  $K_\theta$ ,  $K_D$ , and  $D$  as stall indicators.— An evaluation of the usefulness

of the three distortion parameters as stall indicators is shown in figure 48 in terms of the percentage of occurrences for which the stall initiation peak value was equal to or greater than any previous peak value. The  $K_\theta$  parameter gave the best indication of stall for the TF30 engine, with a stall initiation peak higher than previous peaks in 73 percent of the stalls. The second best parameter was the  $K_D$  parameter, which had a peak higher than previous peaks in 46 percent of the stalls. The  $D$  parameter, which had its highest peak at stall initiation in only 25 percent of the stalls, was a poor indicator of stall.

Rotating stall.— Rotating stall occurred after many subsonic stalls in the F-111A flight tests, during altitude facility tests at the NASA Lewis Research Center (ref. 22) and during the turbulence generator tests discussed in reference 4. The rotating stall frequency was about 43 percent of the fan rotor speed. Figure 49 shows a series of compressor face recovery maps during 1 cycle of a rotating stall. The high and low recovery areas are on opposite sides of the compressor, and in maps 1, 2, 3, and 4 they rotate at nearly the same speed. In map 5, however, the high recovery zone in the 10:00 region is smaller and a new zone has appeared in the 5:00 region. In map 6 the only high recovery zone is at the 4:00 position, and a new cycle begins. This rotating stall continued until engine speed decayed to nearly idle.

A similar situation occurred in a few cases prior to stall. In one instance, a stall was initiated by expanding the inlet cone at  $M_\infty = 0.9$  at an altitude of 3050 meters (10,000 feet) with the engine at military power. The distortion parameters, shown in figure 50, exhibited a strong periodic component just prior to the stall. The frequency of the fluctuation was 48 percent of  $N_1$  speed. Compressor face maps during 1 cycle of rotating stall, shown in figure 51, bear a strong resemblance to those in figure 49. Pressure traces during this rotating stall are shown in figure 52. The rotating stall affects all the pressures shown. The random turbulence superimposed on the rotating stall pressure is larger at probes B, C, and D and tends to mask the predominant frequency somewhat. A power spectral density plot of typical compressor face pressures is shown in figure 53. A prominent rotating stall peak occurs in all the pressure traces except a few located at the 7:30 rake. The stall zone consistently dissipated in the 9:00 area and reformed near the 6:00 area, as in figure 51, minimizing the effects in between. The rotating stall did not seem to affect the engine's overall stall margin significantly, since many cycles occurred before the overall flow broke down. Distortion values for this stall were, in fact, similar to distortion values for other engine stalls during which no rotating stall was evident.

Reasons for lack of correlation between distortion and stall.— Some explanations for the stalls that occurred at distortion values lower than the peak values may be suggested. One possibility is that the 40 probes do not sample all of the flow entering the compressor, so some high or low pressure areas may not be adequately sampled.

A second possibility concerns the data sampling error introduced by the PCM system. (This error is discussed in the DATA ANALYSIS section.) Improper phasing may cause some distortion peaks to be too high and others to be too low, particularly in the subsonic stalls, in which the high frequency fluctuations are very large.

A third possibility is the existence of a rotating stall somewhere in the compressor, as discussed in the preceding section. However, additional internal engine instrumentation would be required to determine the distortion at highly loaded stages of the compressor where the stall actually originates.

Despite these deficiencies, the  $K_\theta$  parameter correctly indicated 73 percent of the stalls.

This shows that if the proper instantaneous distortion parameter is used, data can be correlated with most of the compressor stalls that occurred.

### Rotor Speed Frequencies

At some flight conditions, a prominent frequency at the fan rotation speed was present in the compressor face pressure data. This frequency and its harmonics are caused by shock waves from the compressor blades operating at supersonic tip speeds, and cause the well-known multiple pure tone noise discussed in reference 23.

A power spectral density plot of an analog record of a compressor face rake pressure is shown in figure 54 for a Mach number of 2.0 from F-111A number 6 data. Duct resonance, power supply, low and high pressure compressor rotor speeds, and harmonics account for all the observed peaks.

The  $N_1$  frequency may also be seen in the power spectral density plots of digitally recorded pressures shown in figure 16 at Mach numbers of 1.4, 1.6, and 1.8. At Mach numbers above 1.8, random fluctuations generally mask the rotor speed frequencies. Figure 55 shows power spectral density plots of compressor face pressures for two flights at  $M_\infty = 1.83$ . In figure 55(a) at 11,000 meters (36,000 feet) with a  $T_{t2}$  of  $366^\circ \text{ K}$  ( $659^\circ \text{ R}$ ), the  $N_1$  frequency is evident on most pressures, but the power level does not exceed  $10^{-6}$ . In figure 55(b) at 13,700 meters (45,000 feet) on a colder day with a  $T_{t2}$  of  $350^\circ \text{ K}$  ( $630^\circ \text{ R}$ ), the  $N_1$  frequency is very prominent on all probes and has a power level up to  $10^{-4}$ . In addition, peaks occur at 70 hertz and 82 hertz due to interactions between  $N_1$  and  $N_2$  frequencies. The general level of the data, except for the rotor speed peaks, is essentially the same for the two flight conditions. The fan blade tip Mach numbers are 1.05 in figure 55(a) and 1.22 in figure 55(b), which probably explains the great difference in the power at the rotor speed frequencies.

The significance of these rotor speed frequencies, other than their obvious influence on noise, is difficult to determine. As explained in reference 23, the effects of shock waves from the blades decay rapidly with increasing distance. The compressor face rakes in the F-111A tests were close enough to the blades to be strongly affected by them. For the colder-than-standard-day conditions in figure 55(b), rotor speed harmonics so affected the pressure data that strong evidence of the rotor speed frequency was present in the instantaneous distortion parameters. However, it is believed that these frequencies do not affect compressor stability and should not be taken into consideration in distortion parameter calculations.

### CONCLUSIONS

Flight tests of two F-111A airplanes to study the effects of steady-state and dynamic pressure phenomena on the propulsion system yielded the following conclusions:

1. Most of the engine compressor stalls were caused by high levels of instantaneous distortion. The distortion was usually the result of a simultaneous increase in pressure in the high pressure recovery area and decrease in pressure in the low pressure recovery area.

2. The instantaneous circumferential distortion parameter  $K_\theta$  exhibited a peak just prior to stall higher than any previous peaks in 73 of 100 stalls analyzed. The distortion



factor  $K_D$  was the second best parameter for indicating stall, while the maximum-minus-minimum distortion parameter  $D$  was a poor indicator of stall.

3. Inlet duct resonance occurred in both test airplanes. In F-111A number 6, the resonance was out of phase on opposite sides of the compressor face, causing high distortion, while in F-111A number 12 the resonance was in phase across the compressor face, causing large fluctuations in pressure recovery. Both resonances were believed to be caused by oscillations of the normal shock wave from an internal to an external position.

4. The inlet performance of the two airplanes in terms of pressure recovery, distortion, and turbulence was similar. Agreement between flight and wind-tunnel data was good up to a Mach number of approximately 1.8.

5. Power spectral density plots of compressor face pressures generally showed increasing power levels with increasing Mach number. When power levels were low, the power spectral density curves tended to be flat, while at higher power levels the curves tended to fall off with increasing frequency.

6. The frequency and amplitude of the inlet duct buzz data obtained in flight compared reasonably well with wind-tunnel and theoretical data.

Flight Research Center,  
National Aeronautics and Space Administration,  
Edwards, Calif., April 12, 1973.

## REFERENCES

1. Kimzey, W. F.: An Investigation of the Effects of Shock-Induced Turbulent Inflow on a YJ93-GE-3 Turbojet Engine. AEDC-TR-66-198, Arnold Eng. Dev. Center, Nov. 1966.
2. Smith, Ronald H.; Bellman, Donald R.; and Hughes, Donald L.: Preliminary Flight Investigation of Dynamic Phenomena Within Air Breathing Propulsion Systems of Supersonic Aircraft. AIAA Paper No. 68-593, 1968.
3. Plourde, G. A.; and Brimelow, Brian: Pressure Fluctuations Cause Compressor Instability. Proceedings of the Air Force Airframe-Propulsion Compatibility Symposium, AFAPL-TR-69-103, Air Force Aero Propulsion Lab., June 24-26, 1969, pp. 567-603.
4. Gray, W. G.: Propulsion System Flow Stability Program (Dynamic). Phase I Final Technical Report—Part IV. TF30 Engine and Compressor Tests and Analysis of Test Data. Tech. Rep. AFAPL-TR-68-142, Part IV, Air Force Aero Propulsion Lab., Dec. 1968.
5. Meyer, Carl L.; McAulay, John E.; and Biesiadny, Thomas J.: Technique for Inducing Controlled Steady-State and Dynamic Inlet Pressure Disturbances for Jet Engine Tests. NASA TM X-1946, 1970.
6. Braithwaite, Willis M.; Dicus, John H.; and Moss, John E., Jr.: Evaluation With a Turbofan Engine of Air Jets as a Steady-State Inlet Flow Distortion Device. NASA TM X-1955, 1970.
7. McAulay, John E.: Effect of Dynamic Variations in Engine-Inlet Pressure on the Compressor System of a Twin-Spool Turbofan Engine. NASA TM X-2081, 1970.
8. Bellman, Donald R.; and Hughes, Donald L.: The Flight Investigation of Pressure Phenomena in the Air Intake of an F-111A Airplane. AIAA Paper No. 69-488, 1969.
9. Burcham, Frank W., Jr.; and Hughes, Donald L.: Analysis of In-Flight Pressure Fluctuations Leading to Engine Compressor Surge in an F-111A Airplane for Mach Numbers to 2.17. AIAA Paper No. 70-624, 1970.
10. Martin, Richard A.; and Hughes, Donald L.: Comparisons of In-Flight F-111A Inlet Performance for On- and Off-Scheduled Inlet Geometry at Mach Numbers of 0.68 to 2.18. NASA TN D-6490, 1971.
11. Hughes, Donald L.; Holzman, Jon K.; and Johnson, Harold, J.: Flight-Determined Characteristics of an Air Intake System on an F-111A Airplane. NASA TN D-6679, 1972.
12. Holzman, Jon K.; and Payne, Gordon A.: Design and Flight Testing of a Nullable Compressor Face Rake. NASA TN D-7162, 1973.
13. Burcham, Frank W., Jr.; and Bellman, Donald R.: A Flight Investigation of Steady-State and Dynamic Pressure Phenomena in the Air Inlets of Supersonic Aircraft. Inlets and Nozzles for Aerospace Engines, AGARD CP-91-71, paper No. 24, Dec. 1971.

14. Mechtly, E. A.: The International System of Units—Physical Constants and Conversion Factors. NASA SP-7012, 1969.
15. Bellman, Donald R.; Burcham, Frank W., Jr.; and Taillon, Norman V.: Techniques for the Evaluation of Air-Breathing Propulsion Systems in Full-Scale Flight. Flight Test Techniques, AGARD CP-85, paper No. 7, Feb. 1972.
16. Bendat, Julius S.; and Piersol, Allan G.: Measurement and Analysis of Random Data. John Wiley & Sons, Inc., c.1966.
17. Crites, Roger C.: The Philosophy of Analog Techniques Applied to the Analysis and High Speed Screening of Dynamic Data. AIAA Paper No. 70-595, May 18-20, 1970.
18. Hartin, J. P.: Wind Tunnel Investigation at Transonic and Supersonic Mach Numbers of Duct Modifications to the F-111A Inlet. AEDC-TR-66-19, Arnold Eng. Dev. Center, Feb. 1966. (Available from DDC as AD 369494.)
19. Anon.: Handbook of Supersonic Aerodynamics. Section 17—Ducts, Nozzles and Diffusers. NAVWEPS Rep. 1488 (Volume 6), Jan. 1964, pp. 143—223.
20. Sterbentz, William H.; and Evvard, John C.: Criteria for Prediction and Control of Ram-Jet Flow Pulsations. NACA TN 3506, 1955.
21. Sterbentz, William H.; and Davids, Joseph: Amplitude of Supersonic Diffuser Flow Pulsations. NACA TN 3572, 1955.
22. Braithwaite, Willis M.; and Vollmar, William R.: Performance and Stall Limits of a YTF30-P-1 Turbofan Engine With Uniform Inlet Flow. NASA TM X-1803, 1969.
23. Pickett, Gordon F.: Prediction of the Spectral Content of Combination Tone Noise. J. Aircraft, vol. 9, No. 9, Sept. 1972, pp. 658—663.

TABLE 1. NUMBER OF MEASUREMENTS, SAMPLING RATE, AND FREQUENCY RESPONSE OF PRESSURES IN TWO F-111A AIRPLANES

Location of pressures	Number of measurements		Samples per second	Frequency response, hertz (a)
	F-111A number 6	F-111A number 12		
Cone rake:				
Total pressure	8	—	400	200
Static pressure	2	—	400	200
Cowl lip:				
Total pressure	12	—	200	100 <sup>b</sup>
Static pressure	4	—	200	100 <sup>b</sup>
Shock position probe	6	—	200	100 <sup>b</sup>
Inlet duct:				
Total pressure	4	—	200	100
Static pressure	4	—	200	100
Compressor face:				
Total pressure, low response	20	—	50	10
Total pressure, high response	20	40 <sup>c</sup>	400	200
Fan duct total pressure	8	—	200	100 <sup>b</sup>
Low compressor discharge static pressure	1	1	200	100 <sup>b</sup>
High compressor discharge static pressure	1	1	200	100 <sup>b</sup>

<sup>a</sup>Maximum frequency for statistical analysis.

<sup>b</sup>Parameter filtered at 40 hertz prior to digitizing; amplitude uncertain above 40 hertz.

<sup>c</sup>Nulling type of compressor face rake.

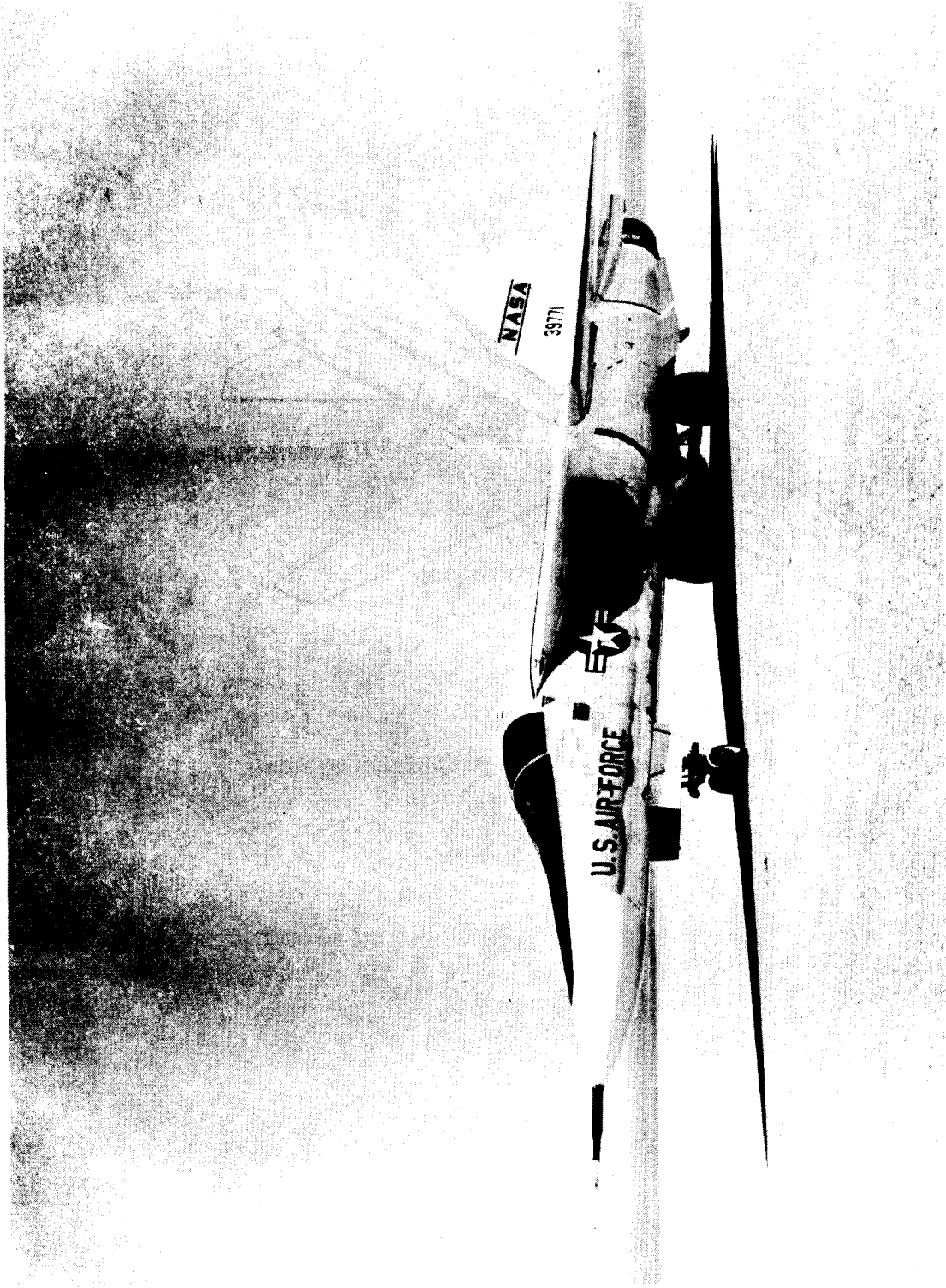
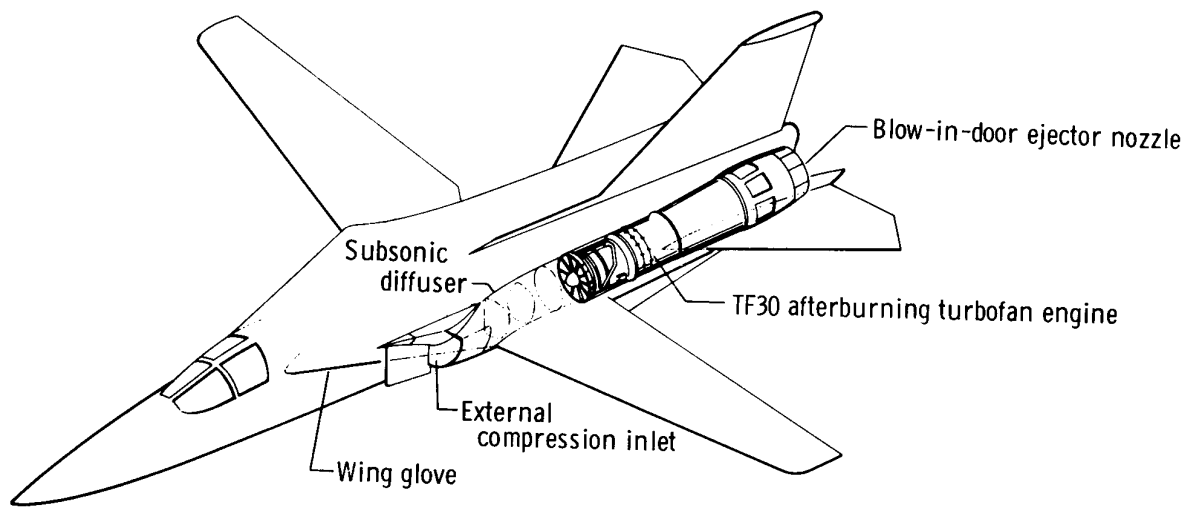


Figure 1. F-111A airplane.

E-20273



**Figure 2. F-111A left propulsion system.**

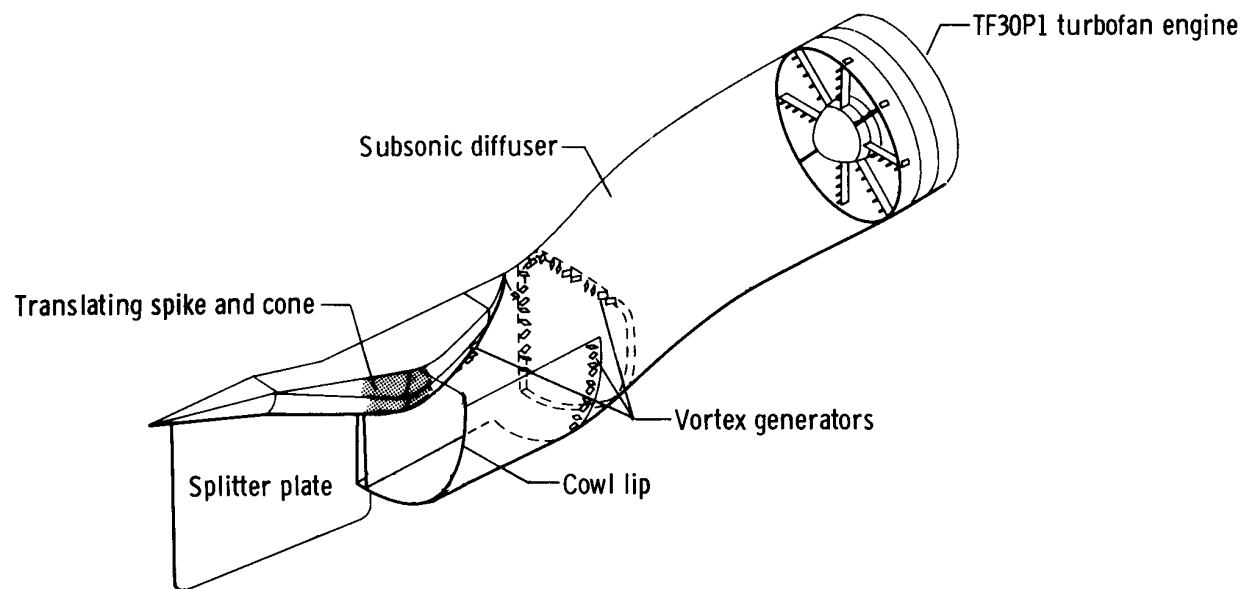
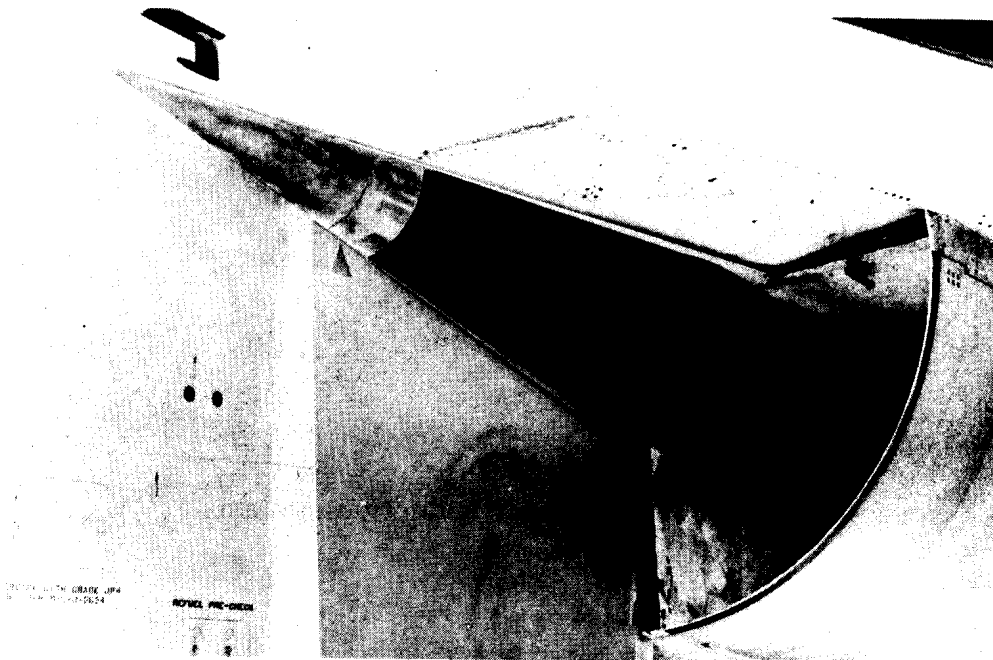
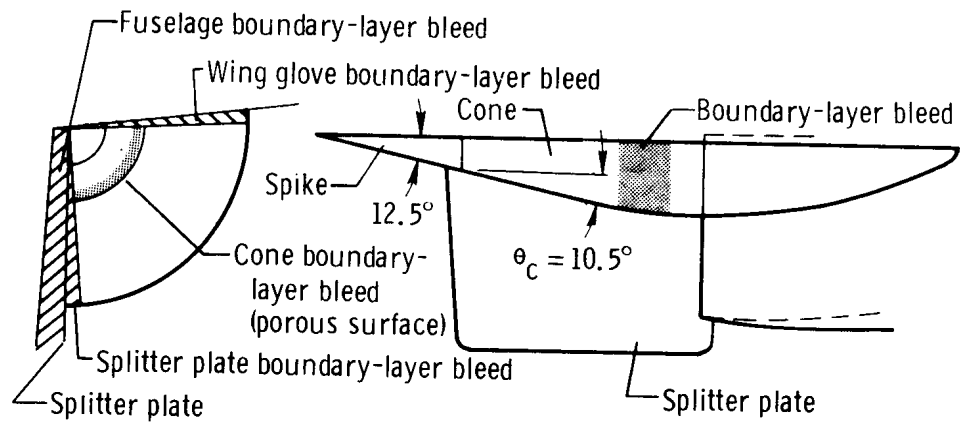


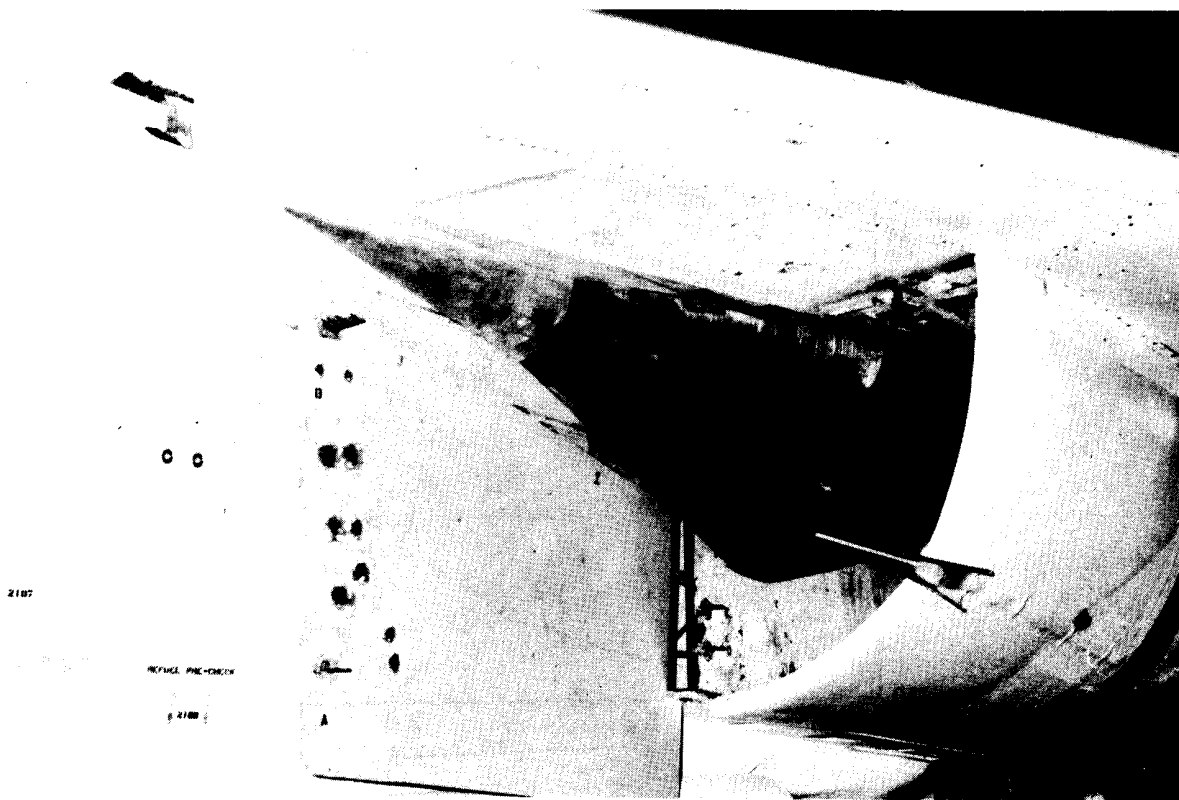
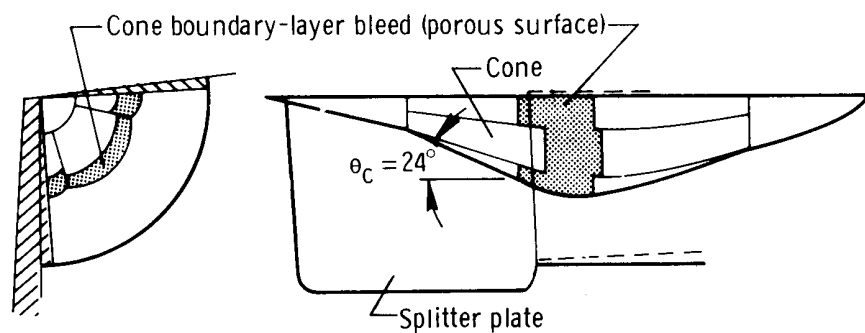
Figure 3. F-111A air induction system.



E-16318

Figure 4. Photograph and two-view drawing of the F-111A inlet with sharp lip cowl installed, spike full forward, and cone fully collapsed.





E-21377

Figure 5. Photograph and two-view drawing of the F-111A inlet with blunt lip cowl installed, spike full aft, and cone fully expanded.

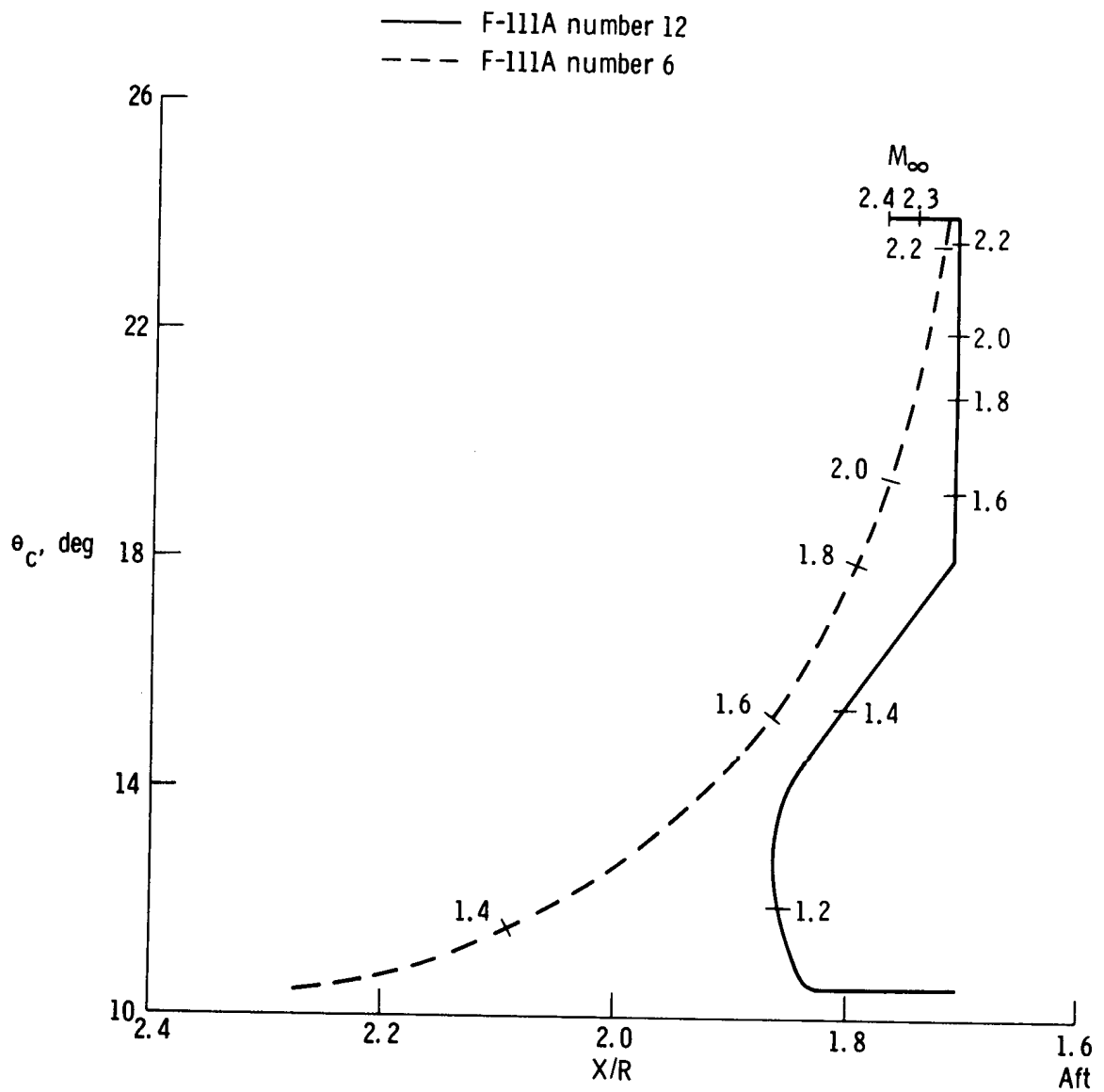


Figure 6. Automatic schedule of spike and cone position for a typical supersonic acceleration profile. Maximum afterburning power.

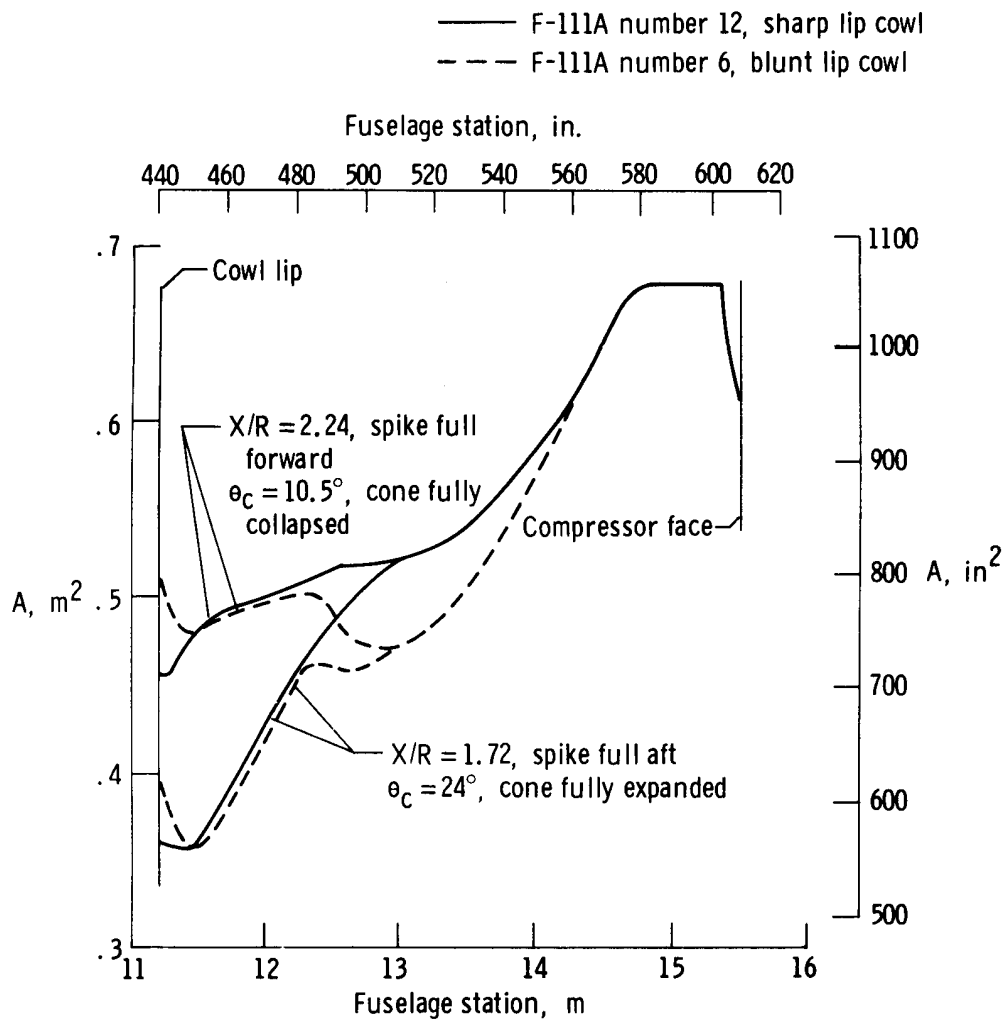


Figure 7. Inlet duct area distribution.

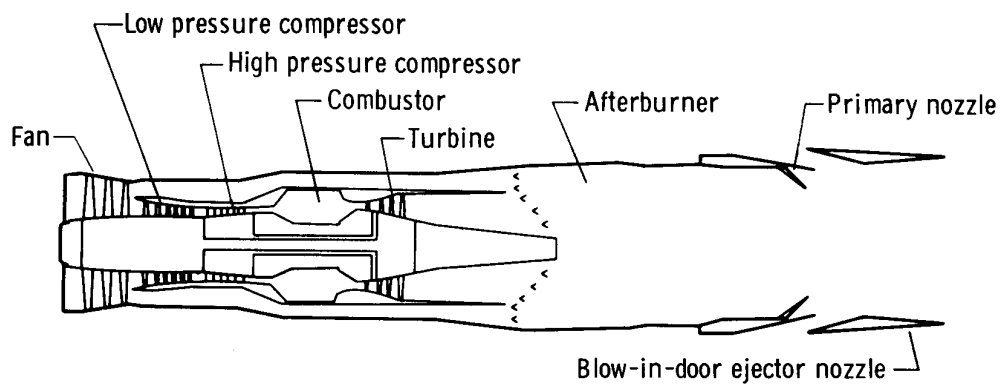


Figure 8. Schematic view of the TF30 engine.

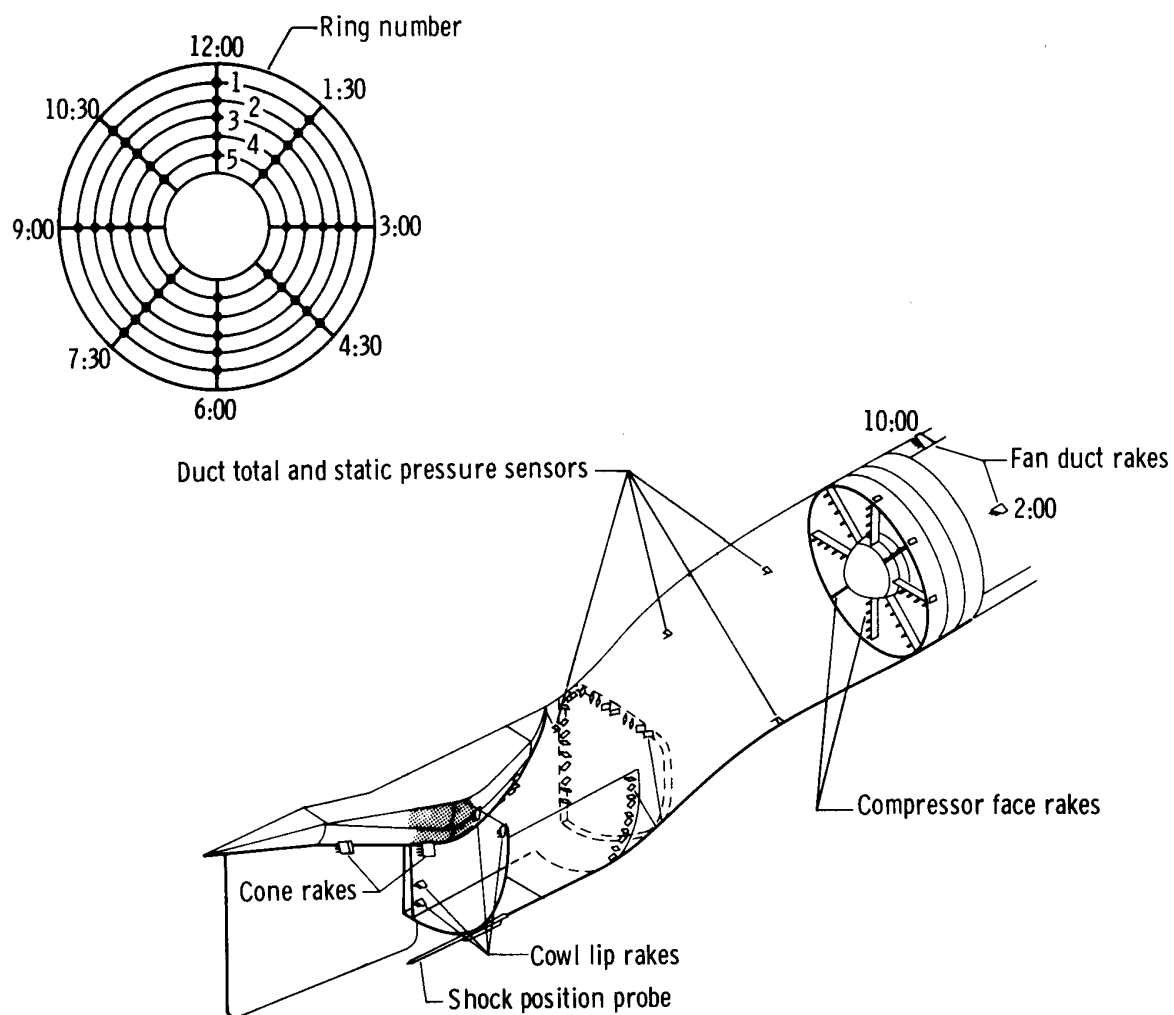


Figure 9. Inlet and compressor face pressure instrumentation.

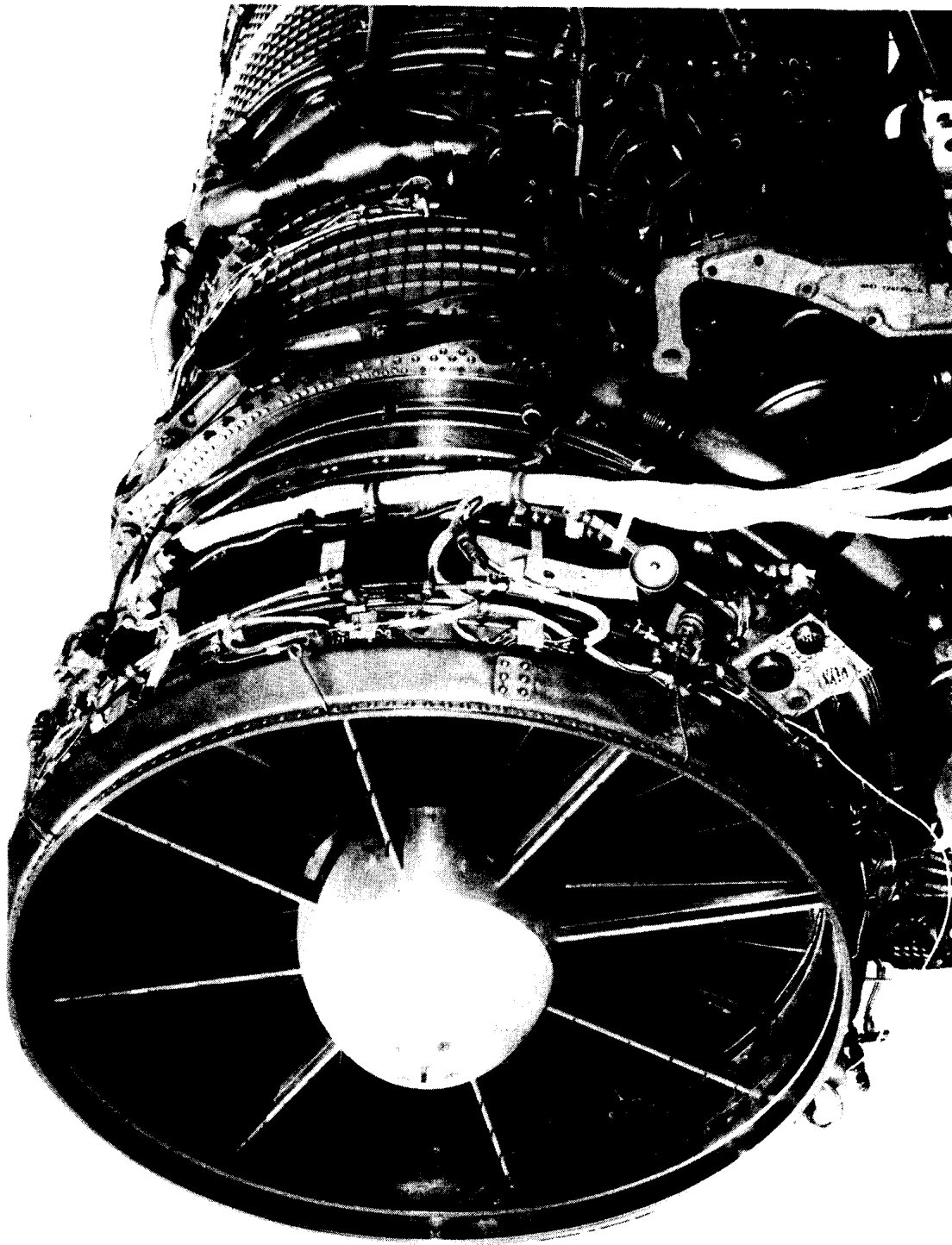


Figure 10. TF30 engine showing compressor face rakes with in-flight nulling capability. E-22912

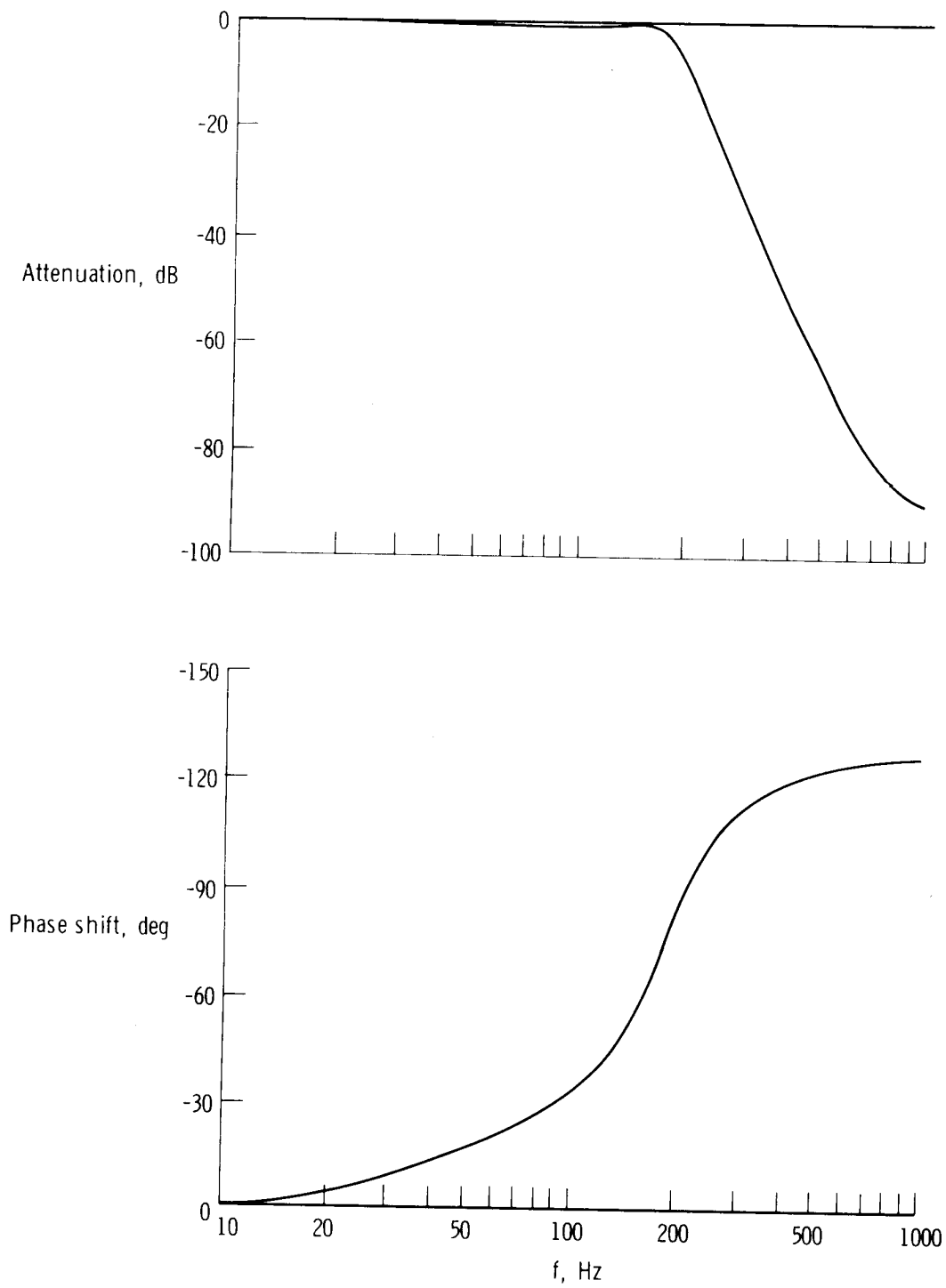


Figure 11. Attenuation and phase shift for the compressor face rake electrical filters.

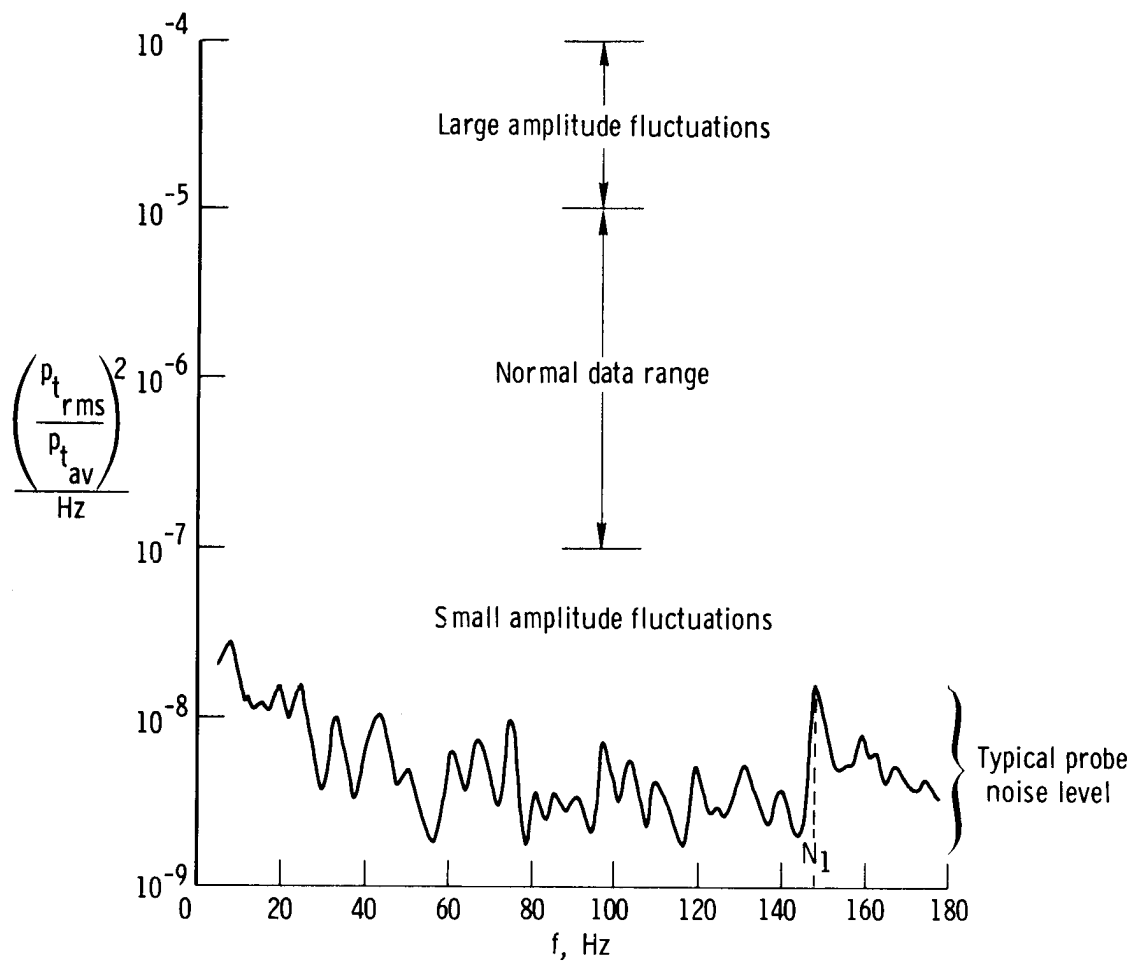


Figure 12. Power spectral density plot showing normal data range and a typical pressure probe noise level.



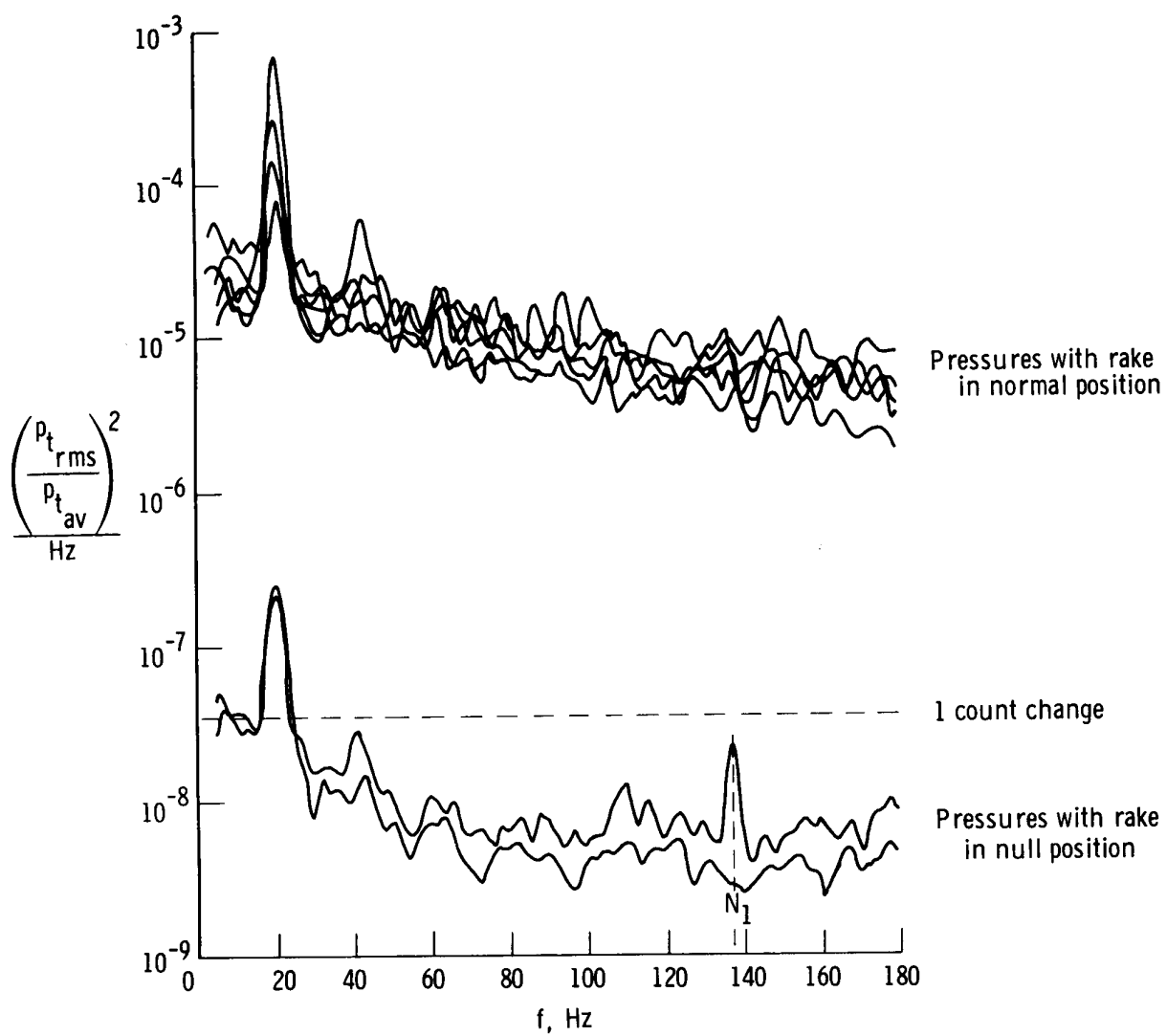


Figure 13. Power spectral density plot showing system cross talk level and the level of a 1 count change in pressure.

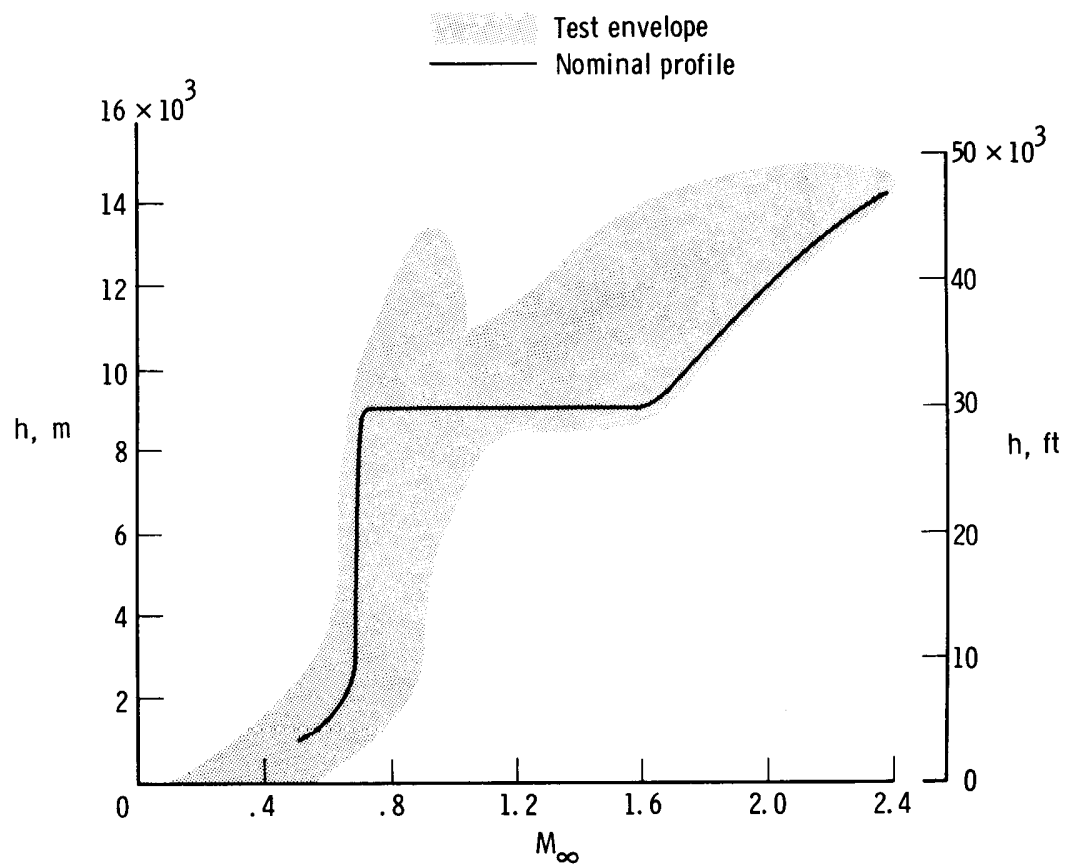
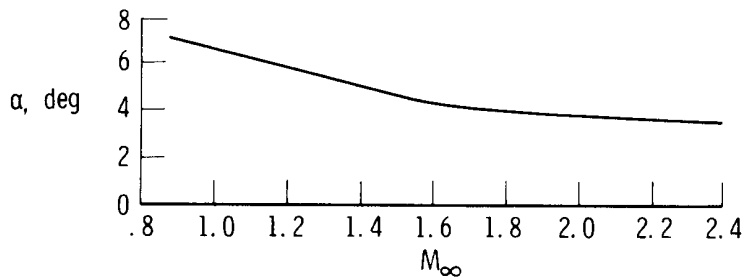
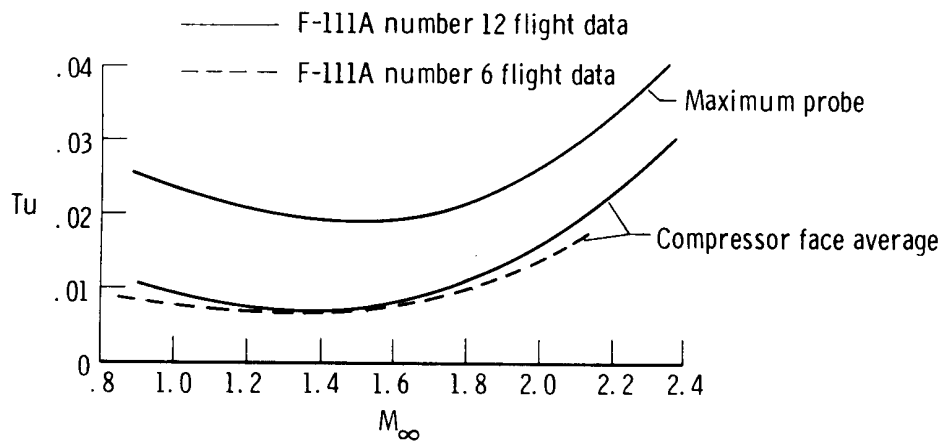


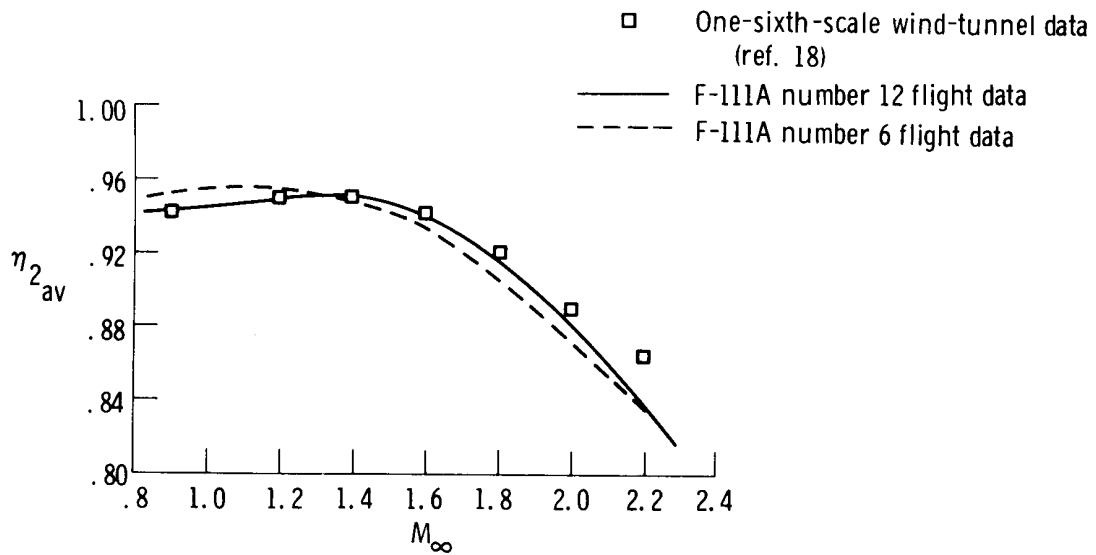
Figure 14. Flight test envelope and typical profile for F-111A flights.



(a) Angle of attack.

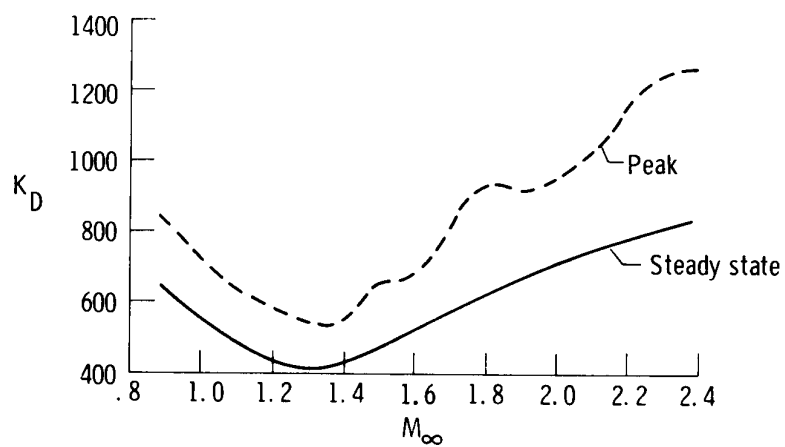


(b) Turbulence factor.

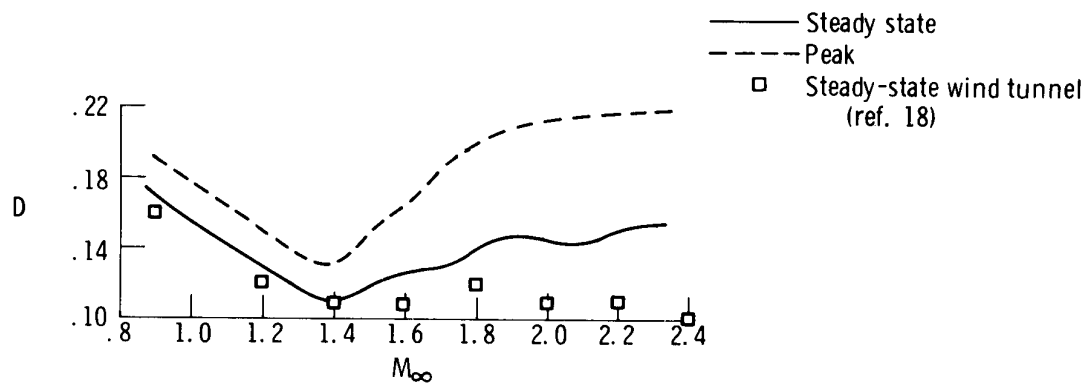


(c) Pressure recovery.

Figure 15. Effect of Mach number for the angle of attack shown on turbulence, compressor face recovery, and distortion. Nominal profile acceleration and climb (fig. 14).

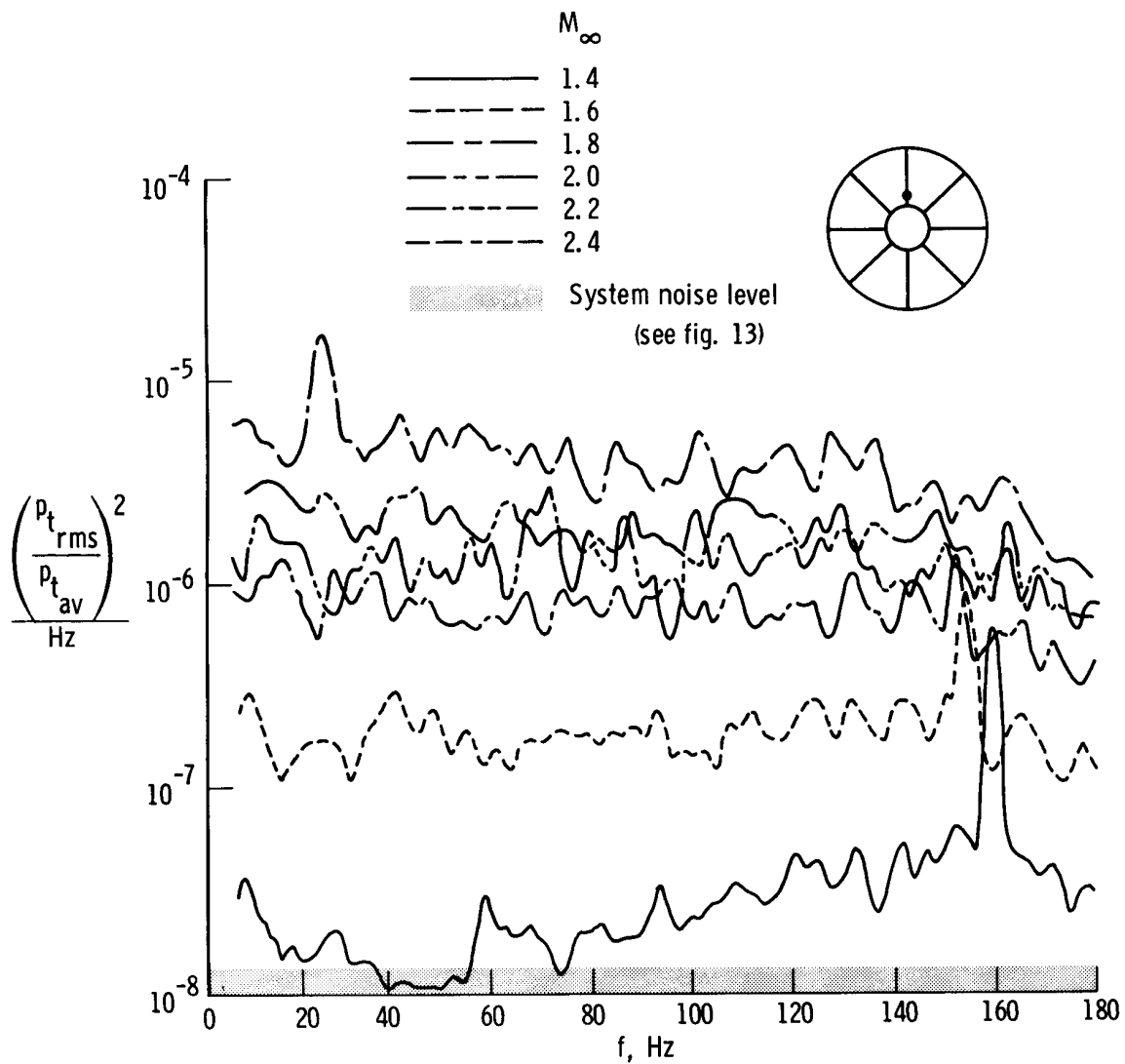


(d)  $K_D$  factor, F-111A number 12.



(e) Distortion factor, F-111A number 12.

Figure 15. Concluded.



(a) Pressure probe on ring 5 at 12:00 rake.

Figure 16. Effect of Mach number on the power spectral density of compressor face pressures. Maximum afterburning power; nominal flight profile (fig. 14); F-111A number 12.

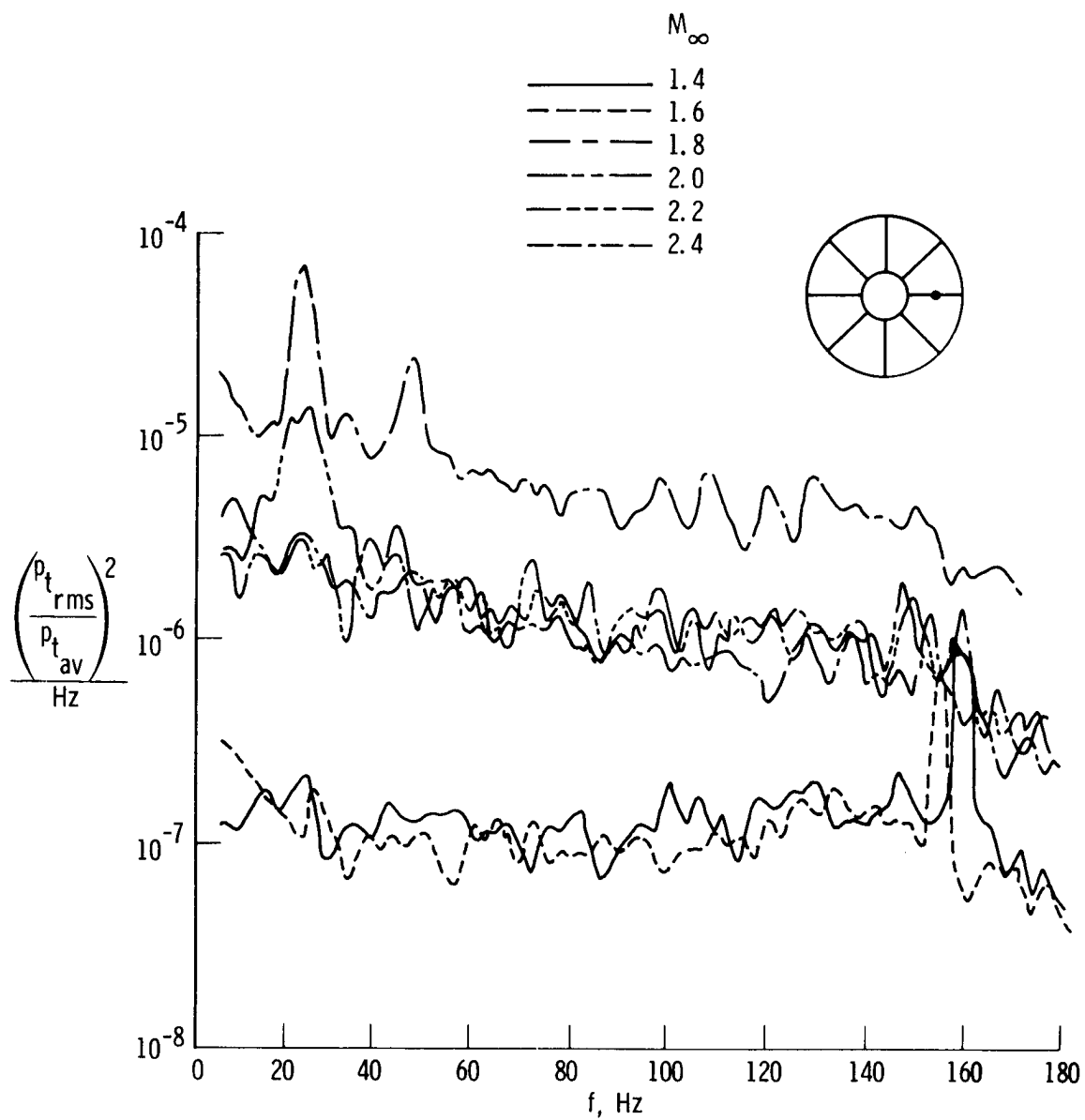
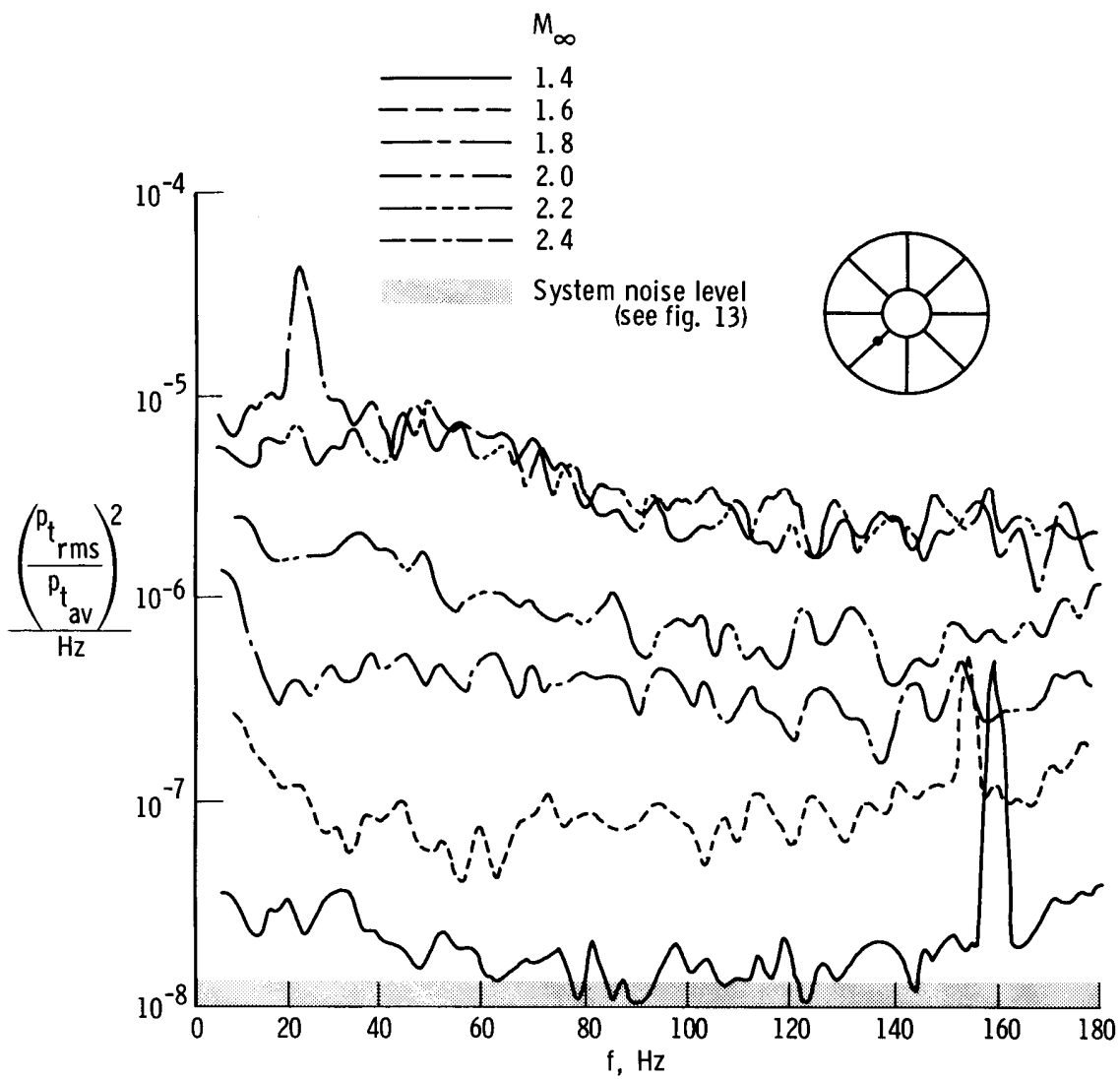
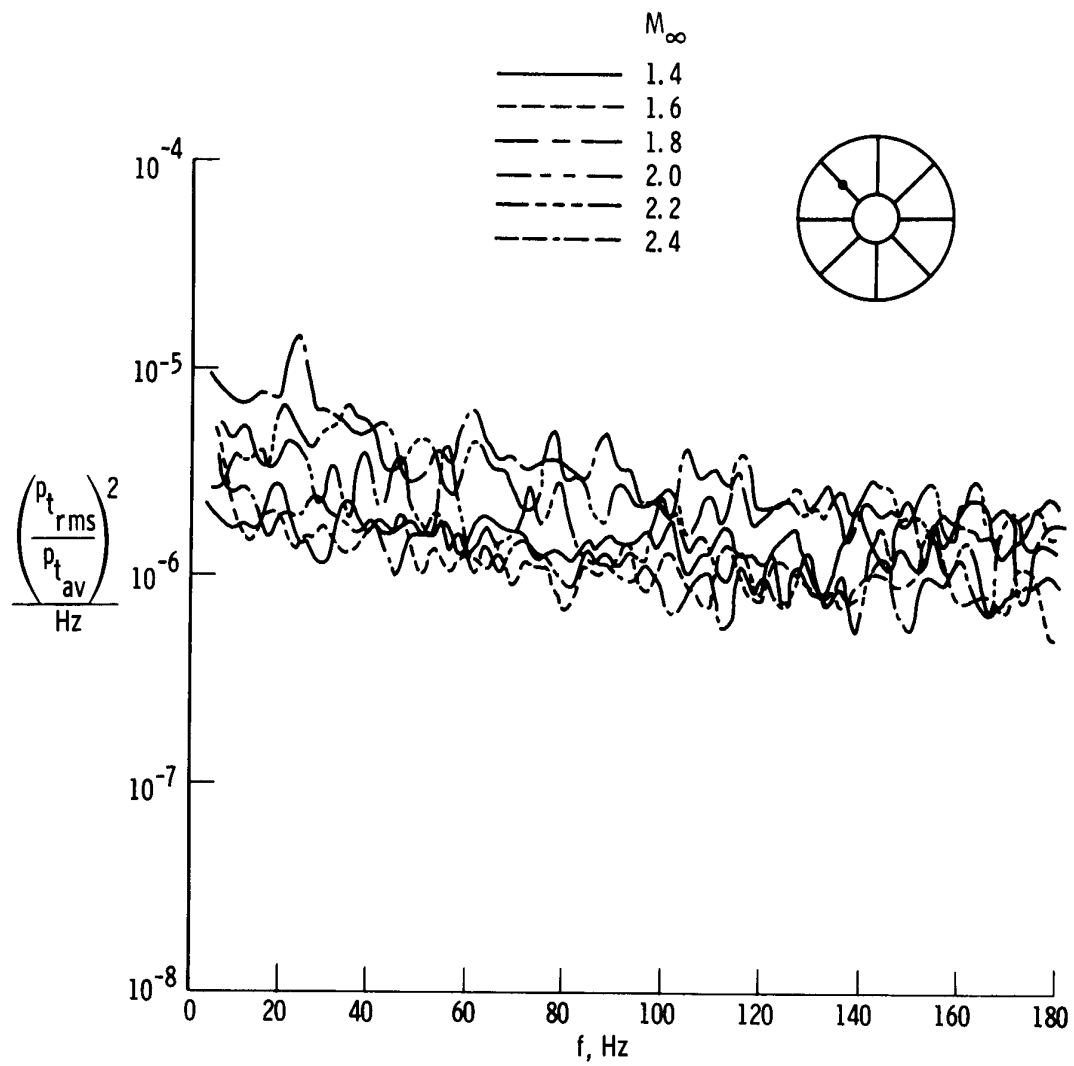


Figure 16. Continued.



(c) Pressure probe on ring 4 at 7:30 rake.

Figure 16. Continued.



(d) Pressure probe on ring 3 at 10:30 rake.

Figure 16. Concluded.



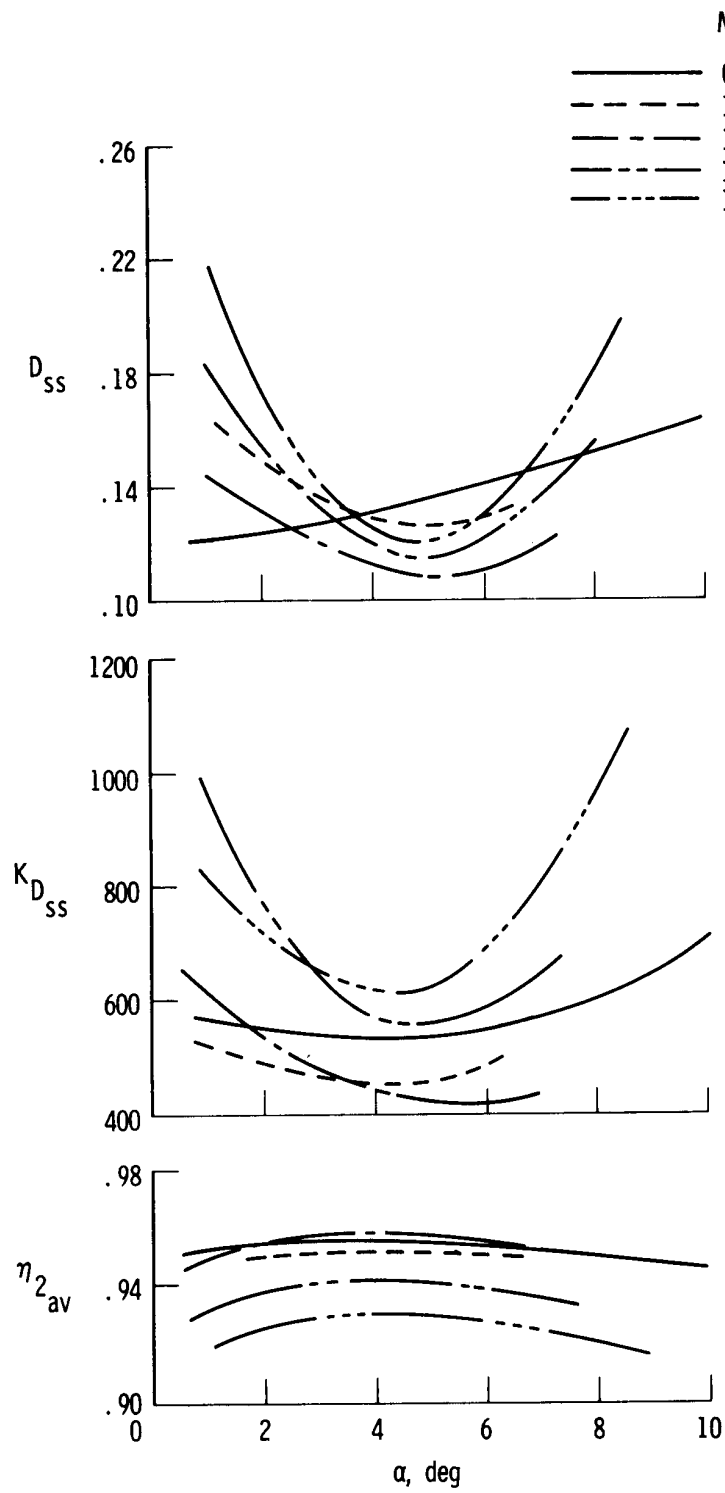
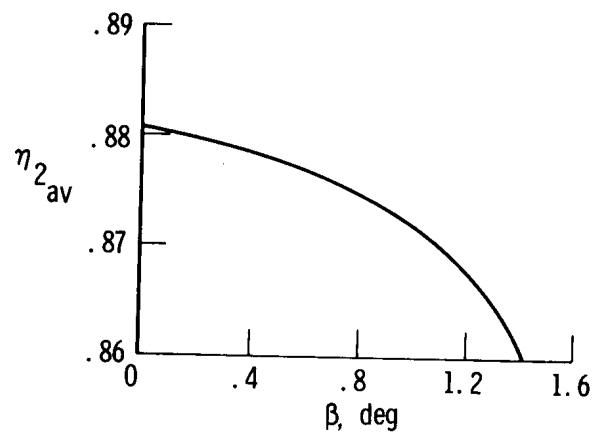
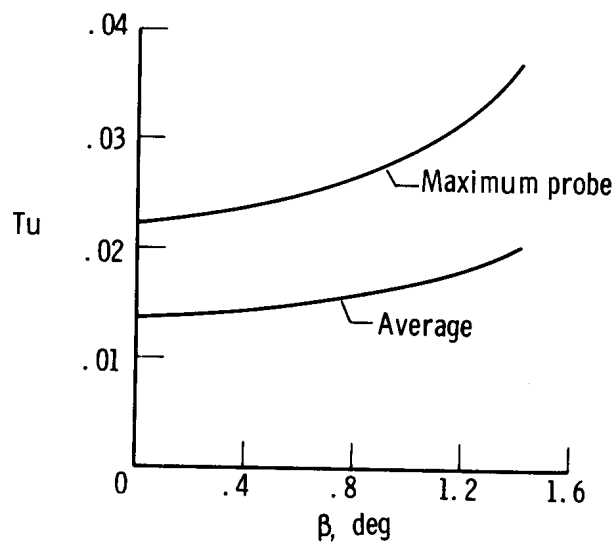


Figure 17. Effect of angle of attack on steady-state inlet distortion and recovery. F-111A number 12.

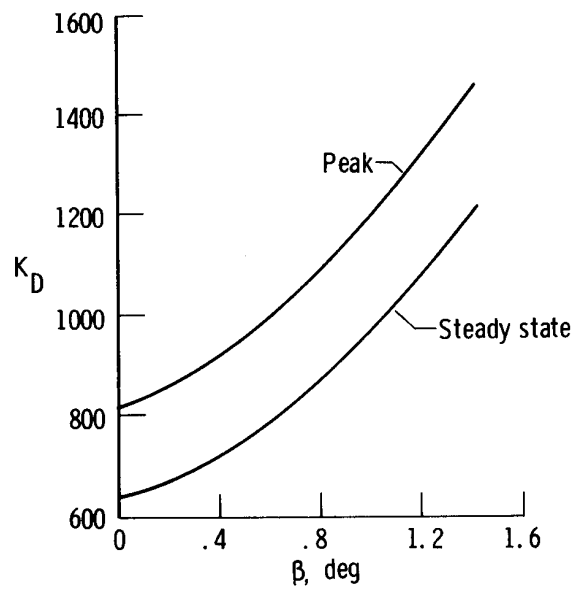


(a) Pressure recovery.

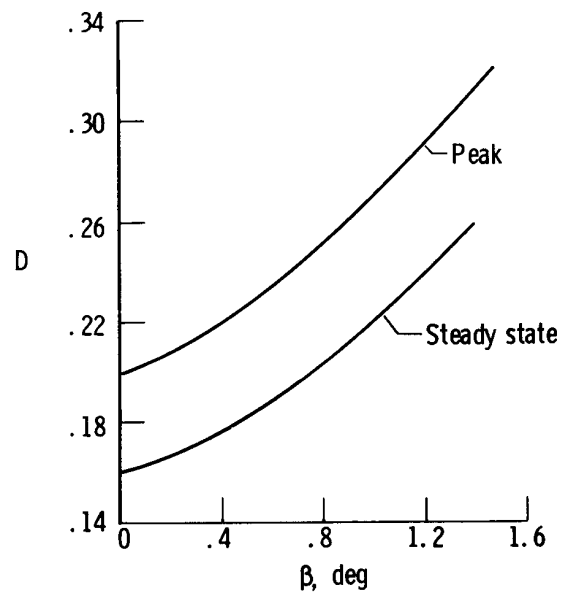


(b) Turbulence factor.

Figure 18. Effect of nose-left sideslip on left inlet pressure recovery, turbulence, and distortion.  $M_\infty = 2.0$ ; F-111A number 12.



(c)  $K_D$  factor.



(d) Distortion factor.

Figure 18. Concluded.

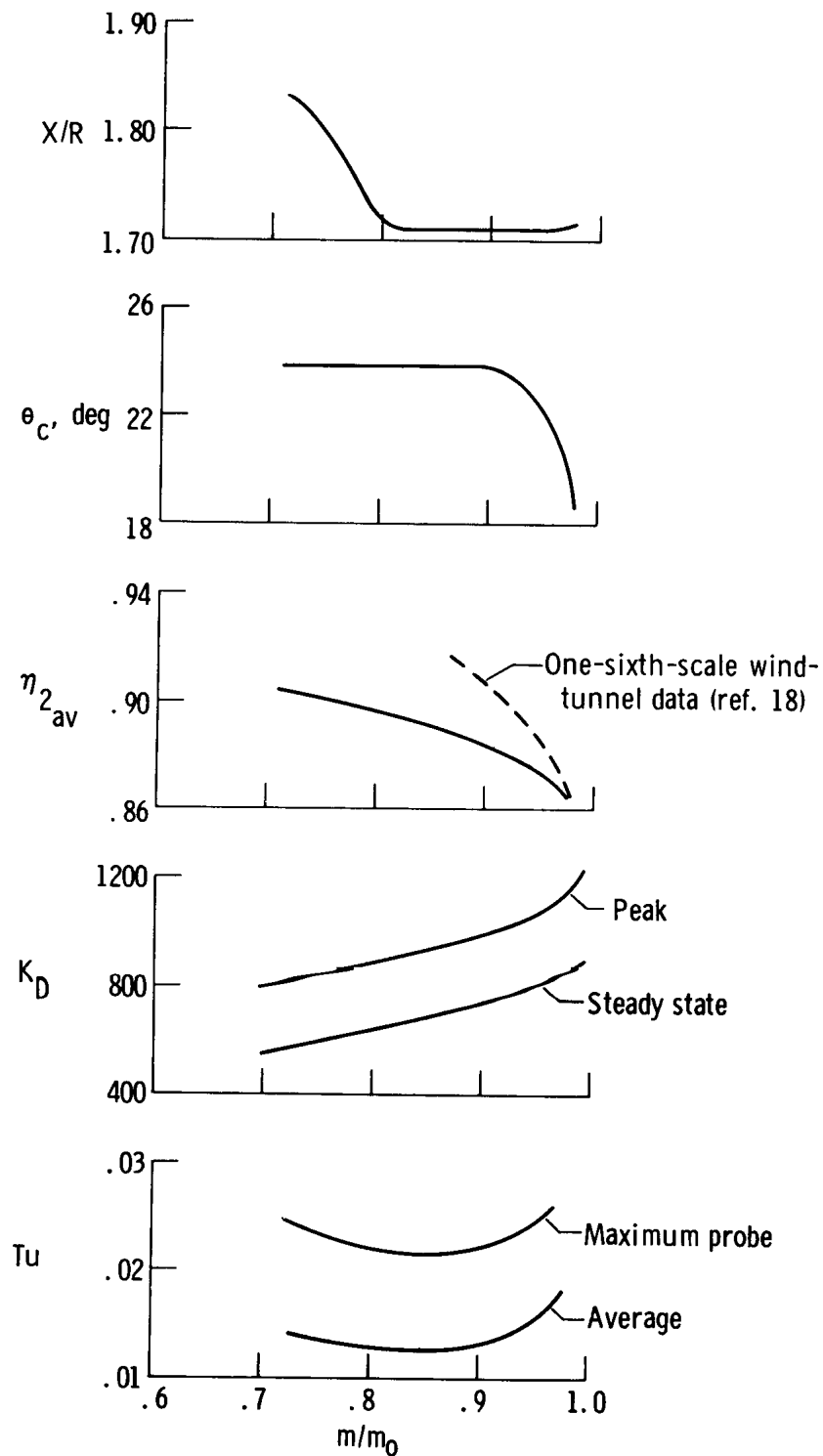


Figure 19. Effect of mass flow ratio on inlet spike and cone position, recovery, distortion, and turbulence. Automatic schedule;  $M_\infty = 2.0$ ; F-111A number 12.

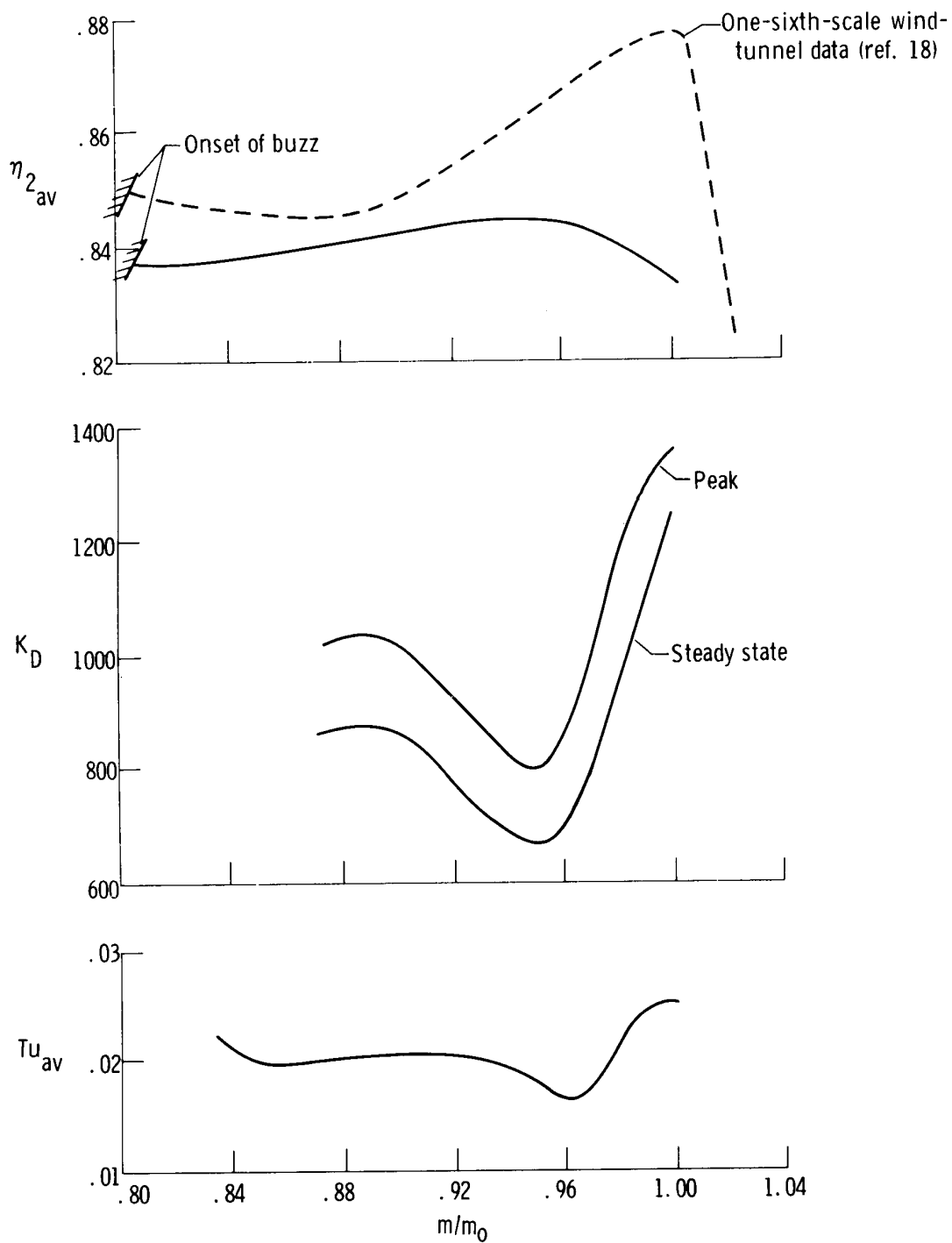


Figure 20. Effect of mass flow ratio on inlet recovery, distortion, and turbulence.  $M_\infty = 2.2$ ;  $\theta_c = 24^\circ$ ;  $X/R = 1.72$ ; F-111A number 12.

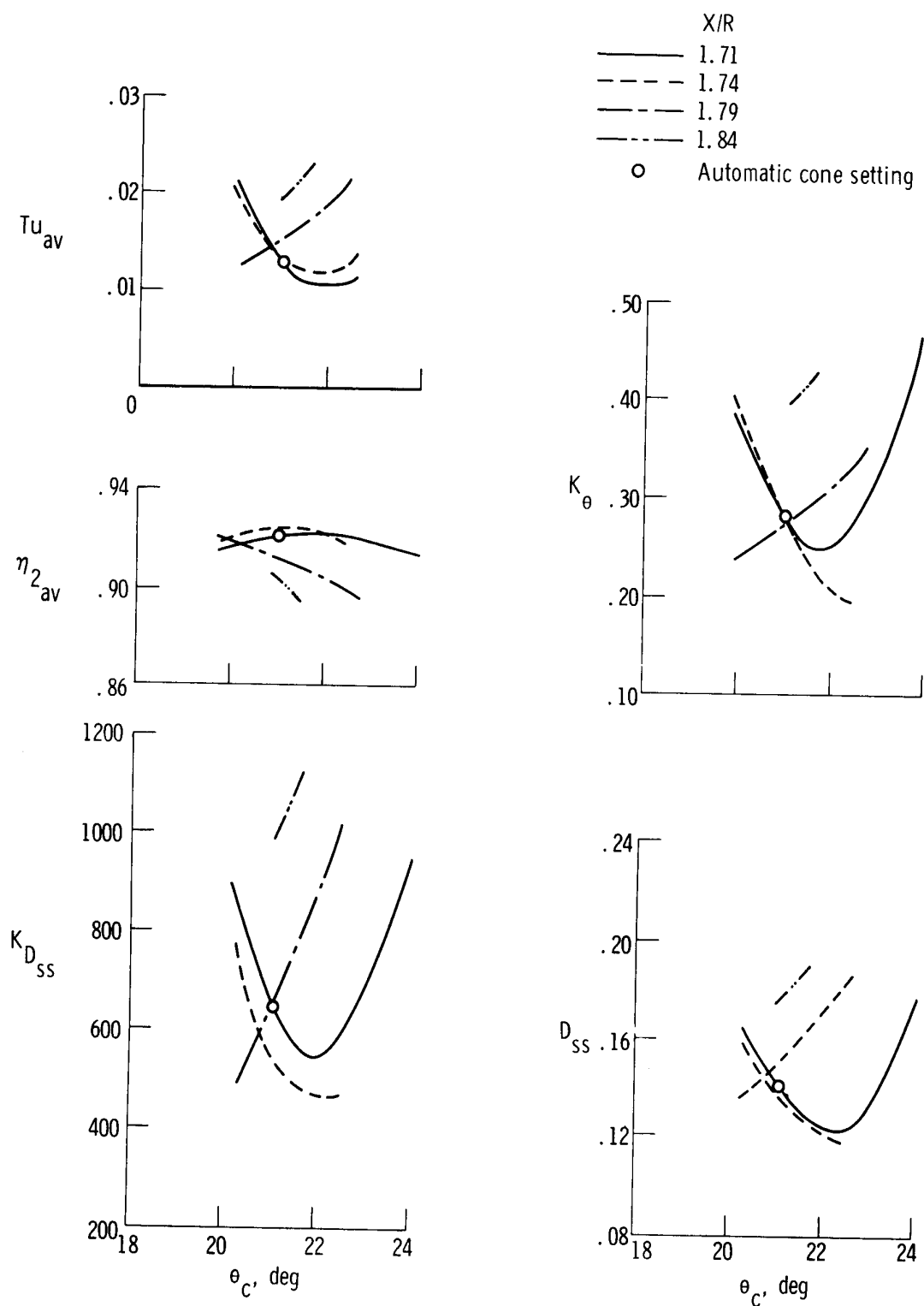


Figure 21. Variation of inlet turbulence, recovery, and distortion parameters during off-schedule operation of the spike and cone. Maximum afterburner;  $M_\infty = 1.82$ ;  $h = 12,192$  meters (40,000 feet);  $m/m_0 = 0.87$ ; F-111A number 12.

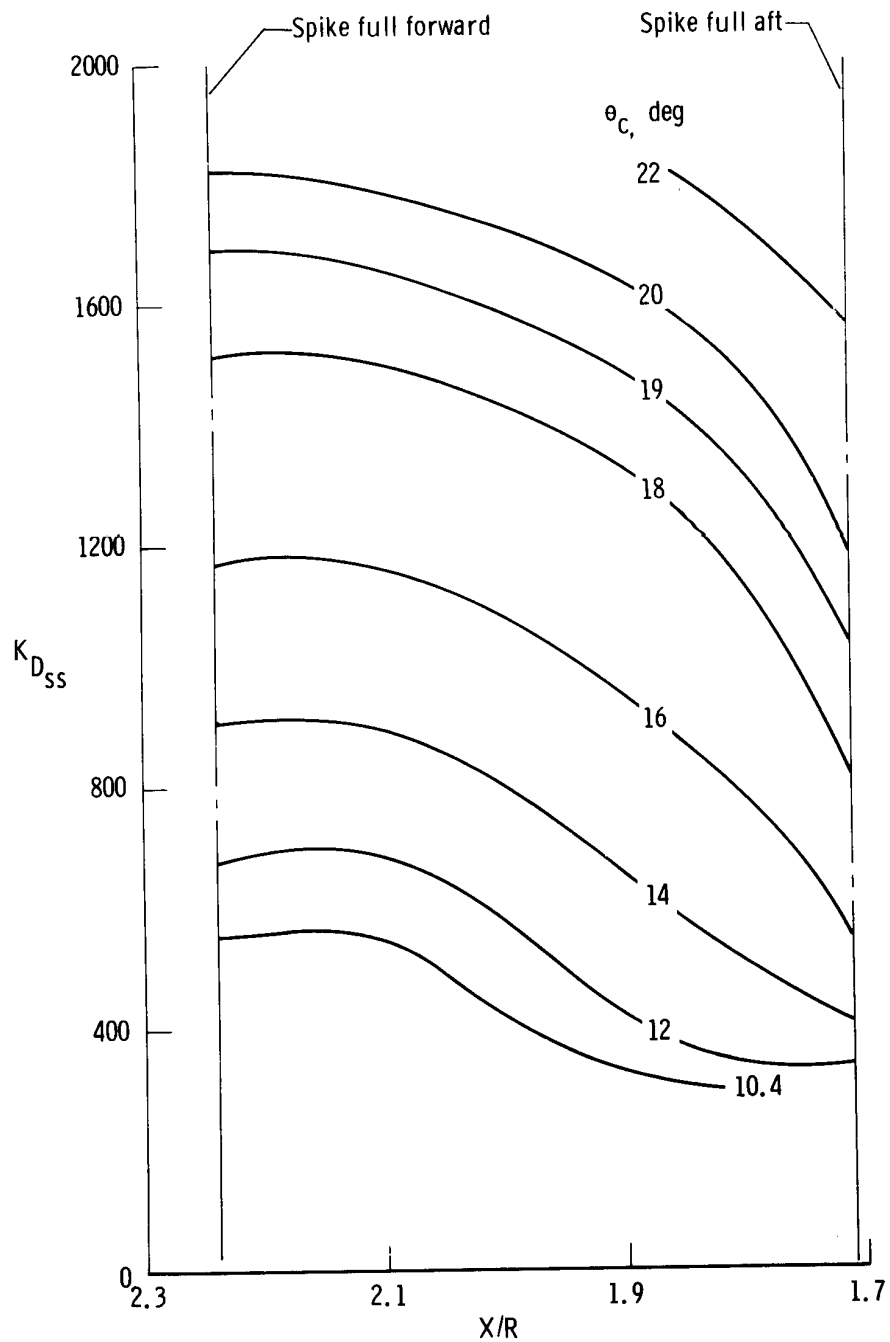
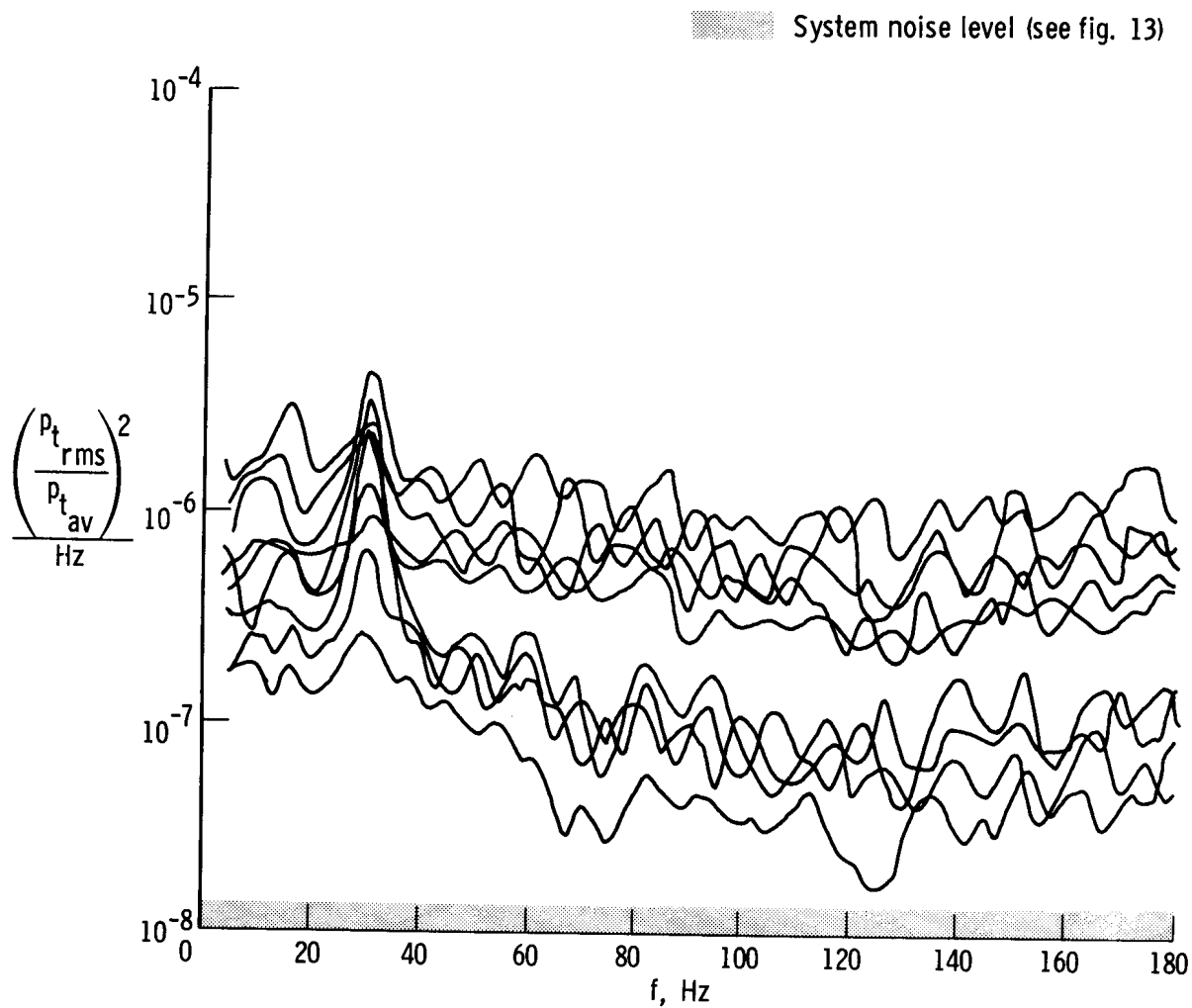


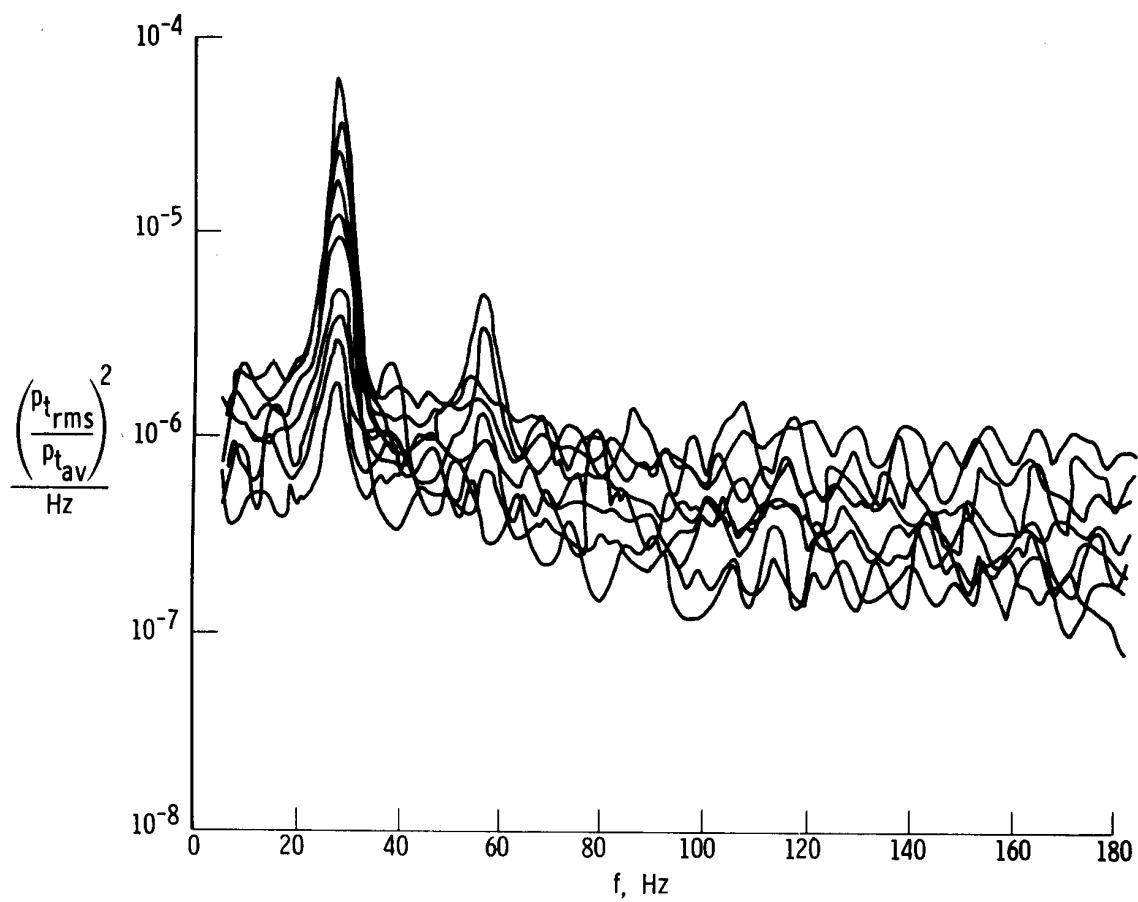
Figure 22. Effect of spike position and cone angle on distortion factor. Military power;  $M_\infty = 0.74$ ;  $h = 2,530$  meters (8,300 feet); F-111A number 12.



(a)  $M_\infty = 1.81$ .

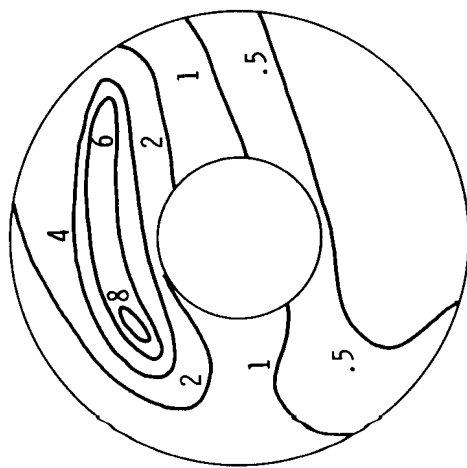
Figure 23. Power spectral density of typical compressor face rake pressures from F-111A number 6.



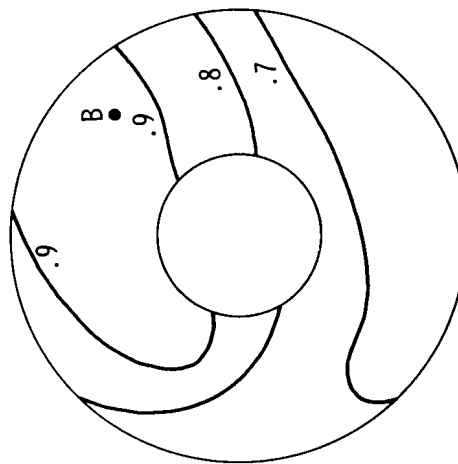


(b)  $M_{\infty} = 2.0$ .

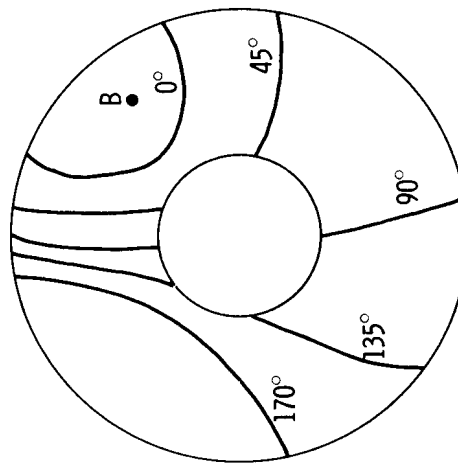
Figure 23. Concluded.



(a) Power at compressor face pressures (numbers are power from power spectral density plots times  $10^{-5}$ , read at 28 hertz).



(b) Coherence between compressor face pressures and pressure at B.



(c) Phase angle between compressor face pressures and pressure at B.

Figure 24. Power, coherence, and phase angle maps for a duct resonance of 28 hertz.  $M_{\infty} = 2.0$ ; F-111A number 6.

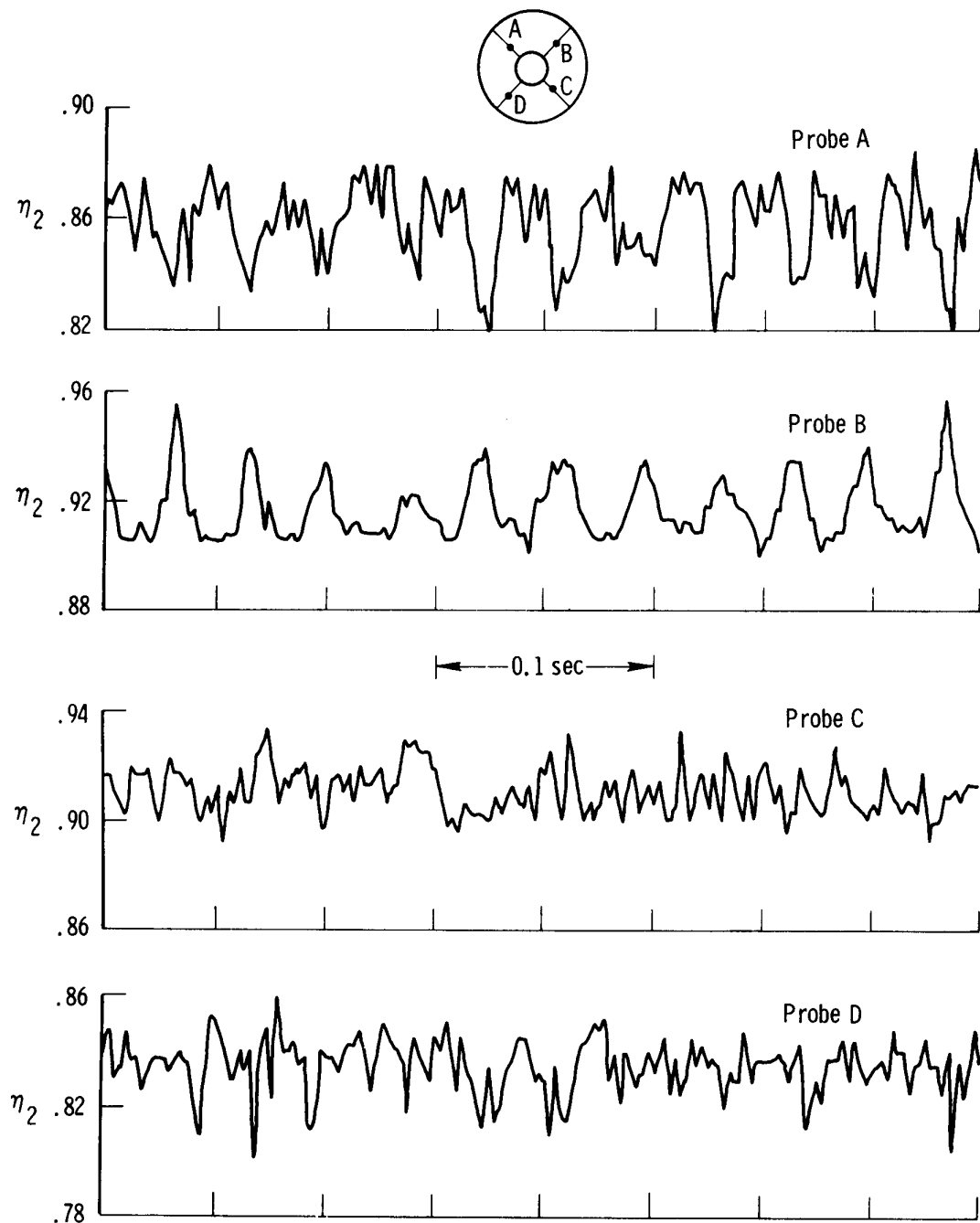


Figure 25. Pressure recovery time histories from four compressor face probes during inlet duct resonance.  $M_\infty = 2.0$ ; F-111A number 6.

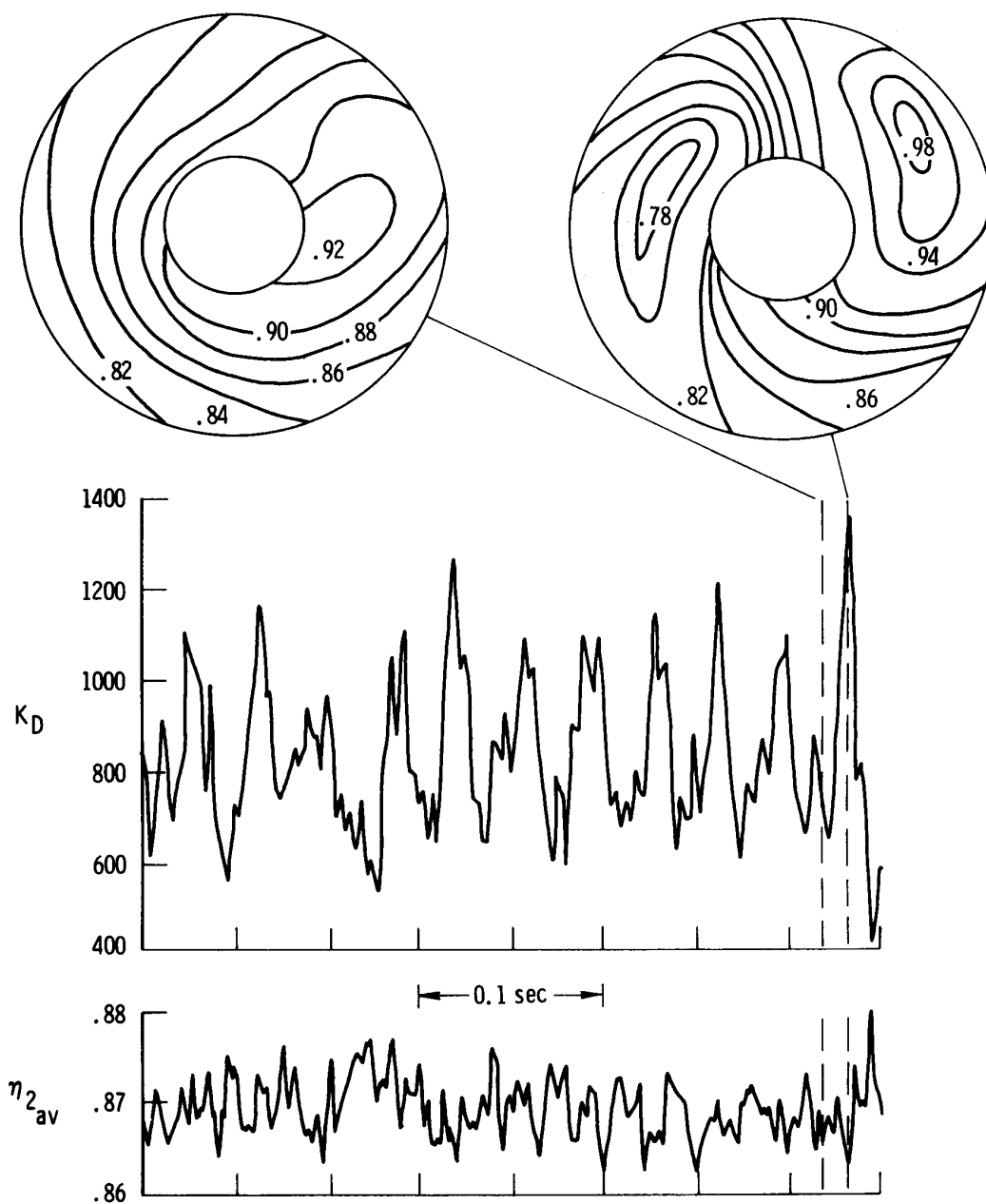


Figure 26. Pressure recovery and  $K_D$  time histories and instantaneous recovery maps during inlet duct resonance.  $M_\infty = 2.0$ ; F-111A number 6.

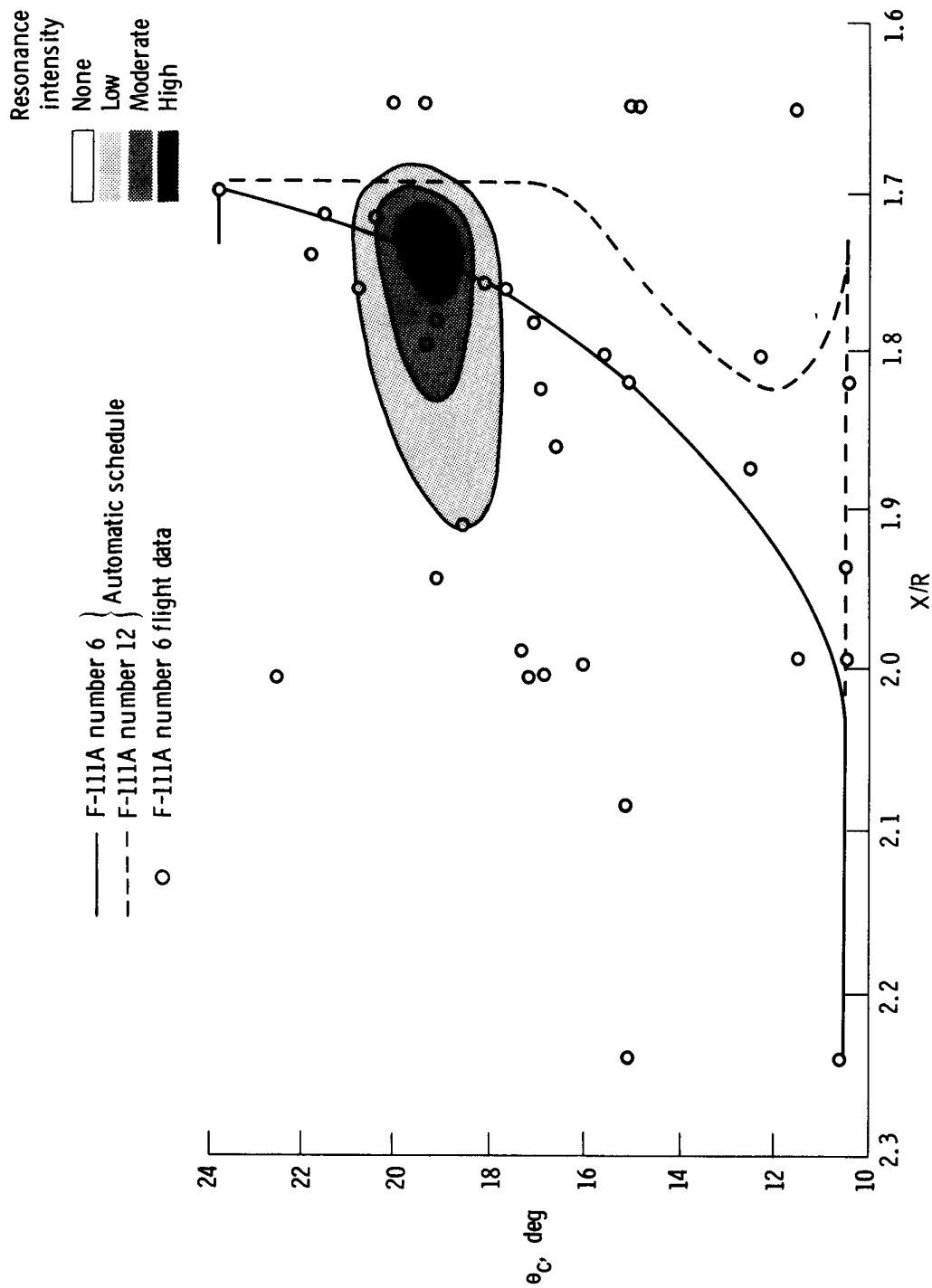
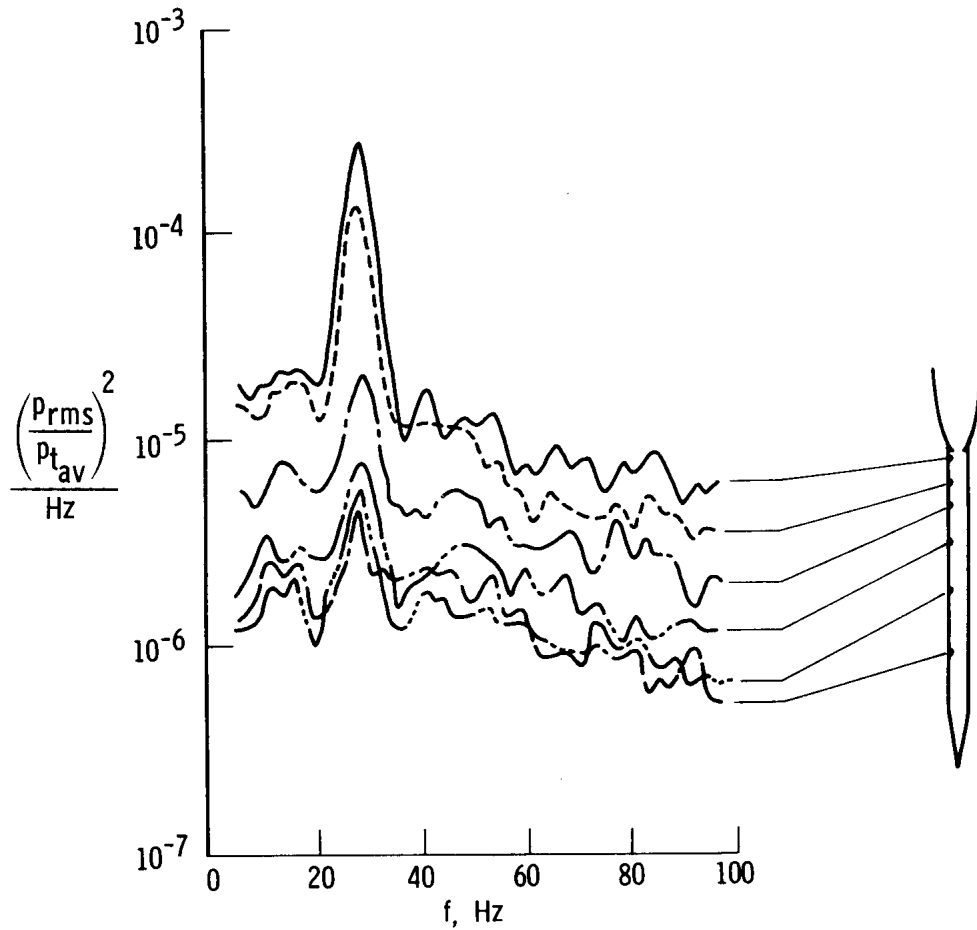
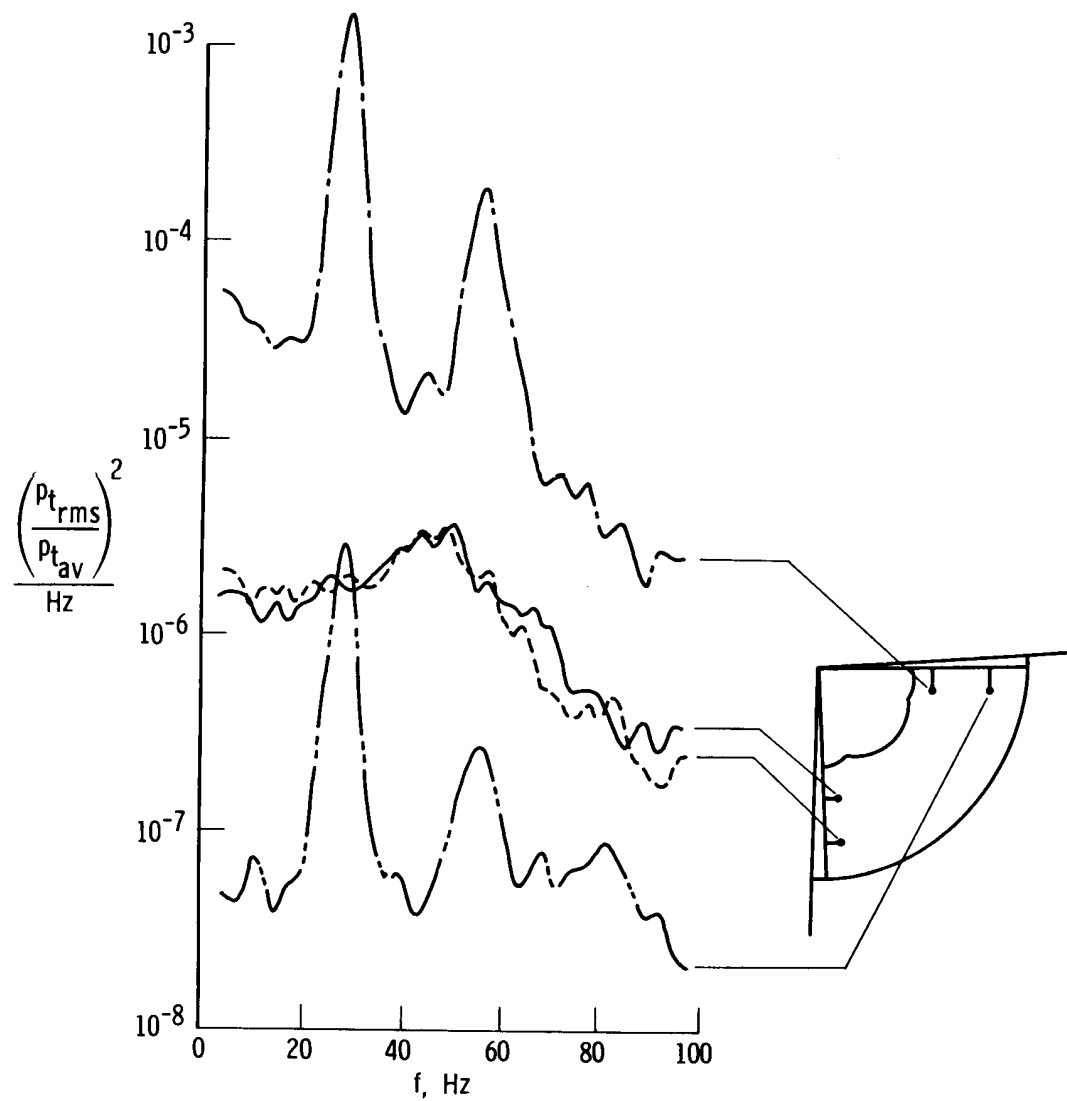


Figure 27. Effect of spike and cone position on the intensity of resonance.



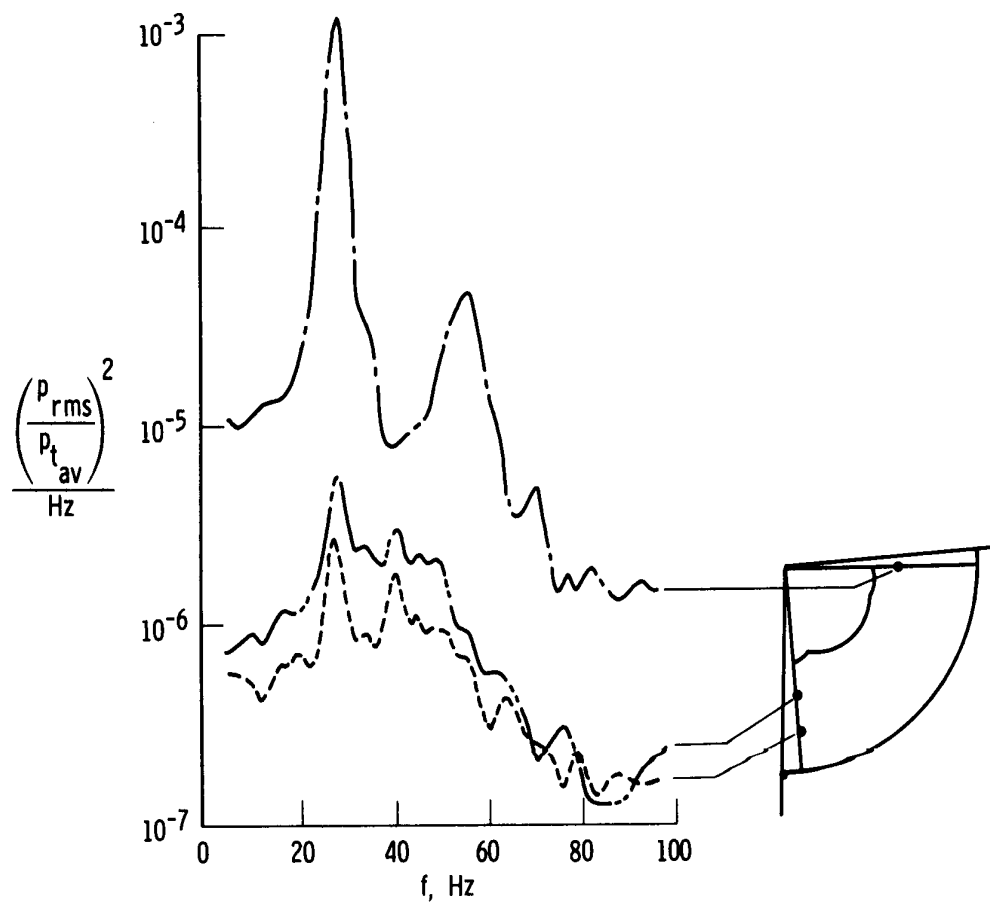
(a) Shock position probe static pressures.

Figure 28. Power spectral density plots of propulsion system pressures during duct resonance.  $M_{\infty} = 2.0$ ; F-111A number 6.



(b) Cowl lip total pressures.

Figure 28. Continued.



(c) Cowl lip static pressures.

Figure 28. Continued.



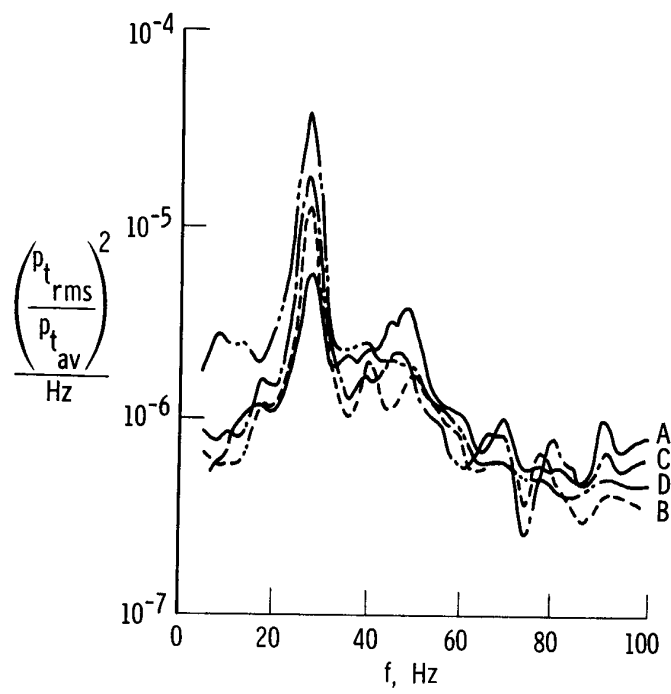
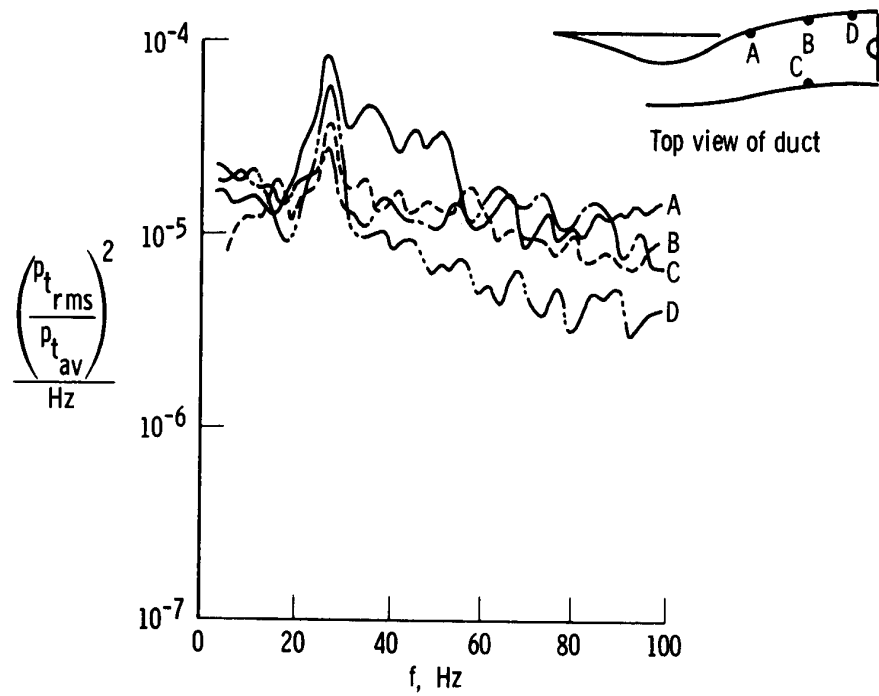
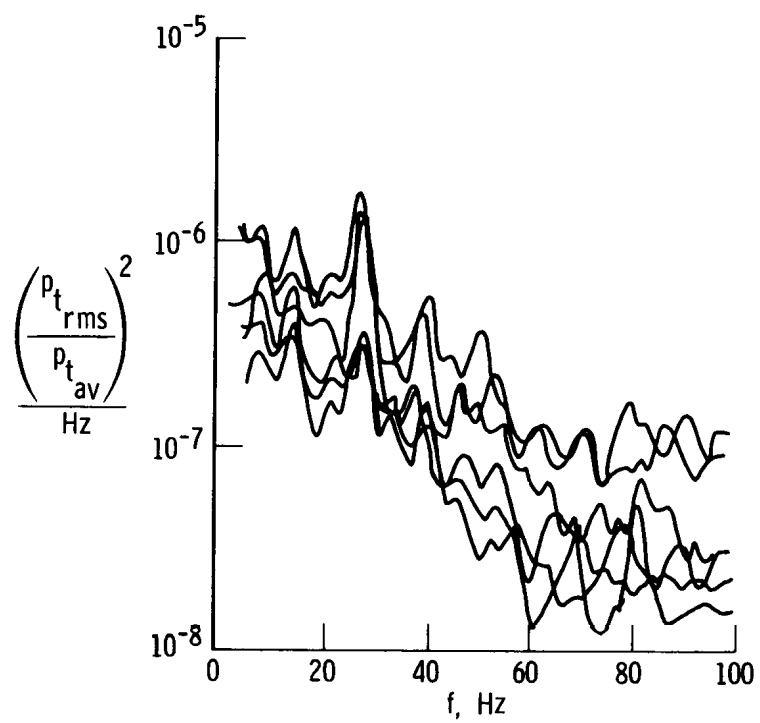


Figure 28. Continued.



(f) Fan duct total pressures.

Figure 28. Concluded.

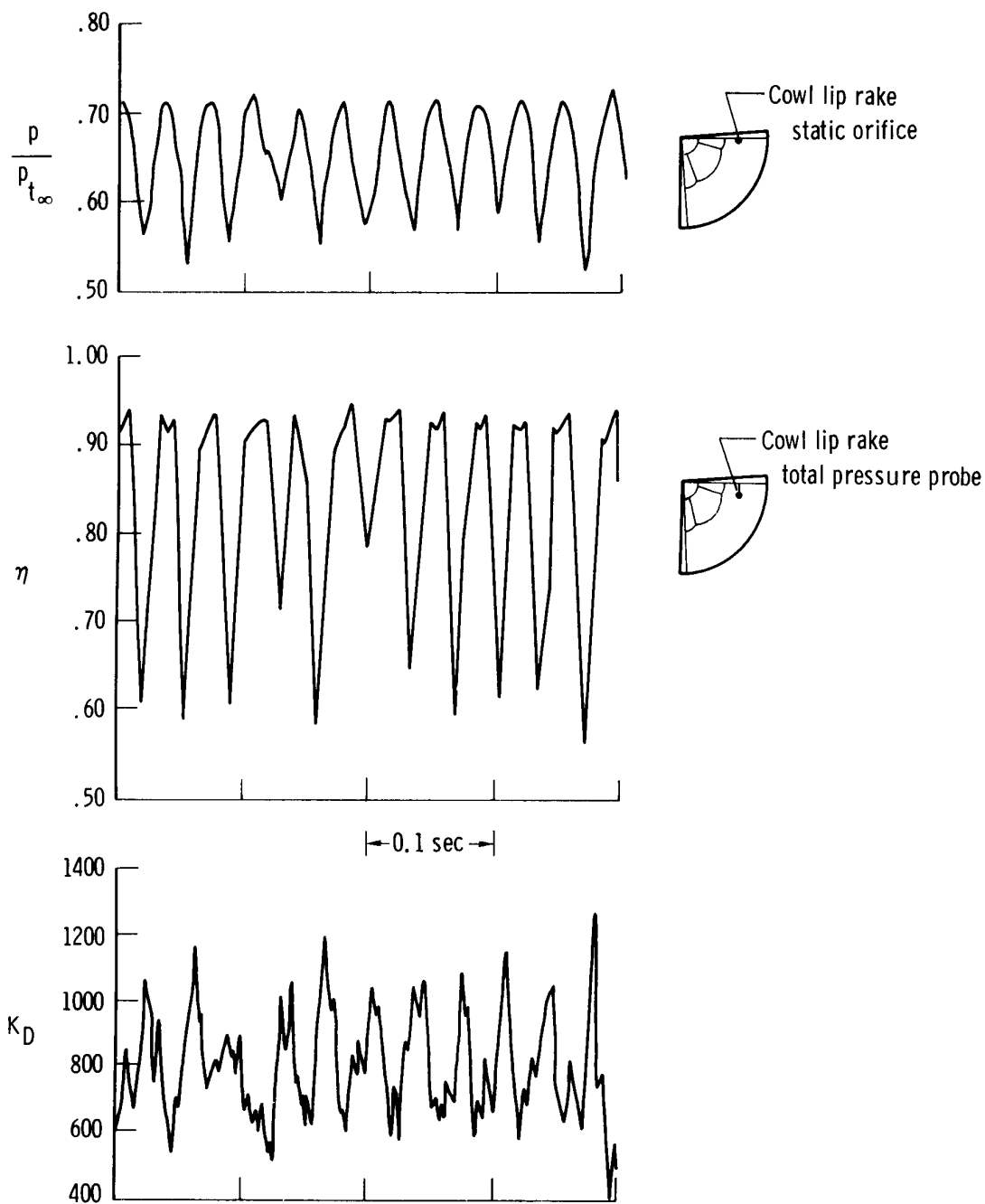


Figure 29. Cowl lip rake static pressure to free-stream total pressure ratio, total pressure recovery, and compressor face distortion factor during inlet resonance.  $M_\infty = 2.0$ ; F-111A number 6.

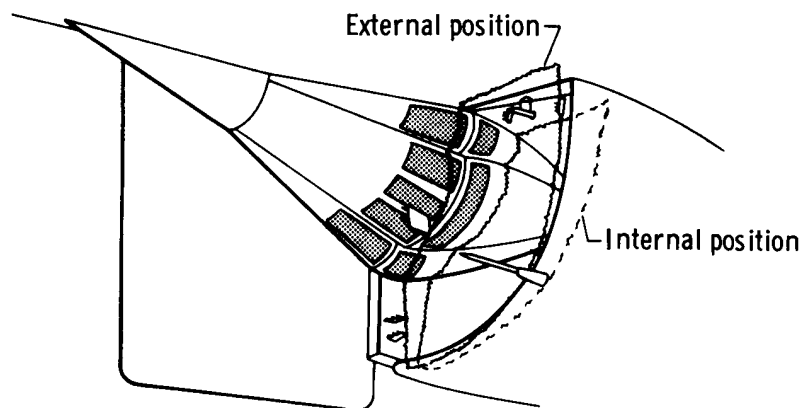


Figure 30. Sketch of the inlet showing the normal shock movement from the external to internal position during duct resonance.  $M_\infty = 2.0$ ; F-111A number 6.

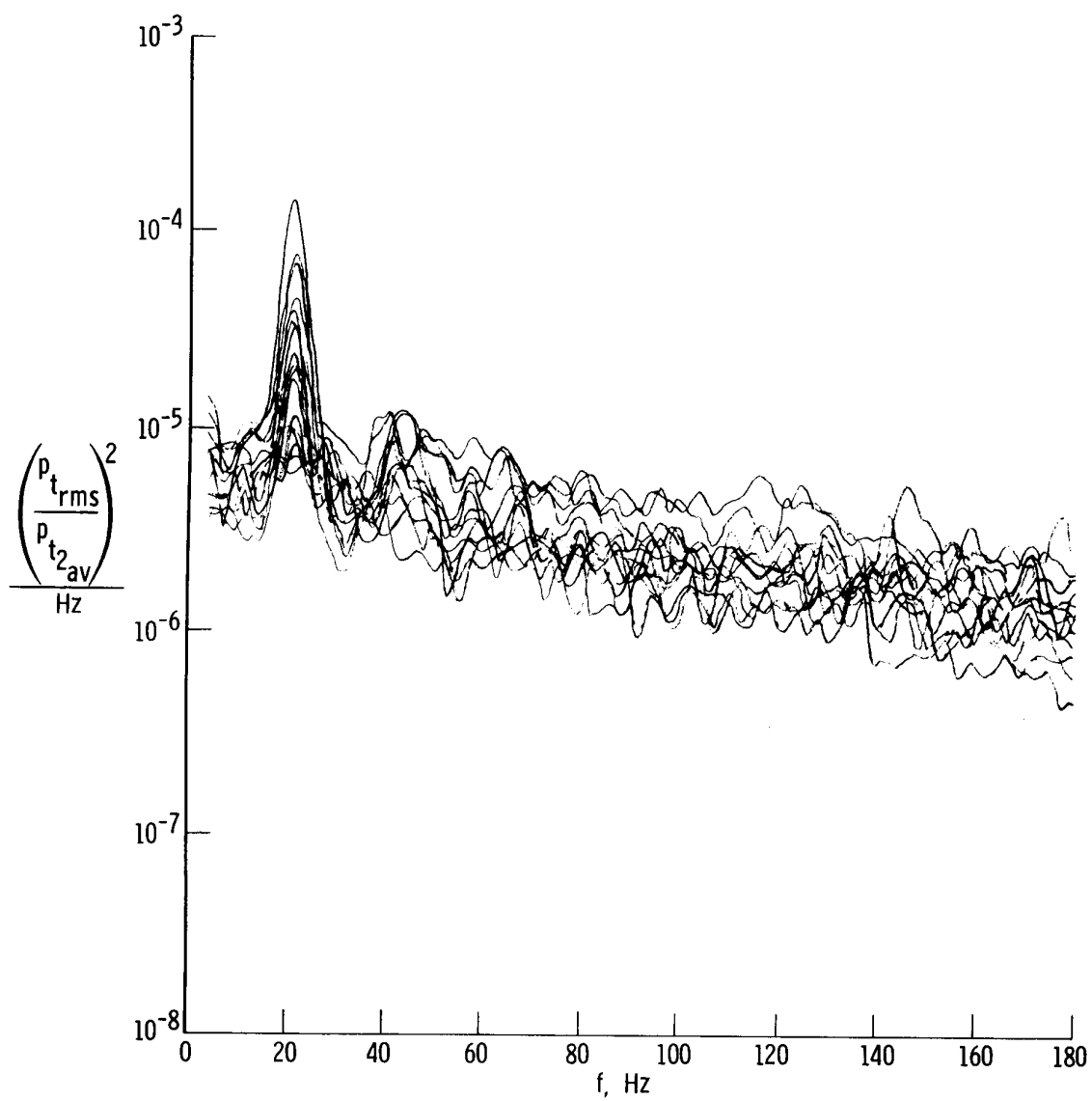
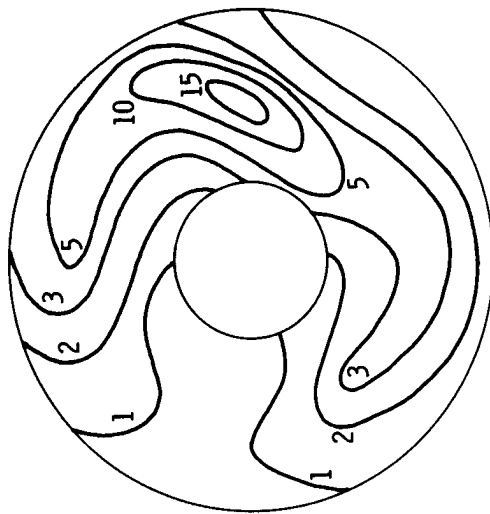
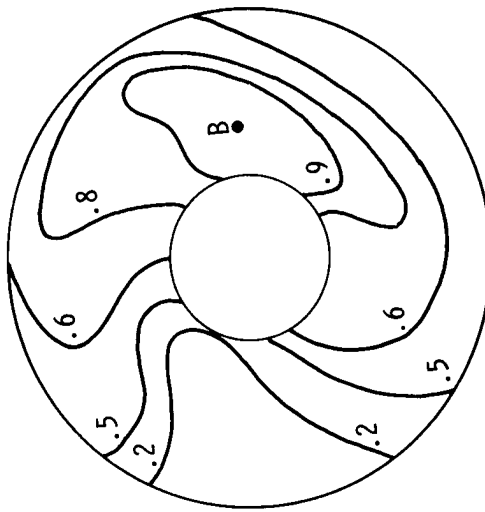


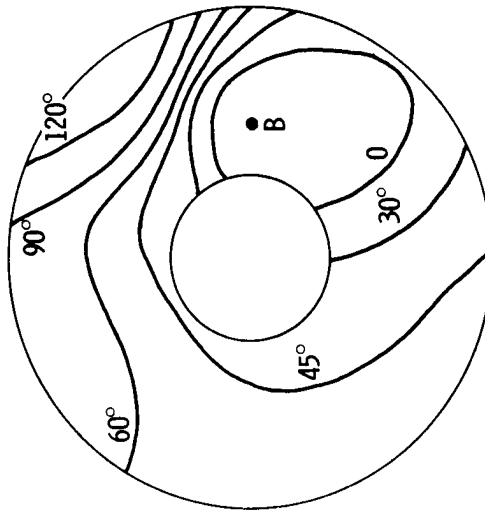
Figure 31. Power spectral density plot of typical compressor face pressures during duct resonance.  $M_\infty = 2.32$ ; F-111A number 12.



(a) Power at compressor face pressures (numbers are power from power spectral density plots times  $10^{-5}$ , read at 23 hertz).

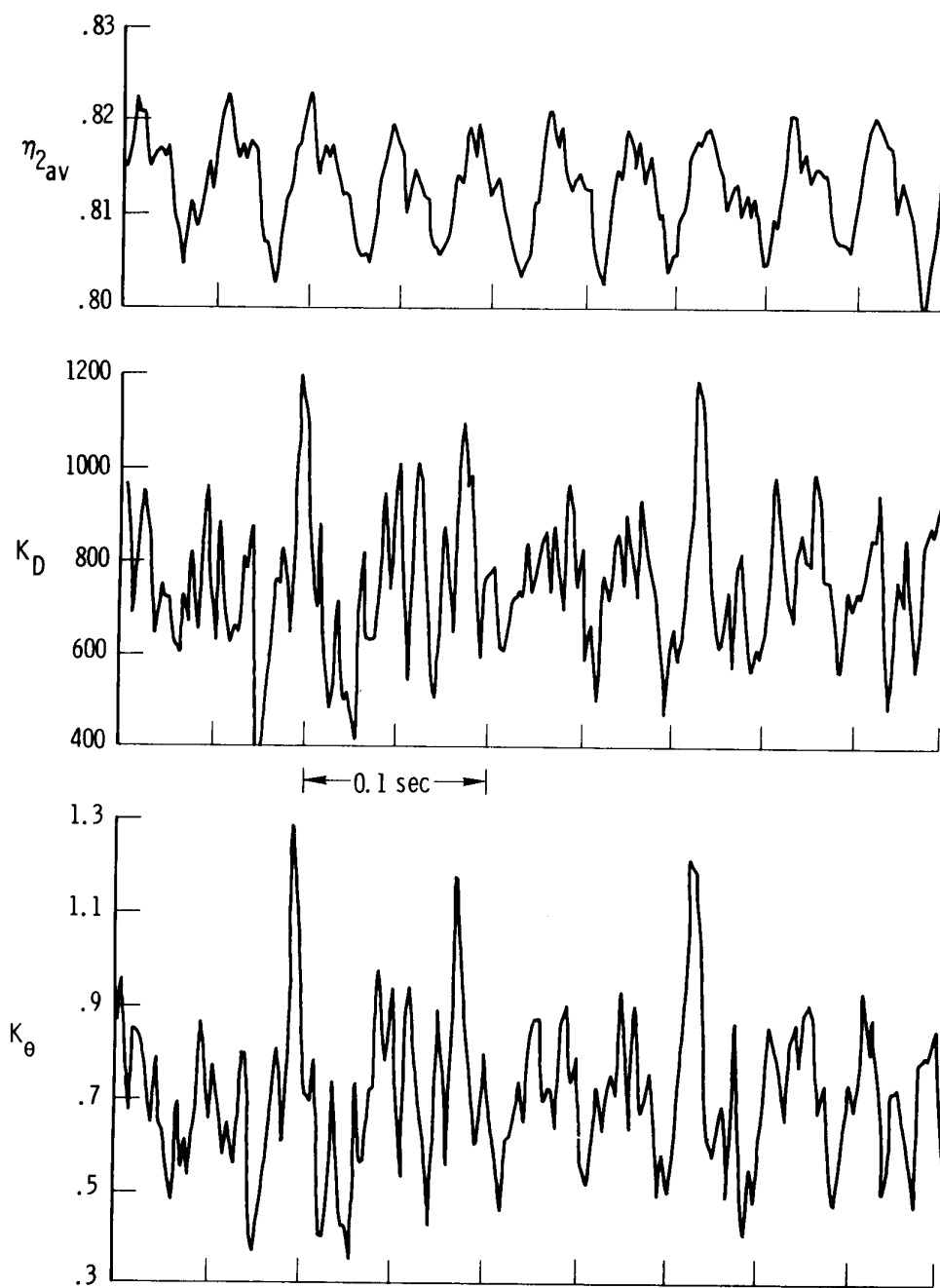


(b) Coherence between compressor face pressures and pressure at B.



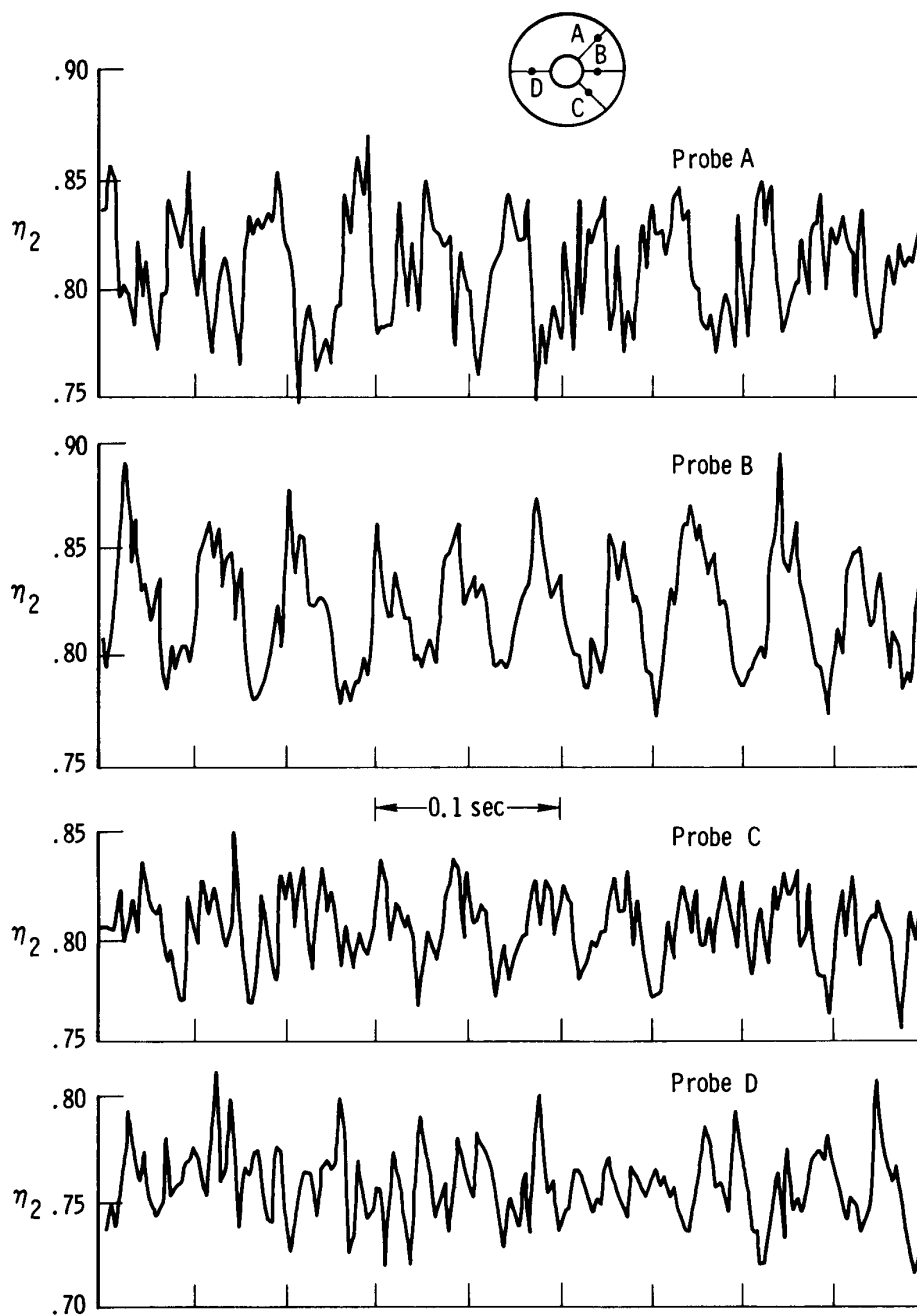
(c) Phase angle between compressor face pressures and pressure at B.

Figure 32. Power, coherence, and phase angle maps for a duct resonance of 23 hertz.  $M_{\infty} = 2.32$ ; F-111A number 12.



(a)  $\eta_{2av}$ ,  $K_D$ , and  $K_\theta$ .

Figure 33. Time histories of pressure recoveries and distortion factors during duct resonance.  $M_\infty = 2.32$ ; F-111A number 12.



(b) Pressure probe recoveries.

Figure 33. Concluded.



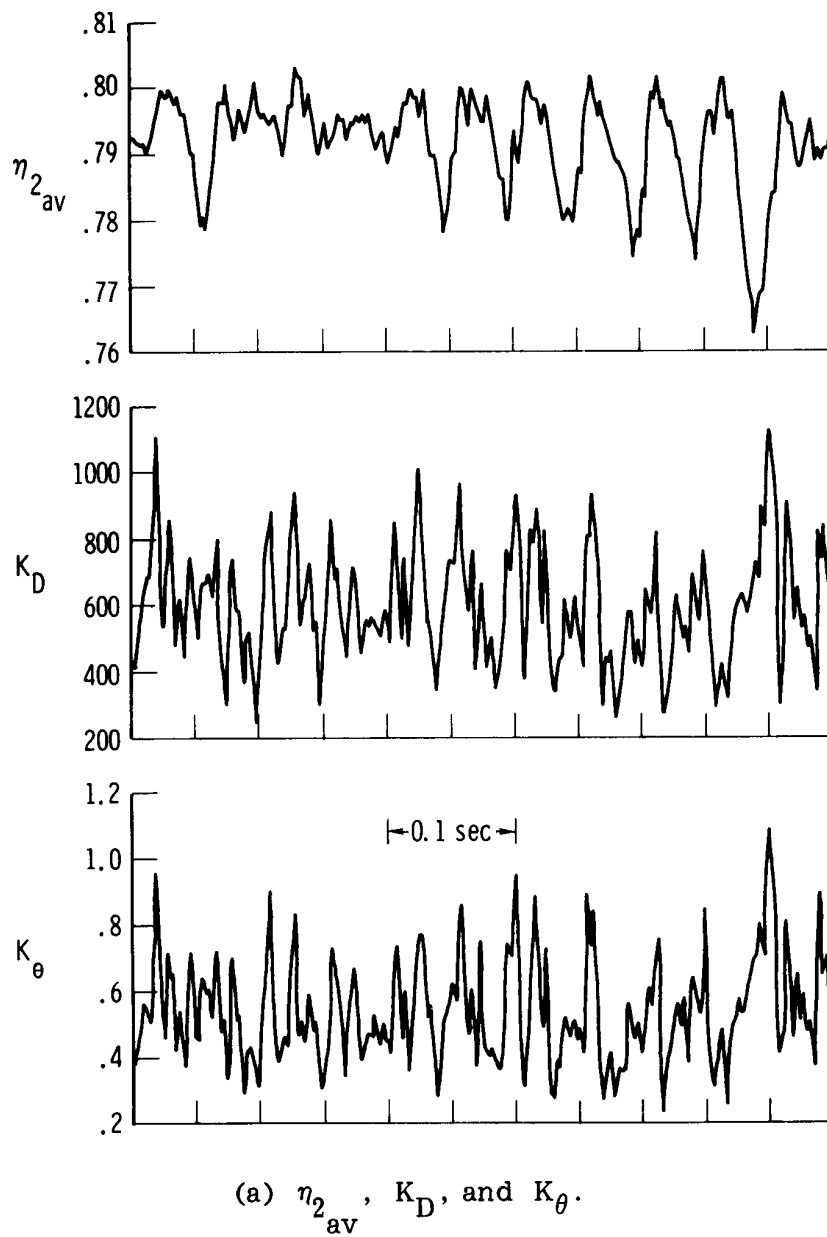
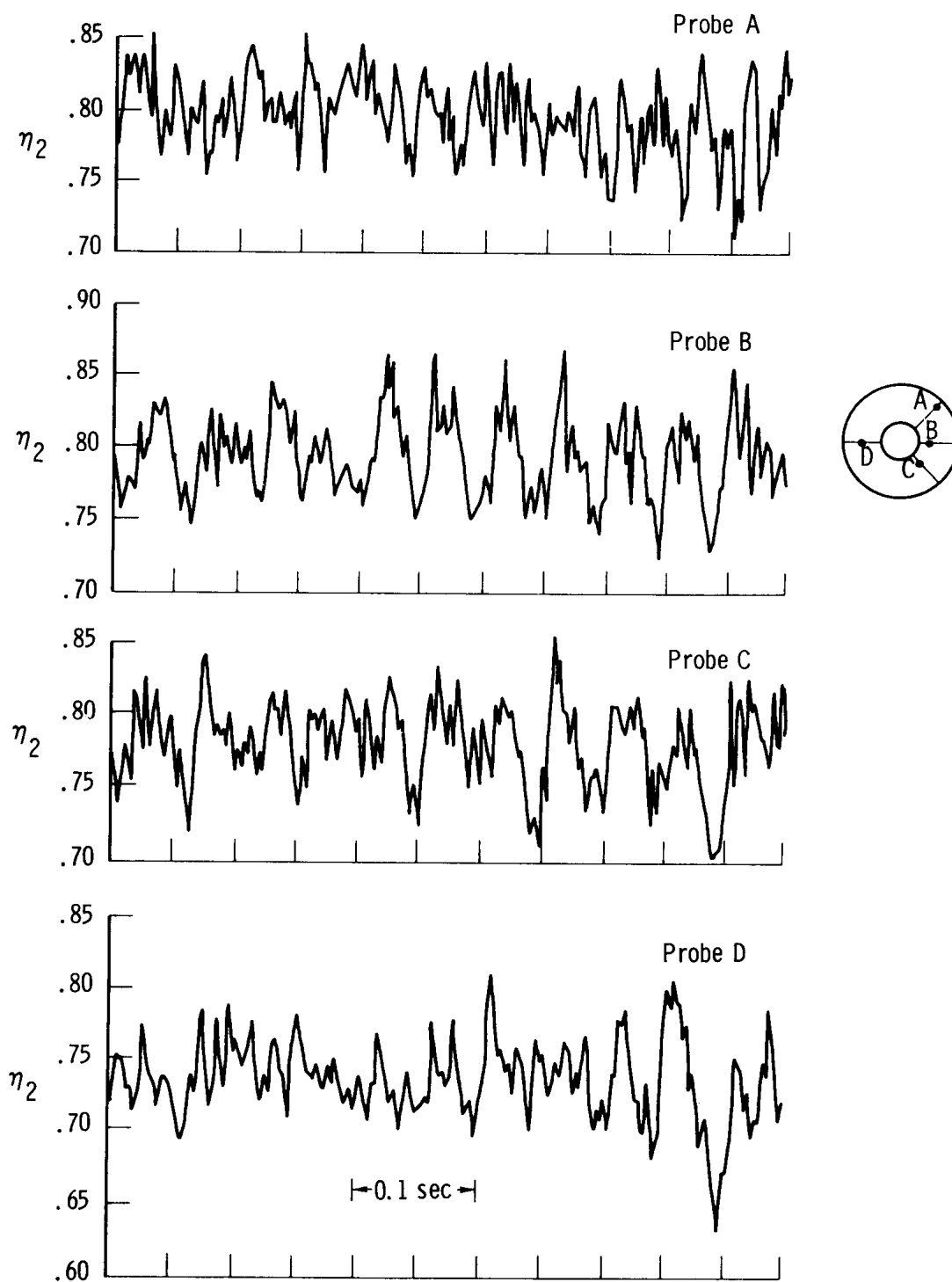


Figure 34. Time histories of pressure recovery and distortion factors and pressure probe recoveries during duct resonance.  $M_\infty = 2.38$ ; F-111A number 12.



(b) Pressure probe recoveries.

Figure 34. Concluded.

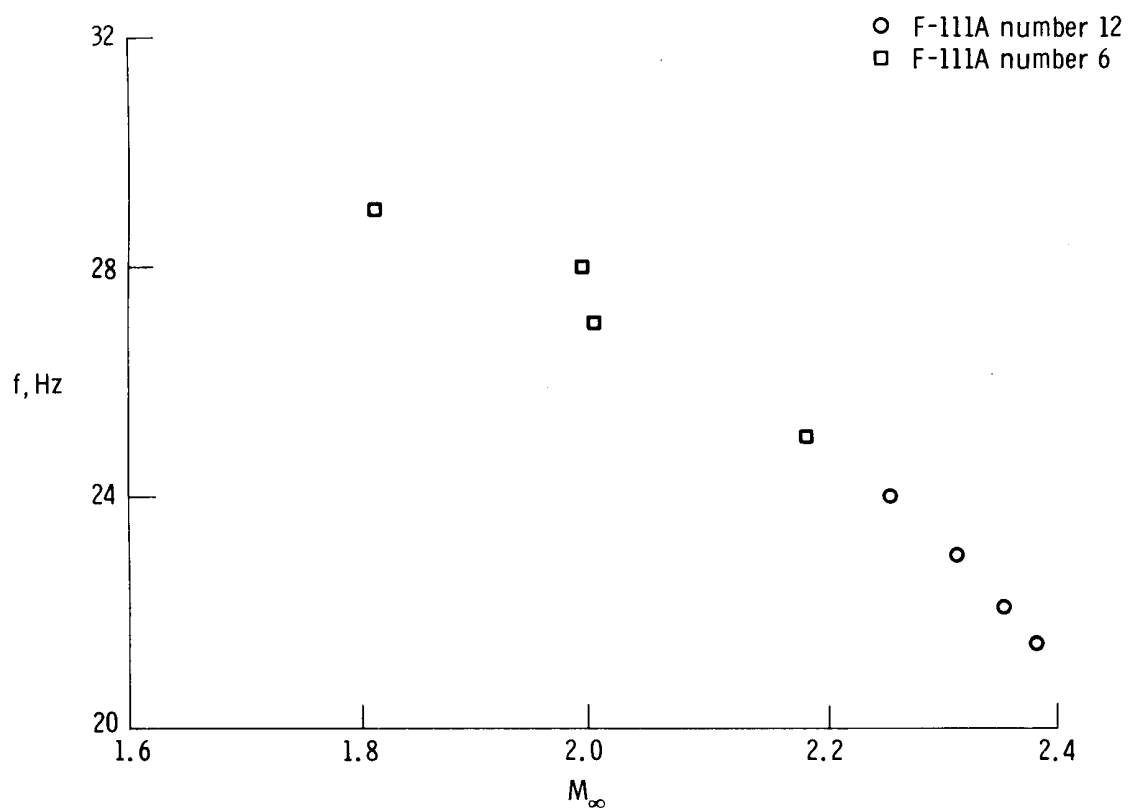


Figure 35. Resonant frequency as a function of Mach number.

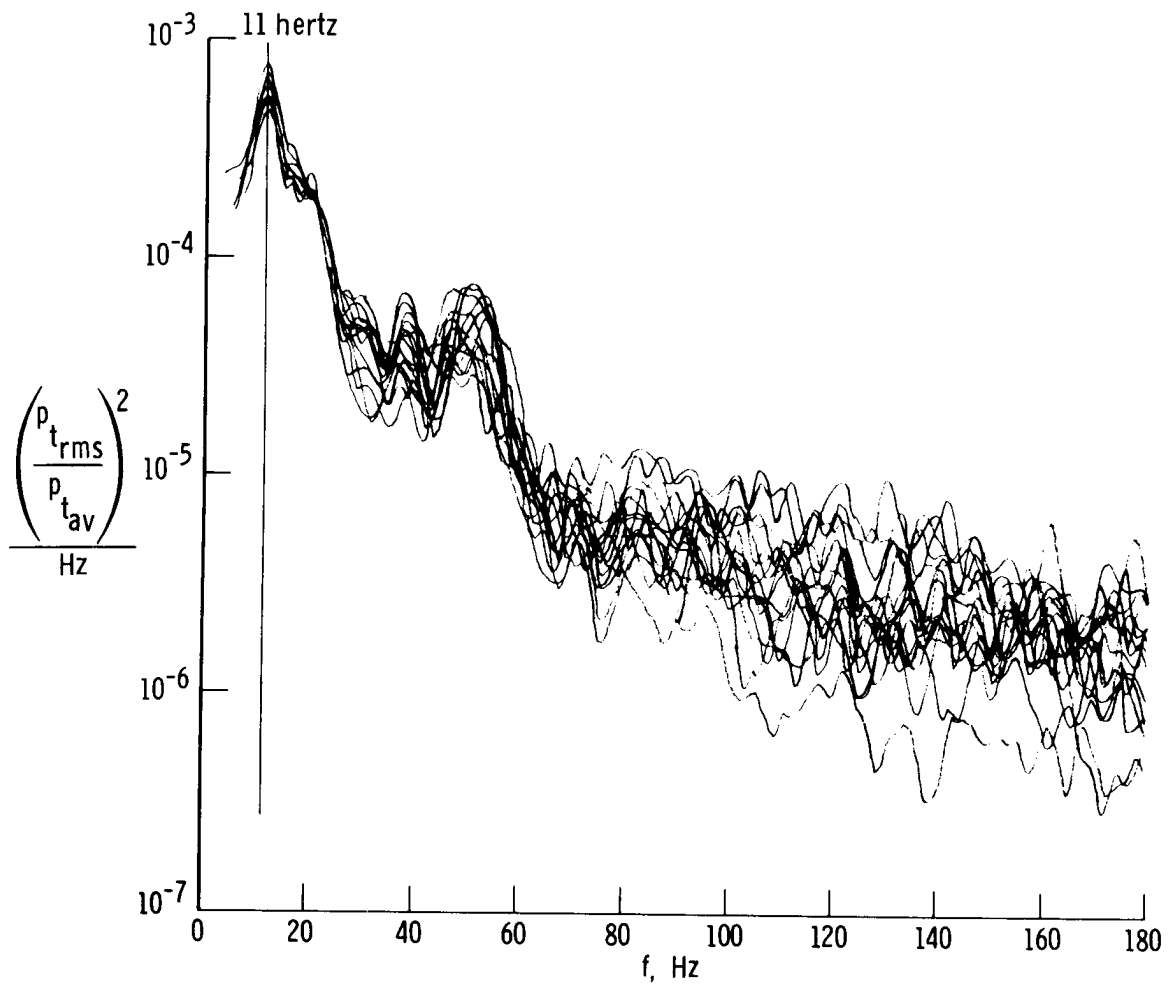
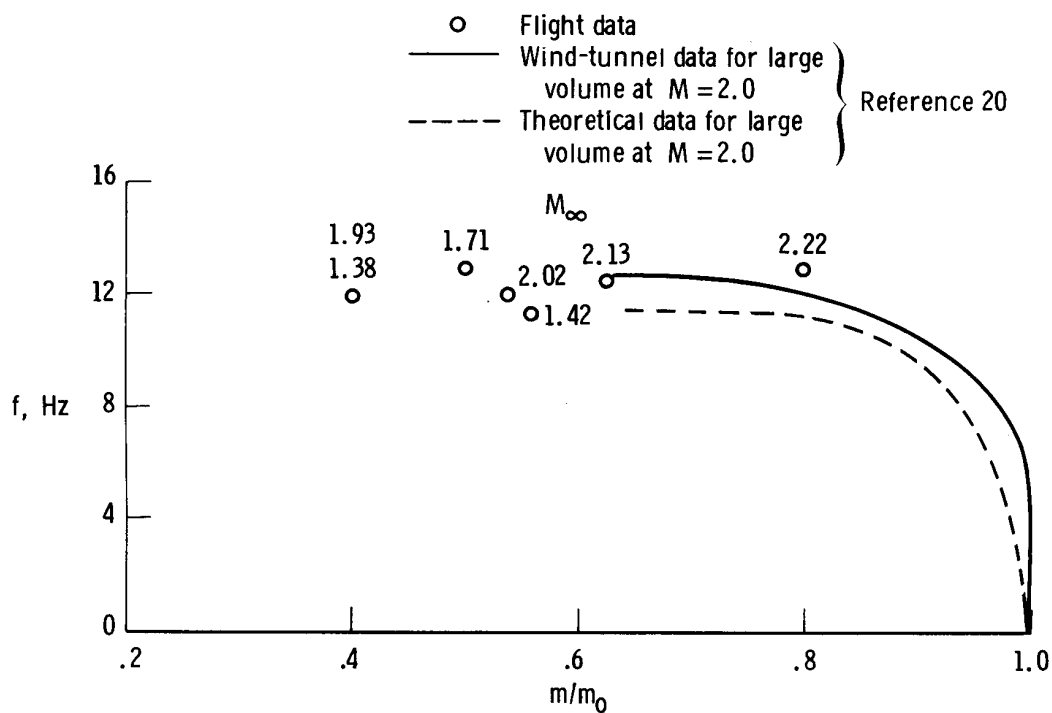
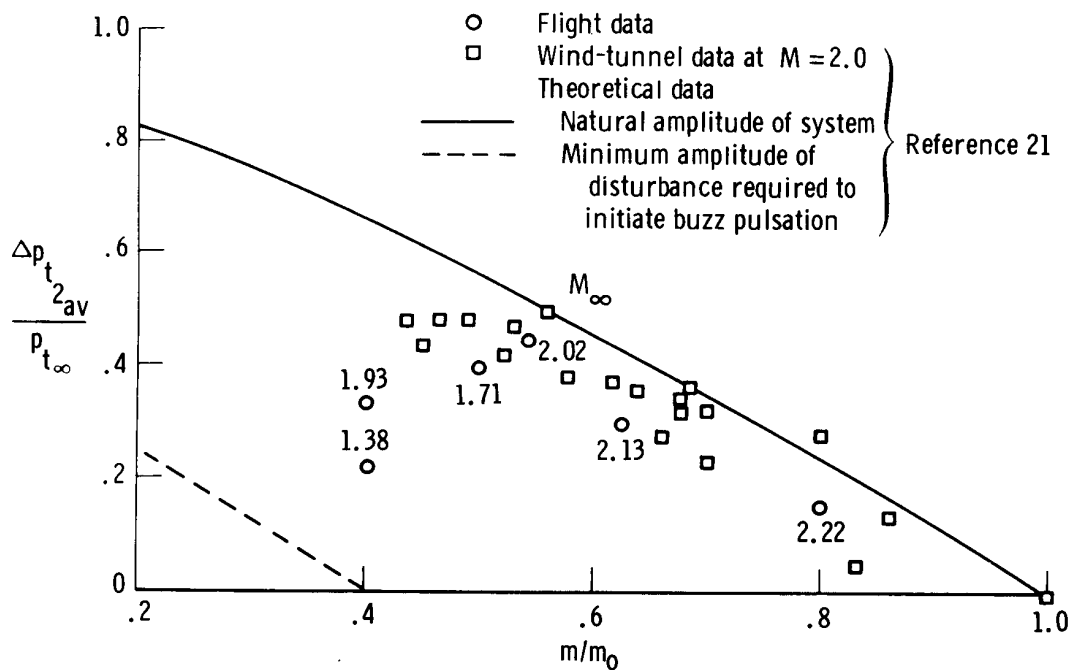


Figure 36. Power spectral density plot of compressor face pressures during inlet duct buzz.  $M_\infty = 1.4$ ; F-111A number 12.



(a) Buzz frequency.



(b) Buzz amplitude.

Figure 37. Effect of mass flow ratio on buzz frequency and amplitude for F-111A number 12. Mach numbers shown are for flight data.

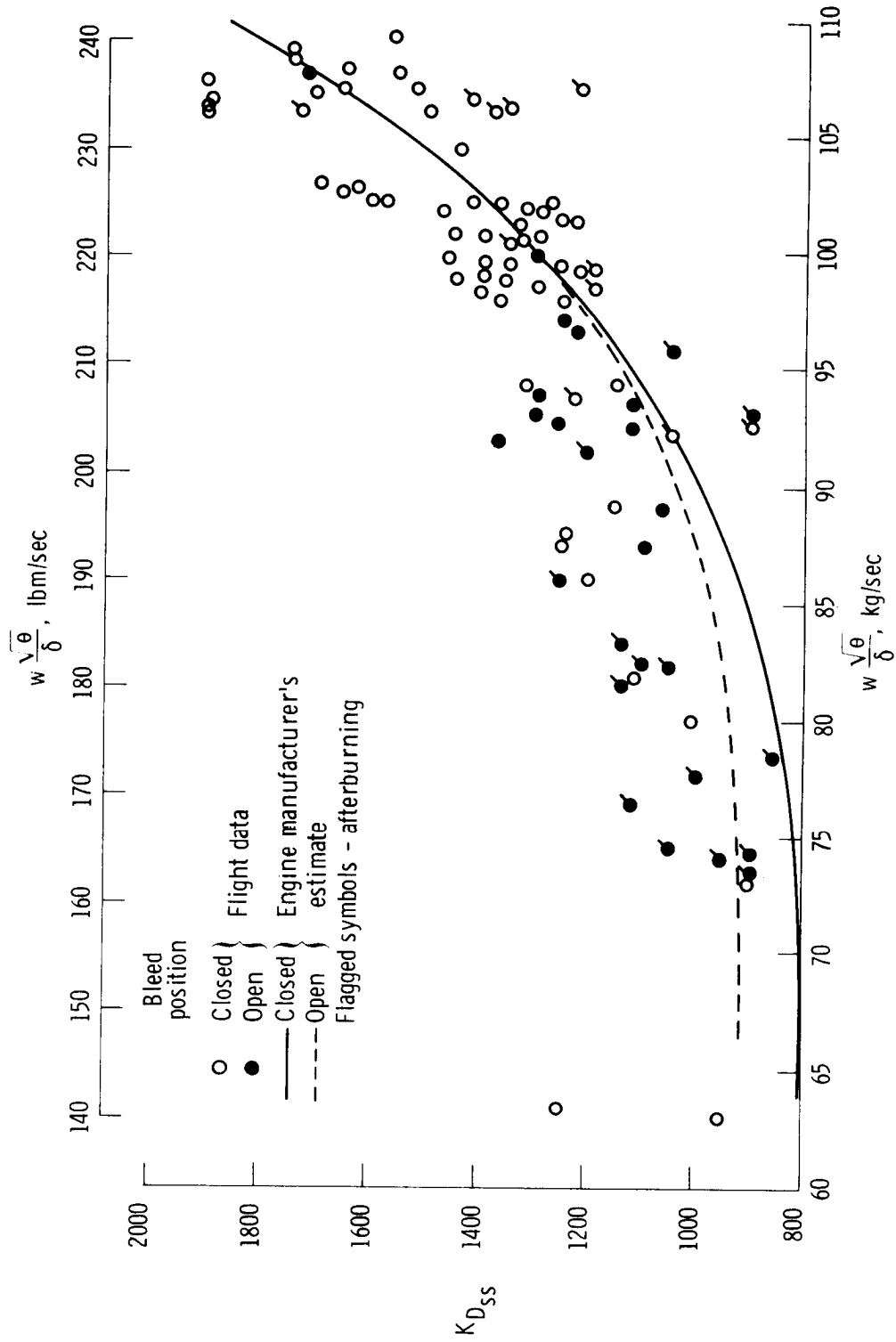


Figure 38. Effect of corrected airflow on steady-state  $K_D$  prior to stall. All data adjusted to  $Re_i = 1.0$ ; F-111A number 12.

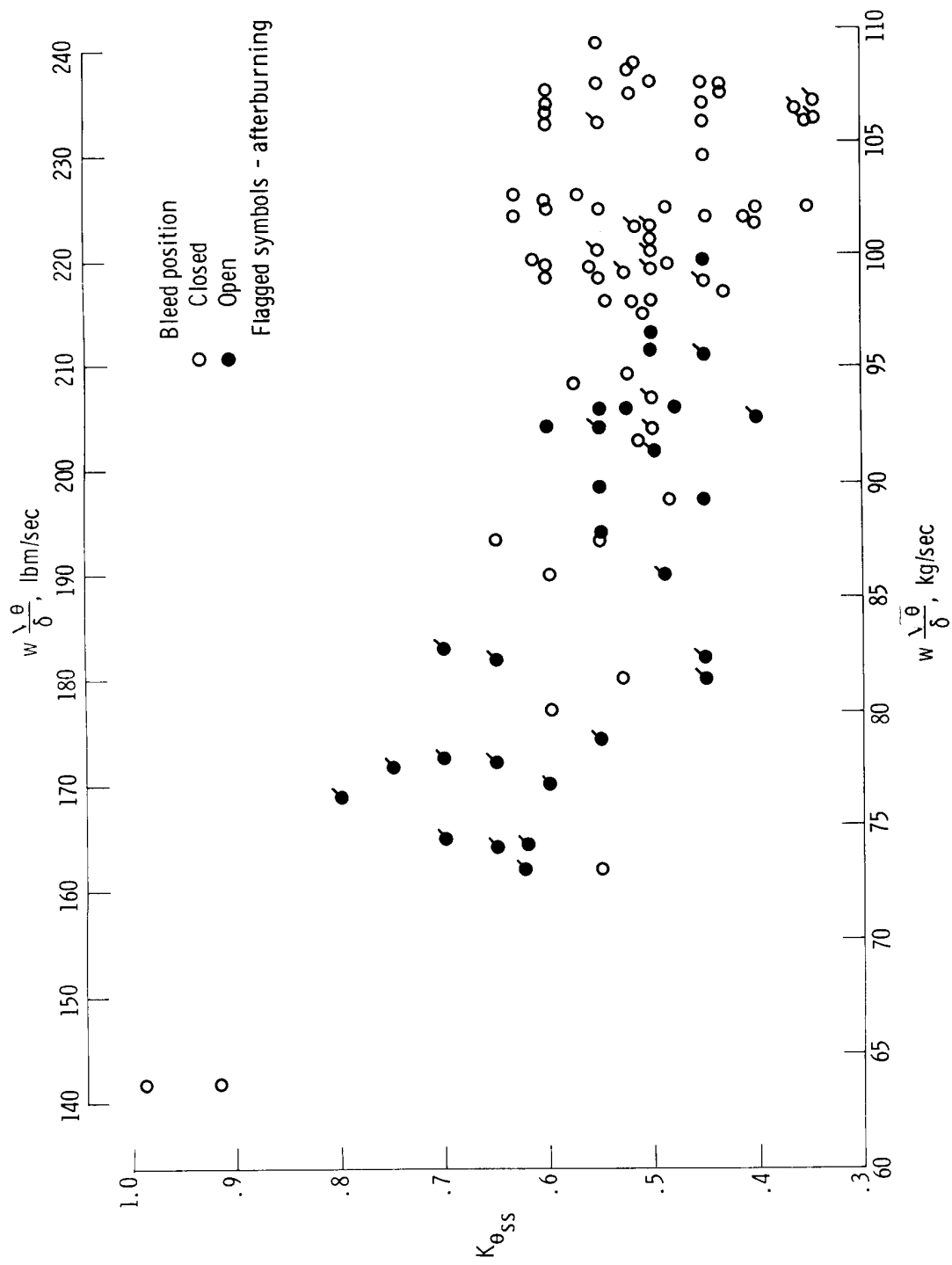


Figure 39. Effect of corrected airflow on steady-state  $K_{\theta}$  prior to stall. F-111A number 12.

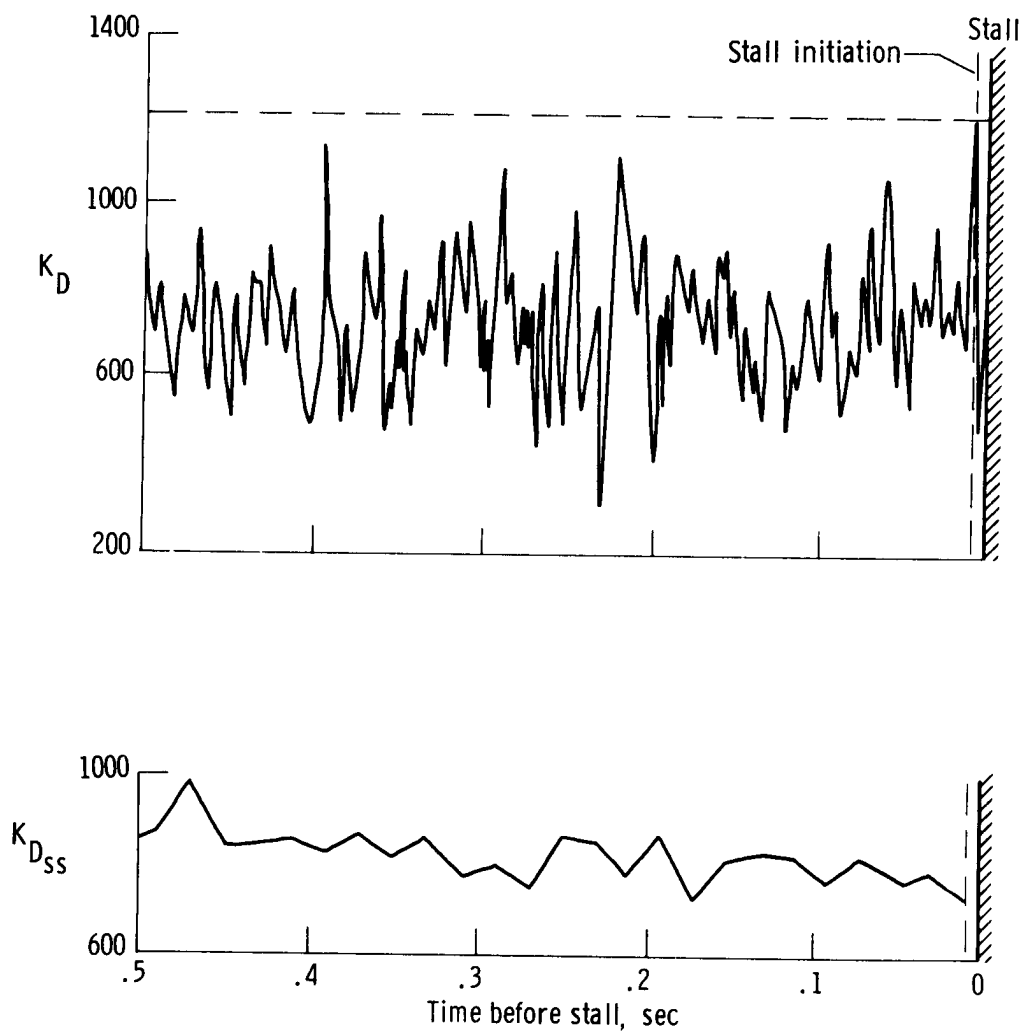


Figure 40. Steady-state and instantaneous distortion factors for a compressor stall.  $M_\infty = 1.60$ ;  $h = 13,700$  meters (45,000 feet).



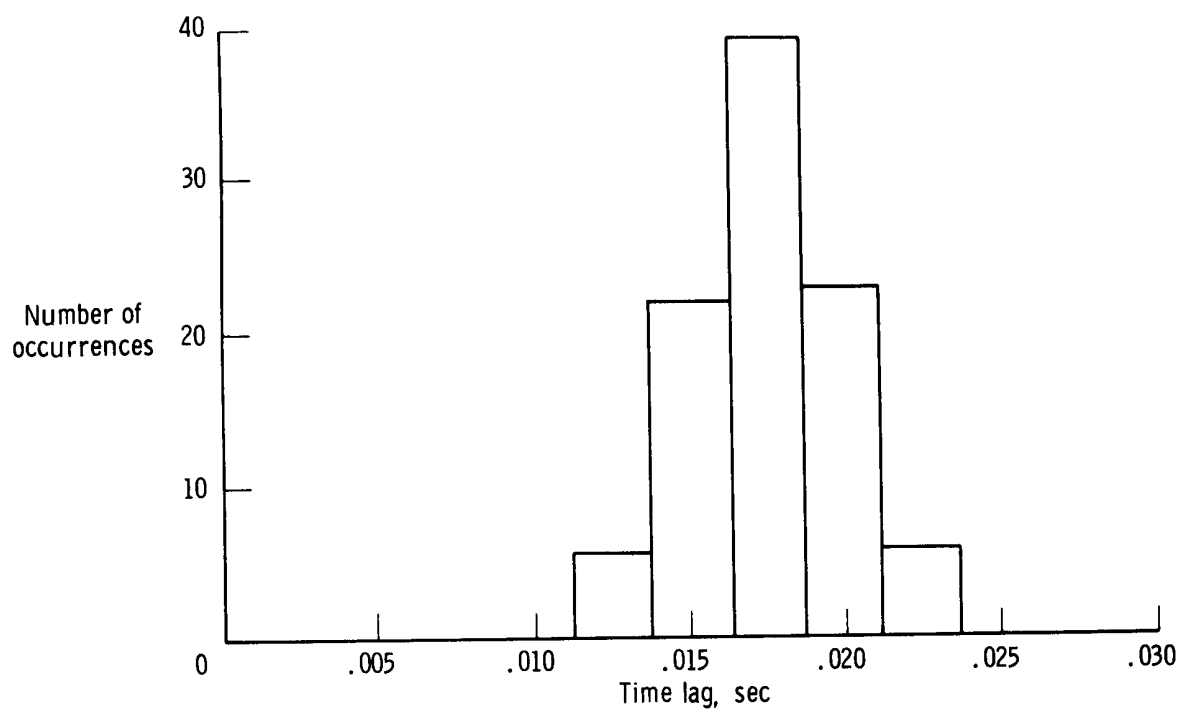


Figure 41. Time between distortion peak and hammer shock wave.

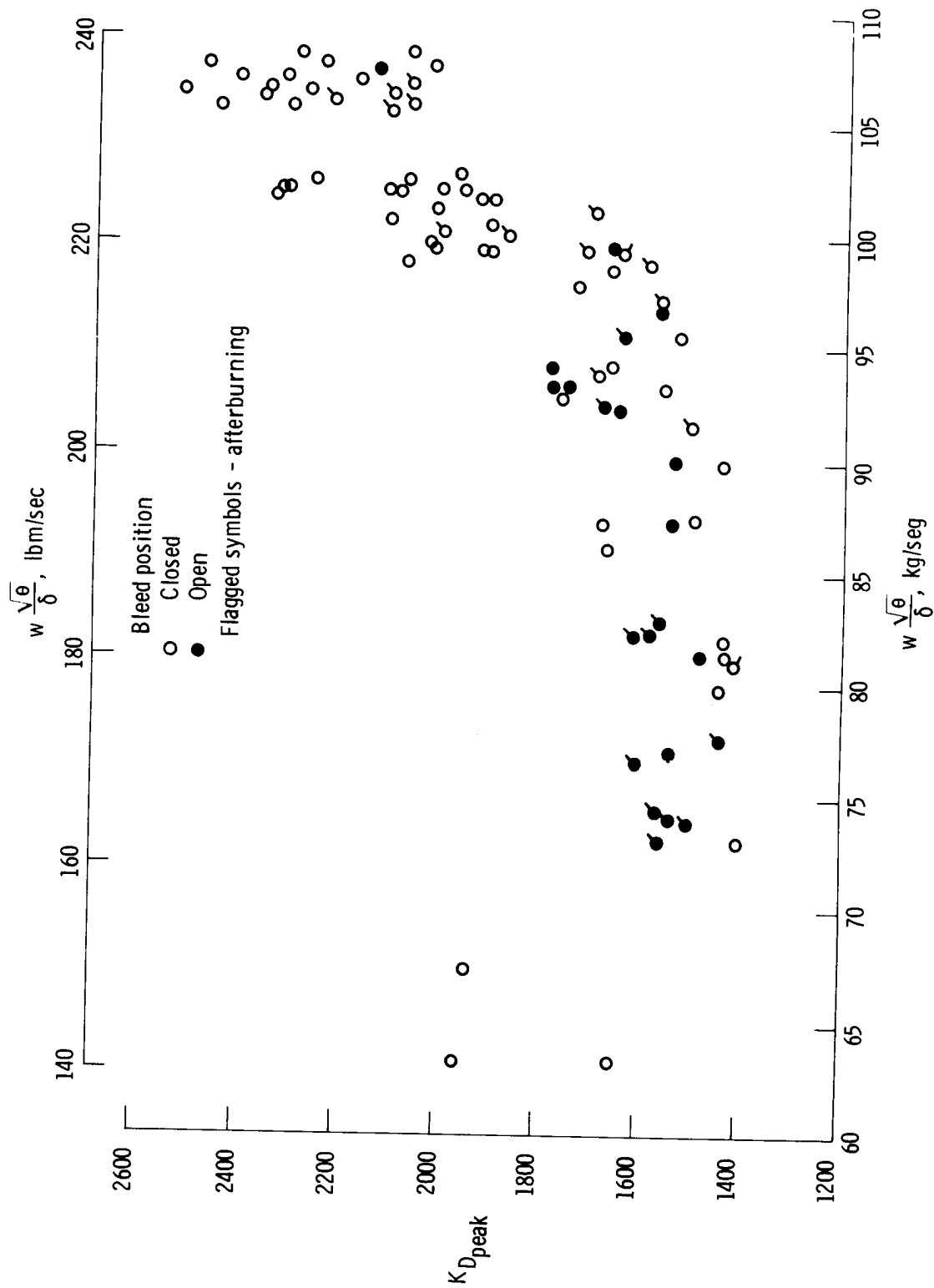


Figure 42. Effect of corrected airflow on peak instantaneous  $K_D$  prior to stall. All data adjusted to  $Re_i = 1.0$ ; F-111A number 12.

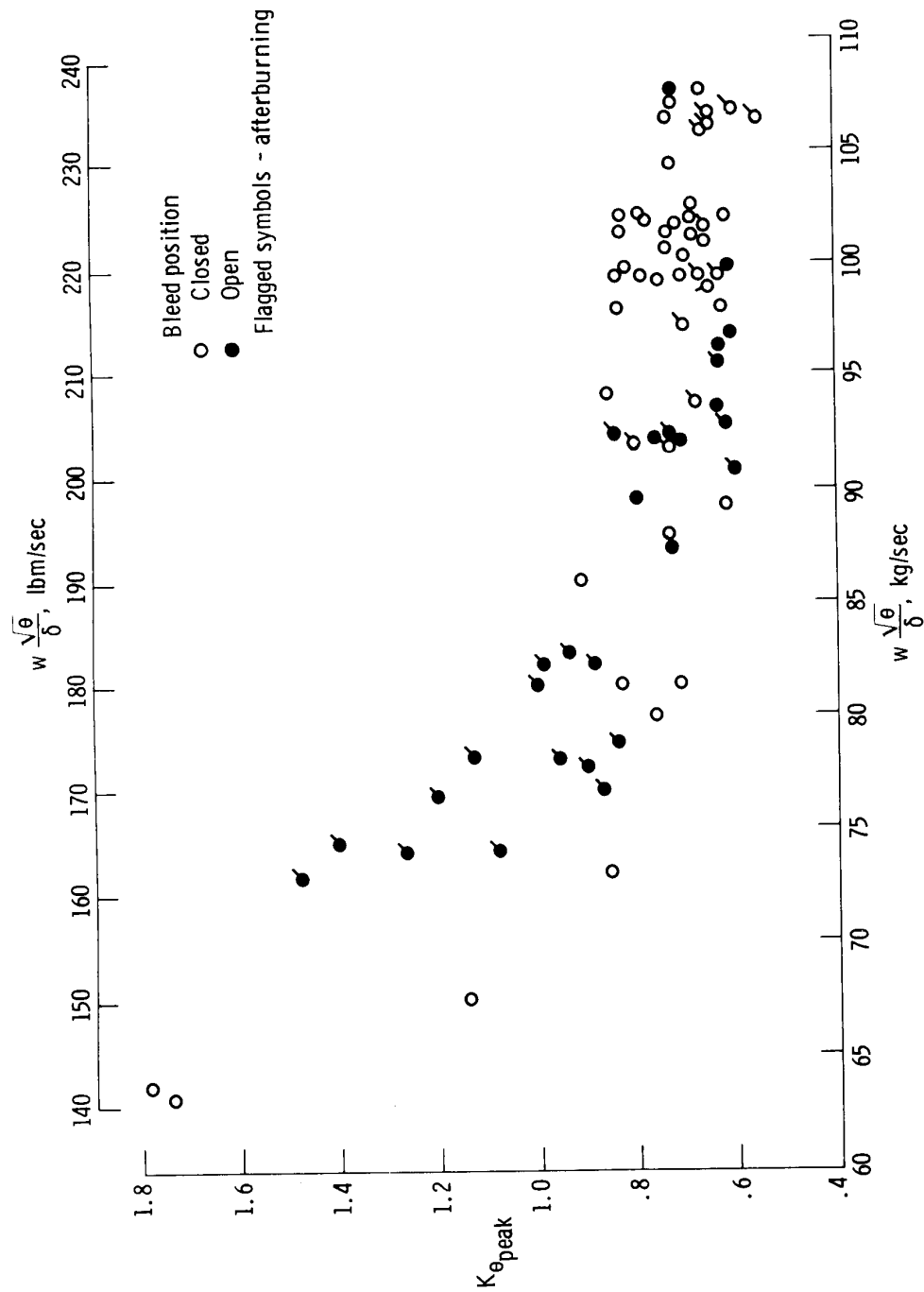


Figure 43. Effect of corrected airflow on peak instantaneous  $K_{\theta}$  prior to stall. F-111A number 12.

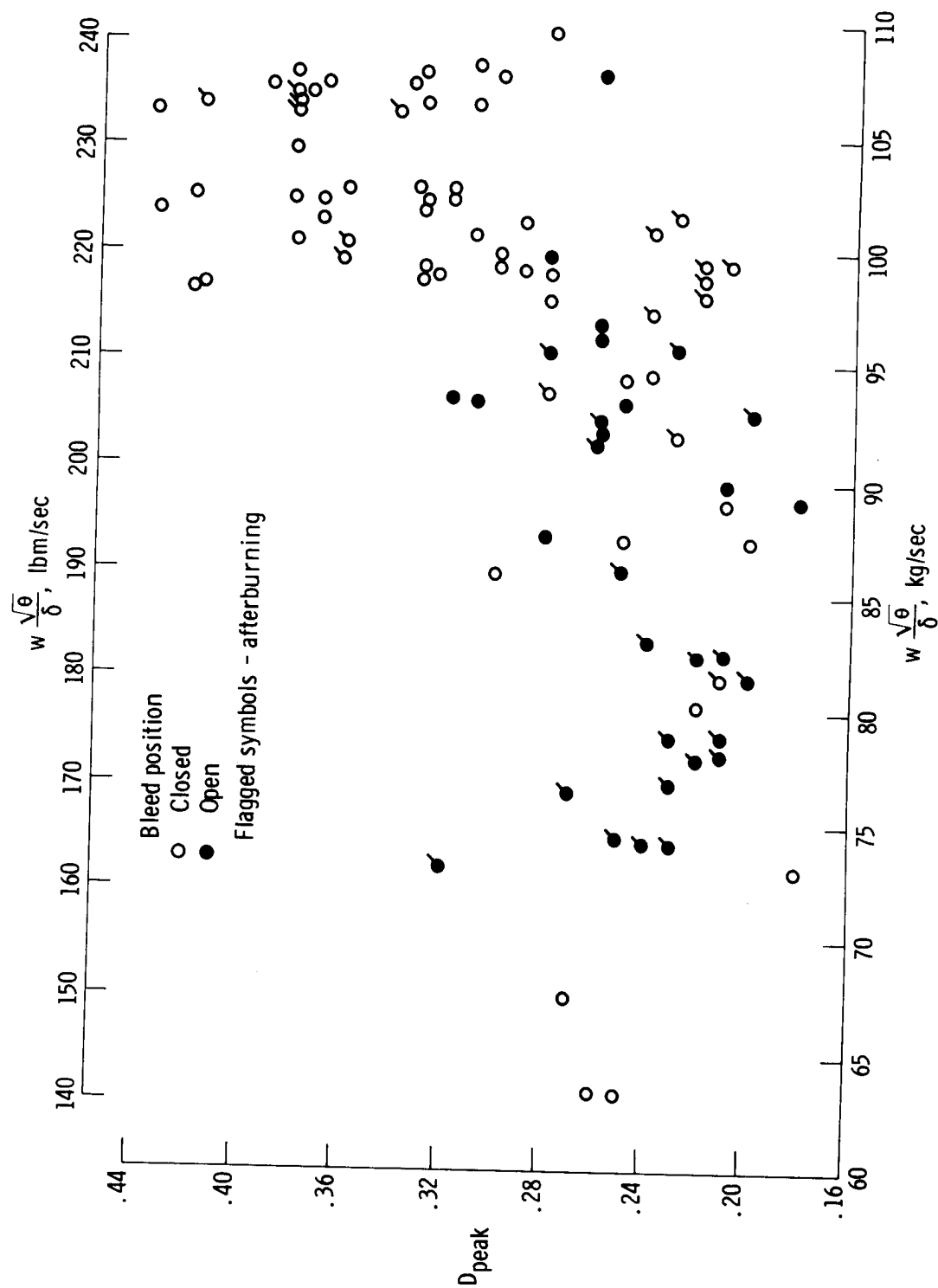
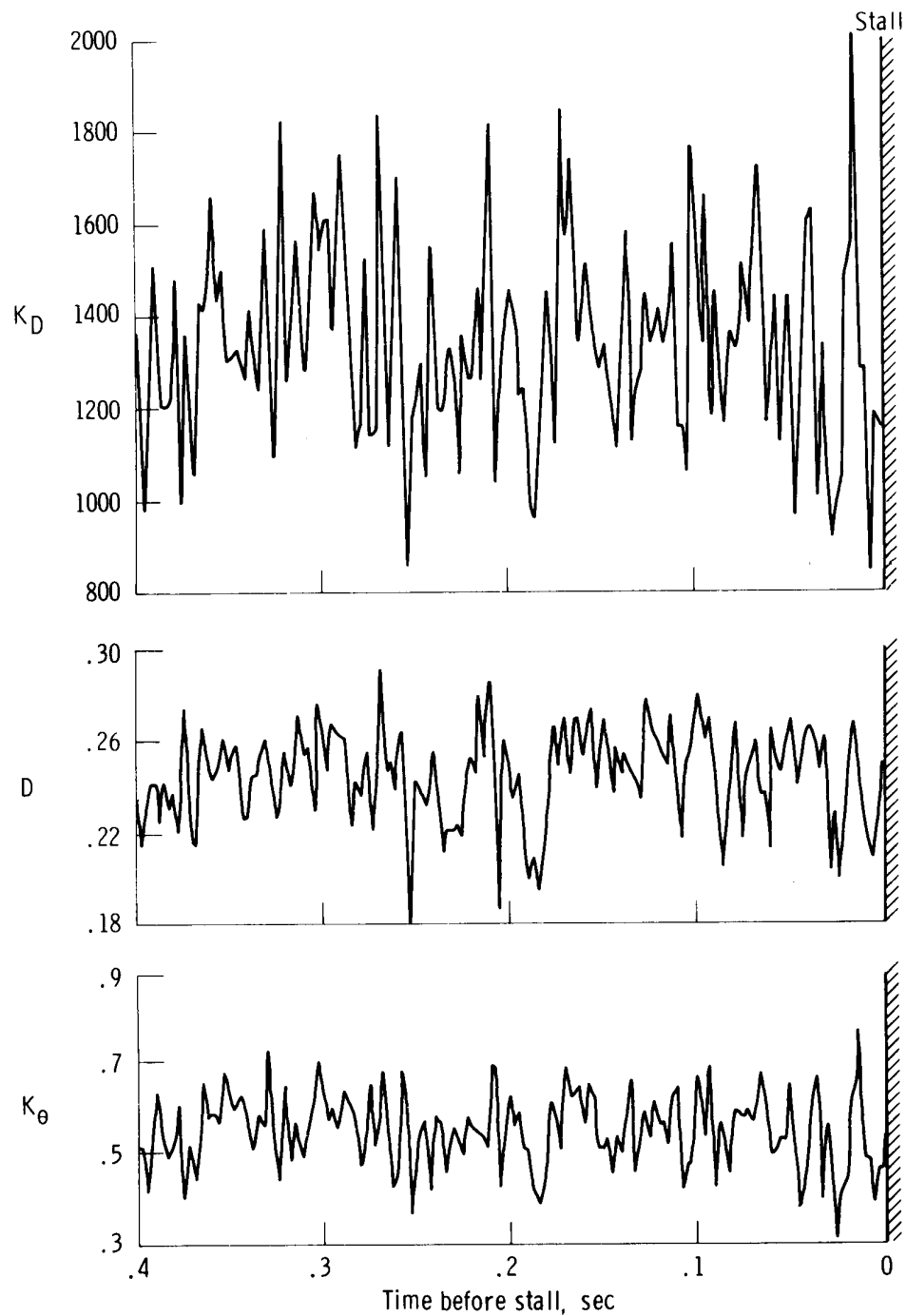
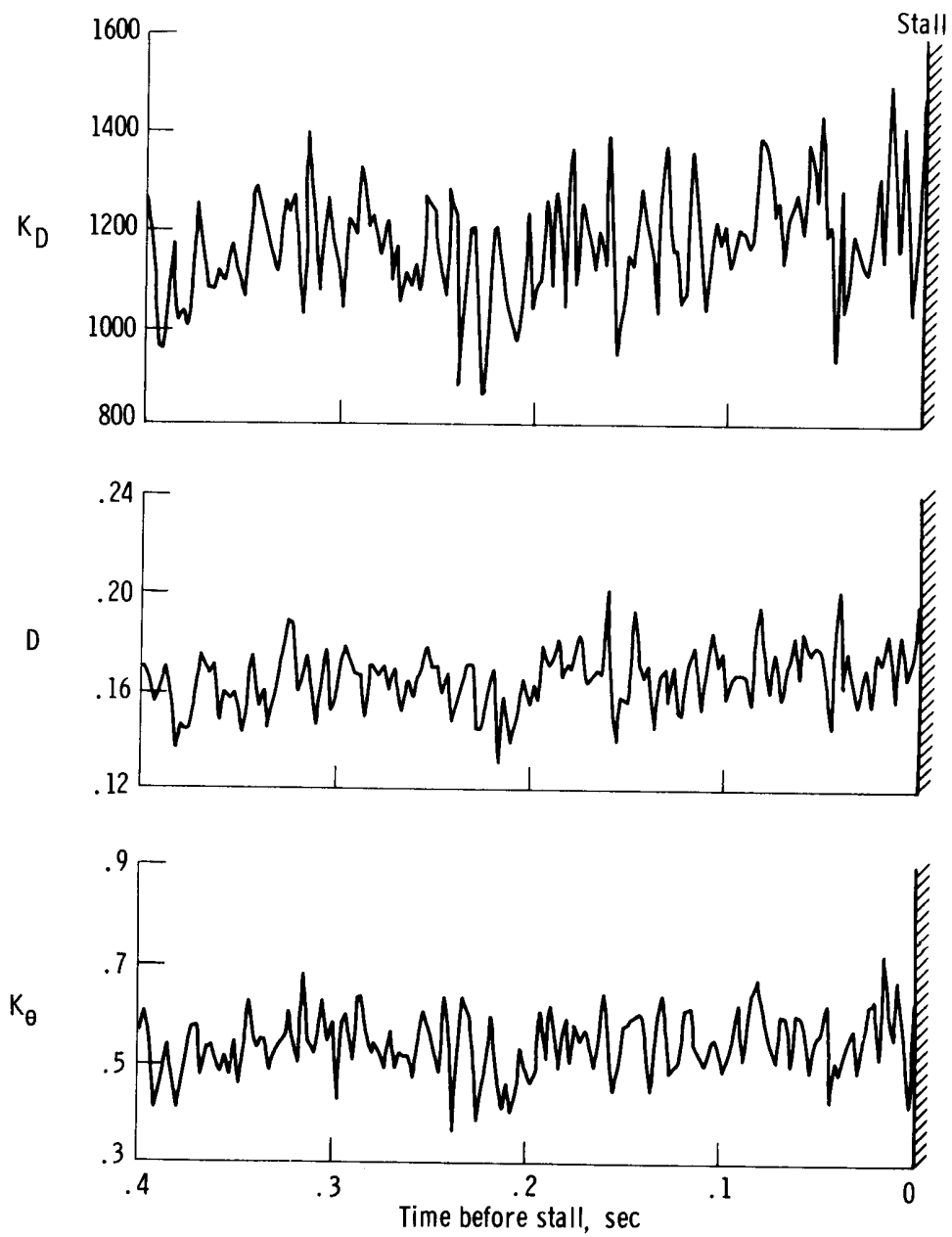


Figure 44. Effect of corrected airflow on peak instantaneous  $D$  prior to stall. F-111A number 12.



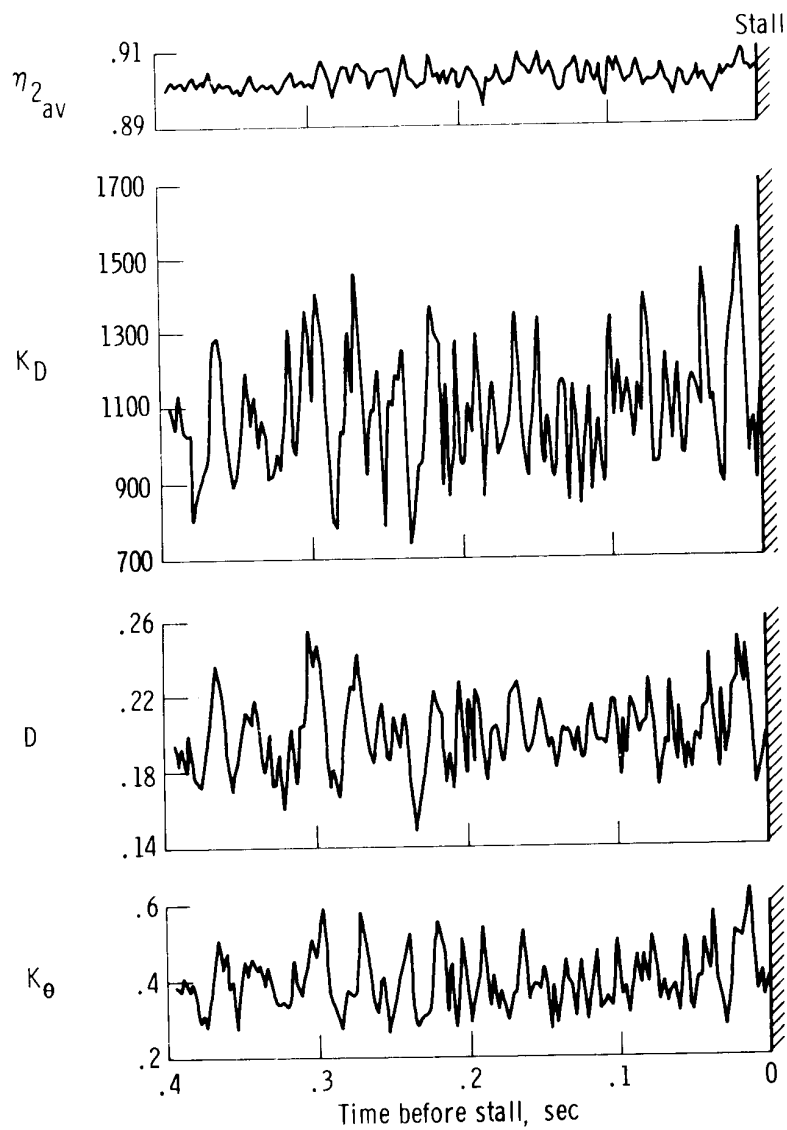
(a) Military power;  $M_\infty = 0.9$ ;  $h = 3,050$  meters (10,000 feet);  
 $Tu_{av} = 0.024$ .

Figure 45. Time histories of instantaneous  $K_D$ ,  $D$ , and  $K_\theta$  just prior to a compressor stall. Subsonic flight; F-111A number 12.



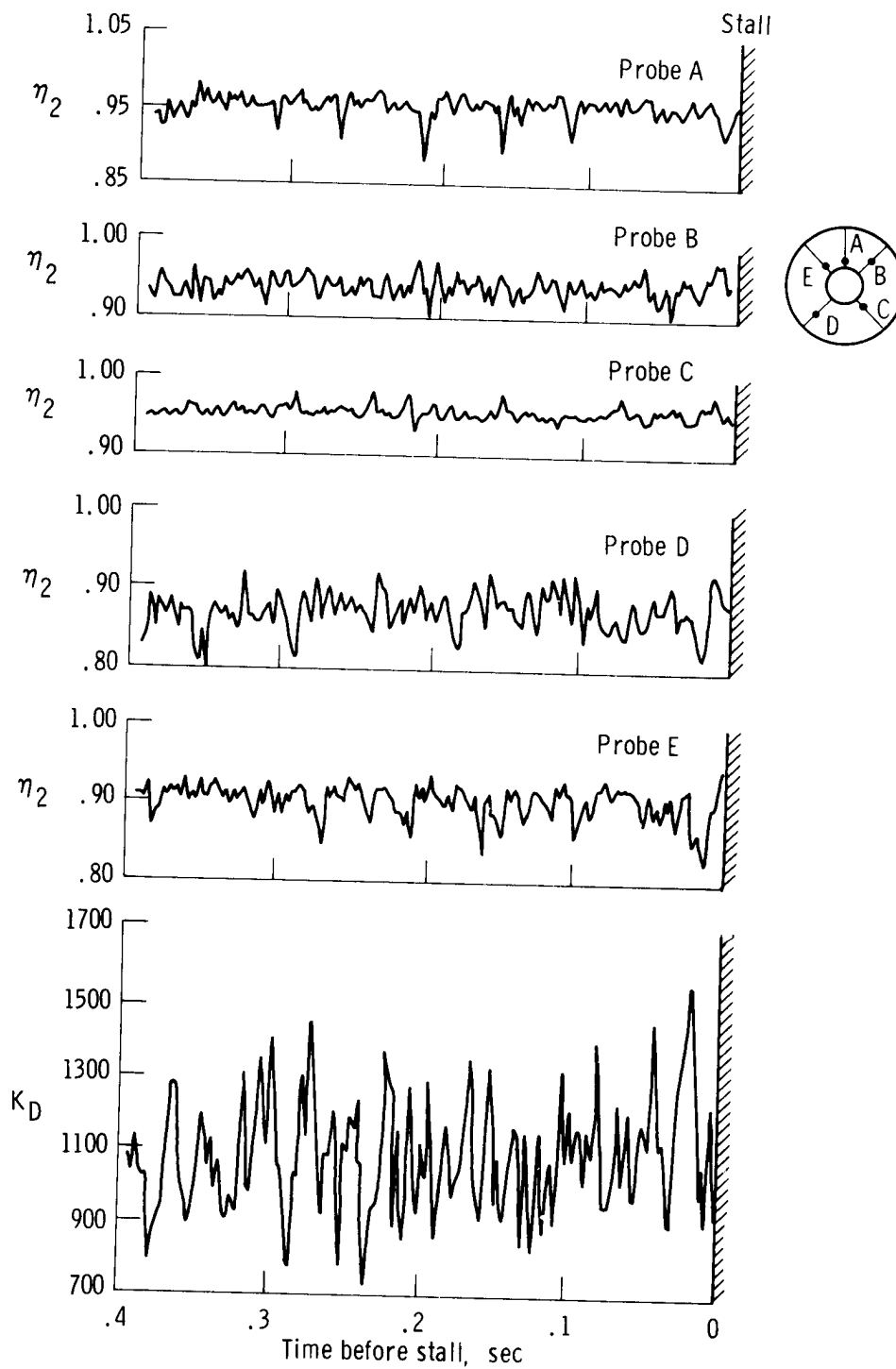
(b) Partial power;  $M_\infty = 0.7$ ;  $h = 9,150$  meters (30,000 feet);  $Tu = 0.015$ .

Figure 45. Concluded.



(a) Time histories of  $\eta_{2_{av}}$ ,  $K_D$ ,  $D$ , and  $K_\theta$ .

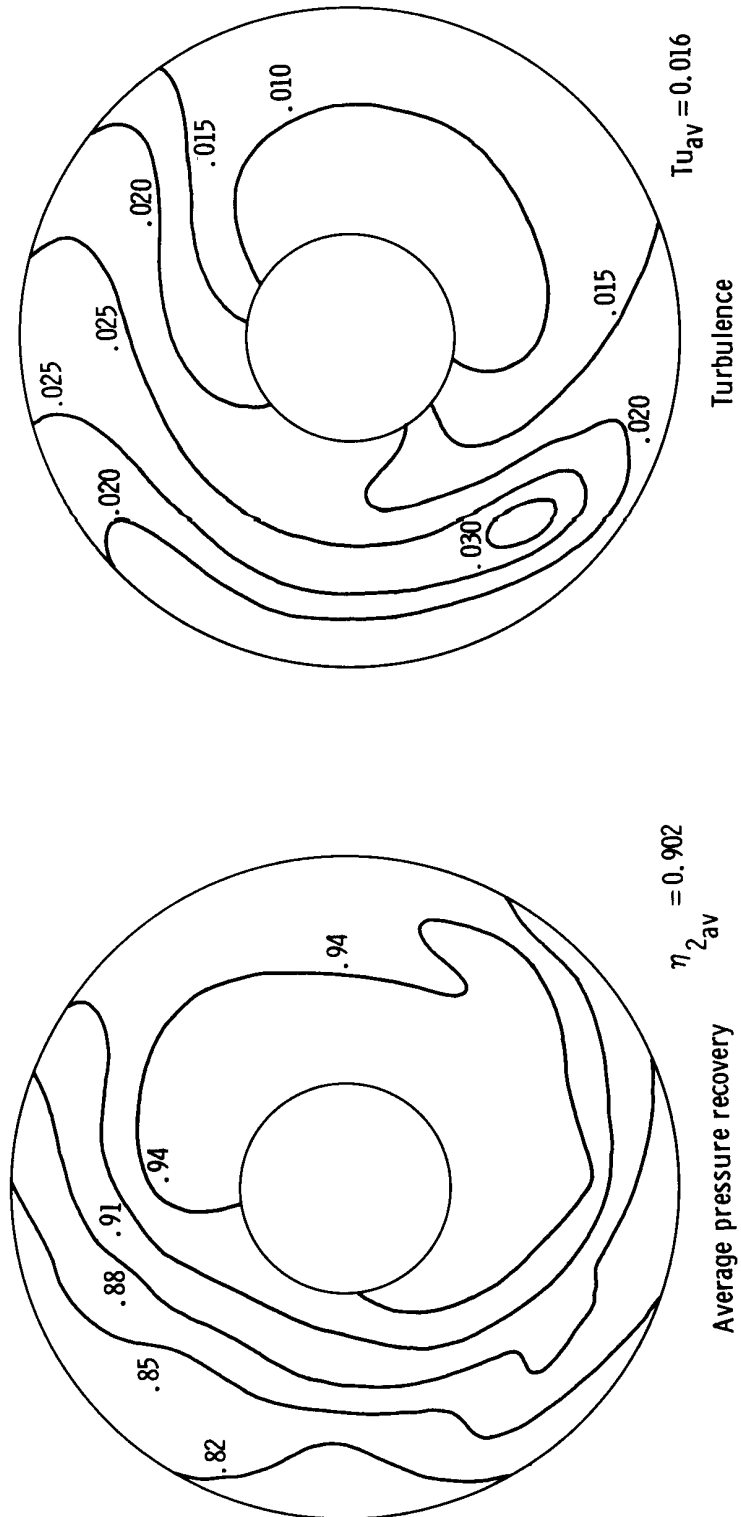
Figure 46. Inlet performance leading to stall during forward spike movement. Maximum afterburning;  $M_\infty = 1.7$ ;  $h = 13,700$  meters (45,000 feet); F-111A number 12.



(b) Comparison of time histories of compressor face pressure probe recoveries with  $K_D$ .

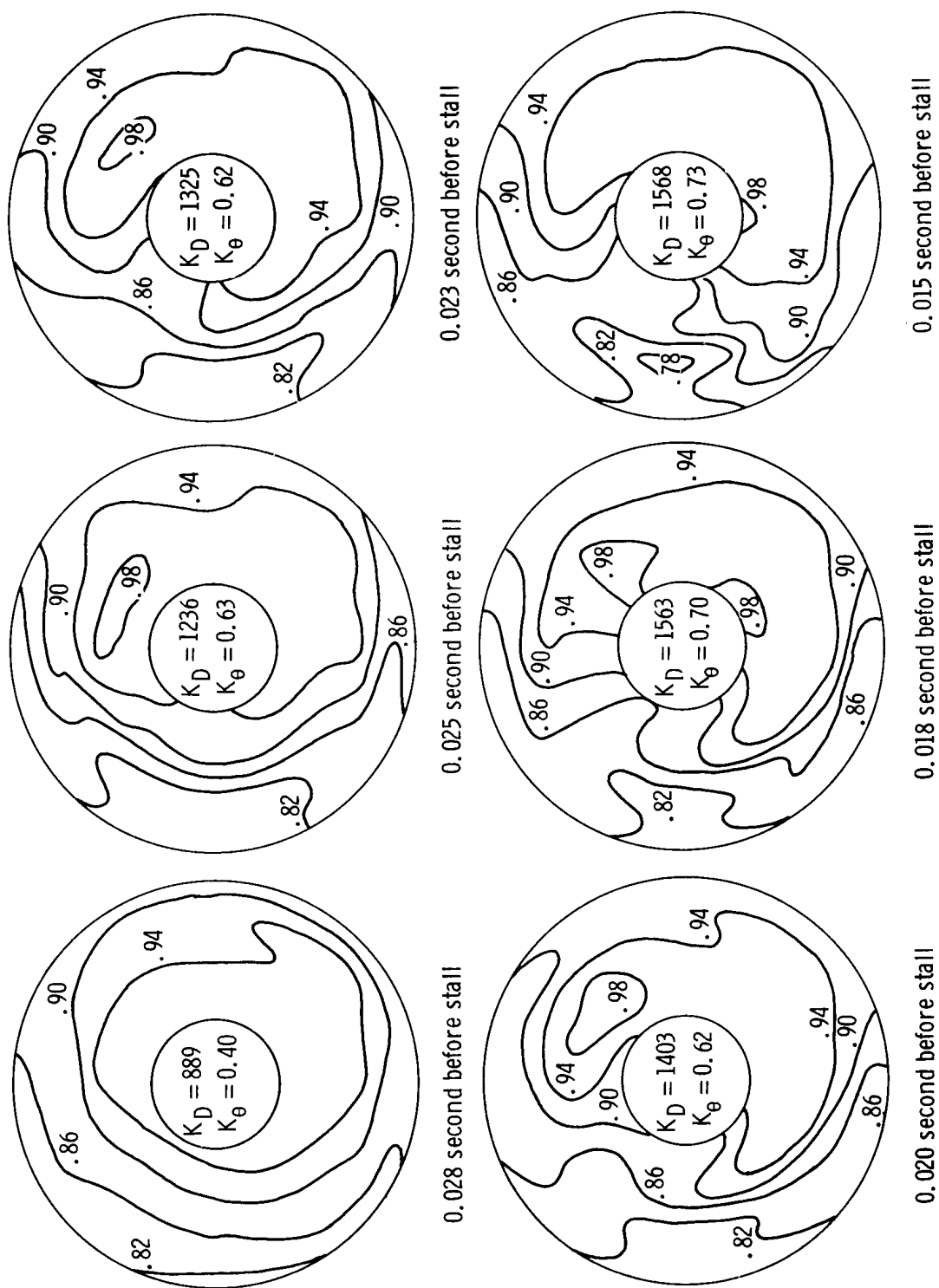
Figure 46. Continued.





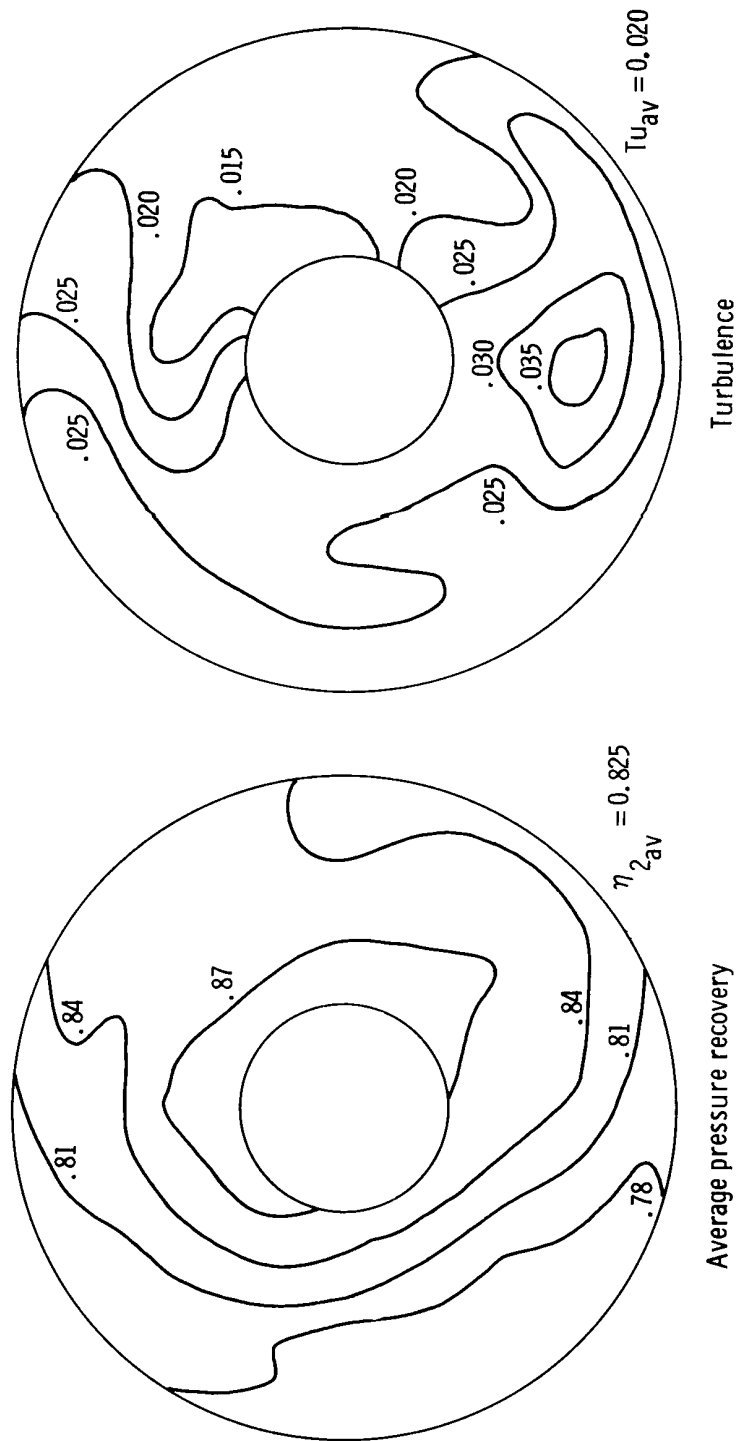
(c) Maps of average compressor face pressure recovery and turbulence prior to stall.

Figure 46. Continued.



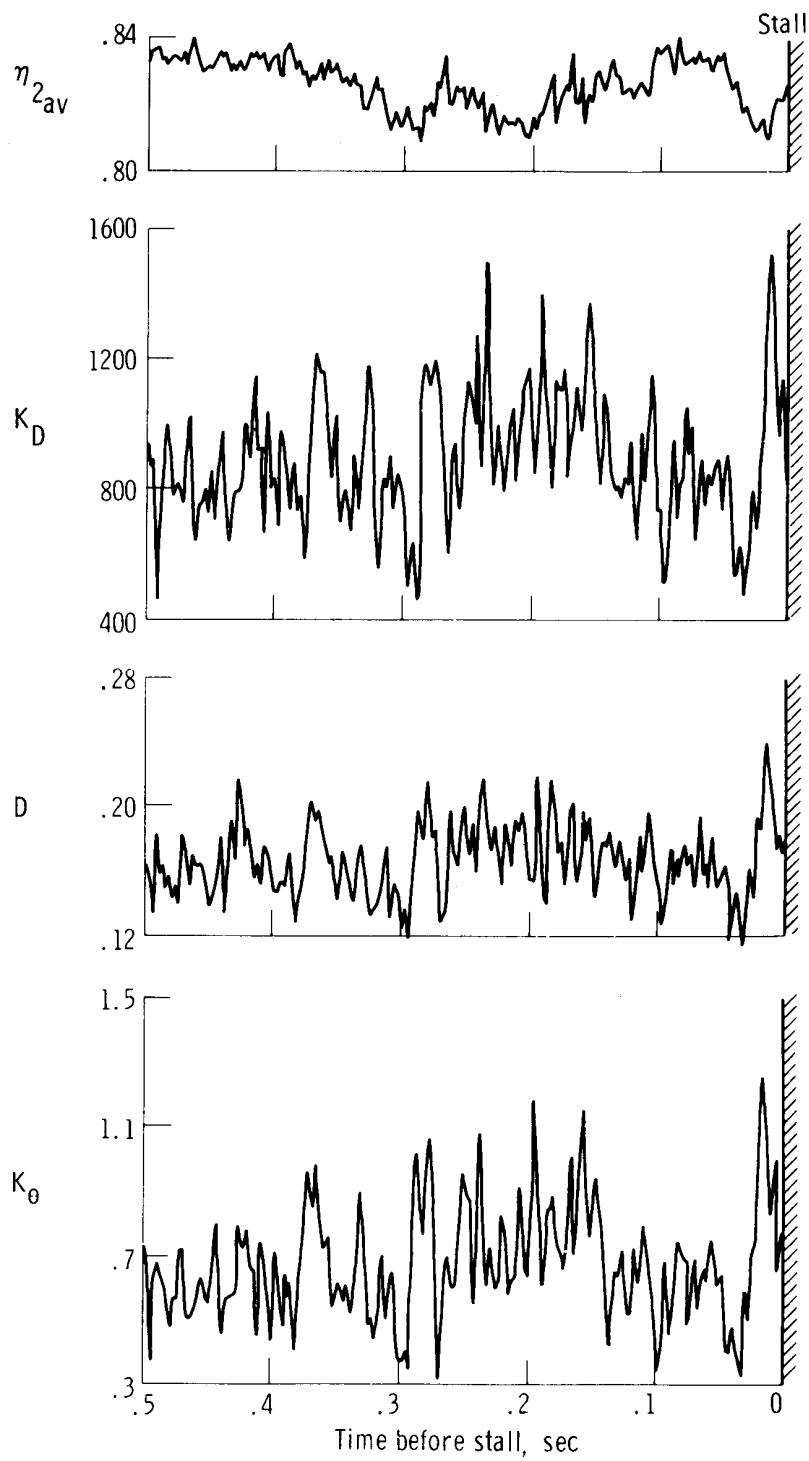
(d) Instantaneous compressor face pressure recovery maps prior to stall.

Figure 46. Concluded.



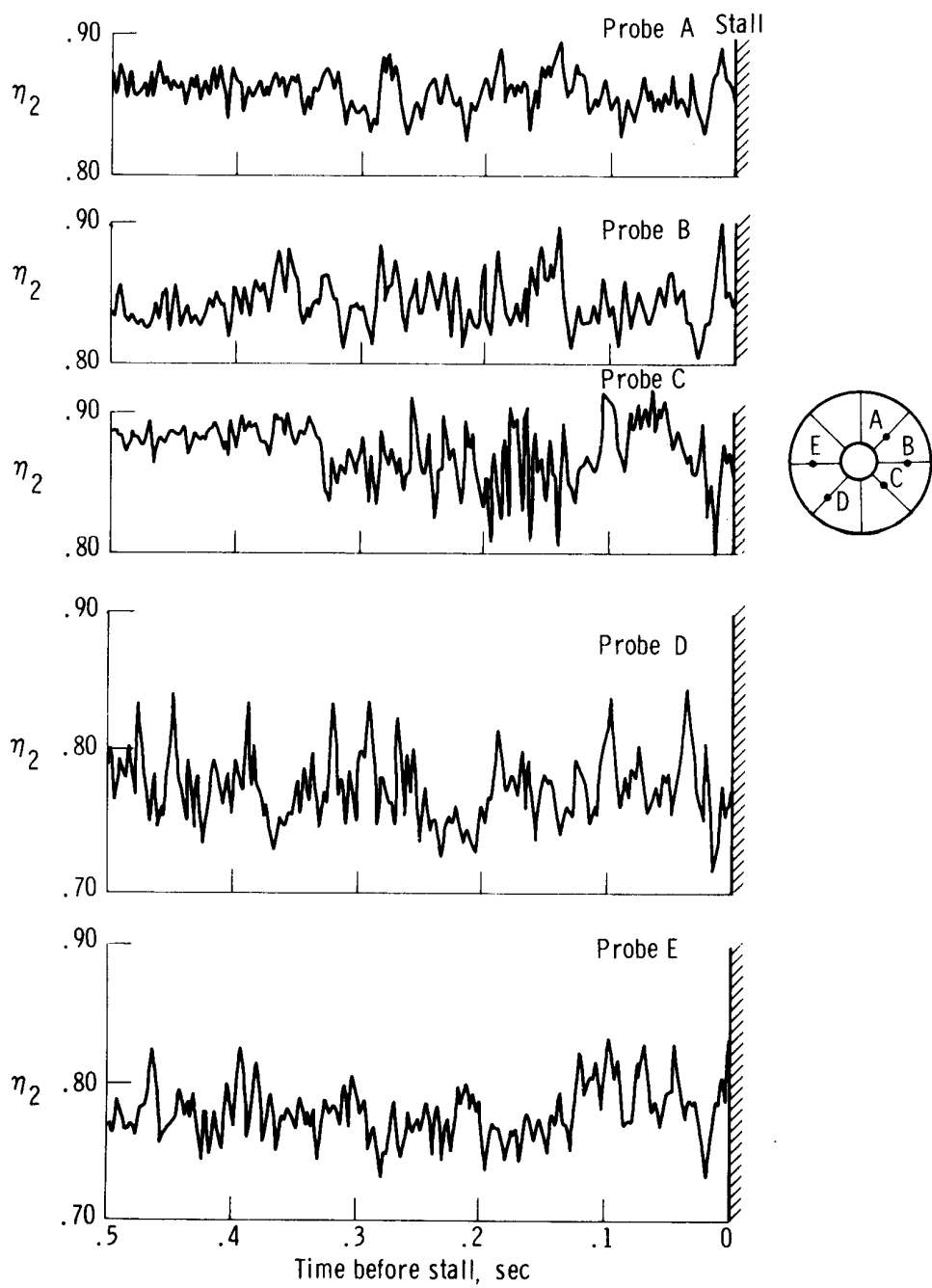
(a) Maps of average compressor face pressure recovery and turbulence prior to stall .

Figure 47. Inlet performance prior to unintentional compressor stall. Maximum afterburning;  $M_\infty = 2.22$ ;  $h = 13,700$  meters (45,000 feet); bleeds open; F-111A number 12.



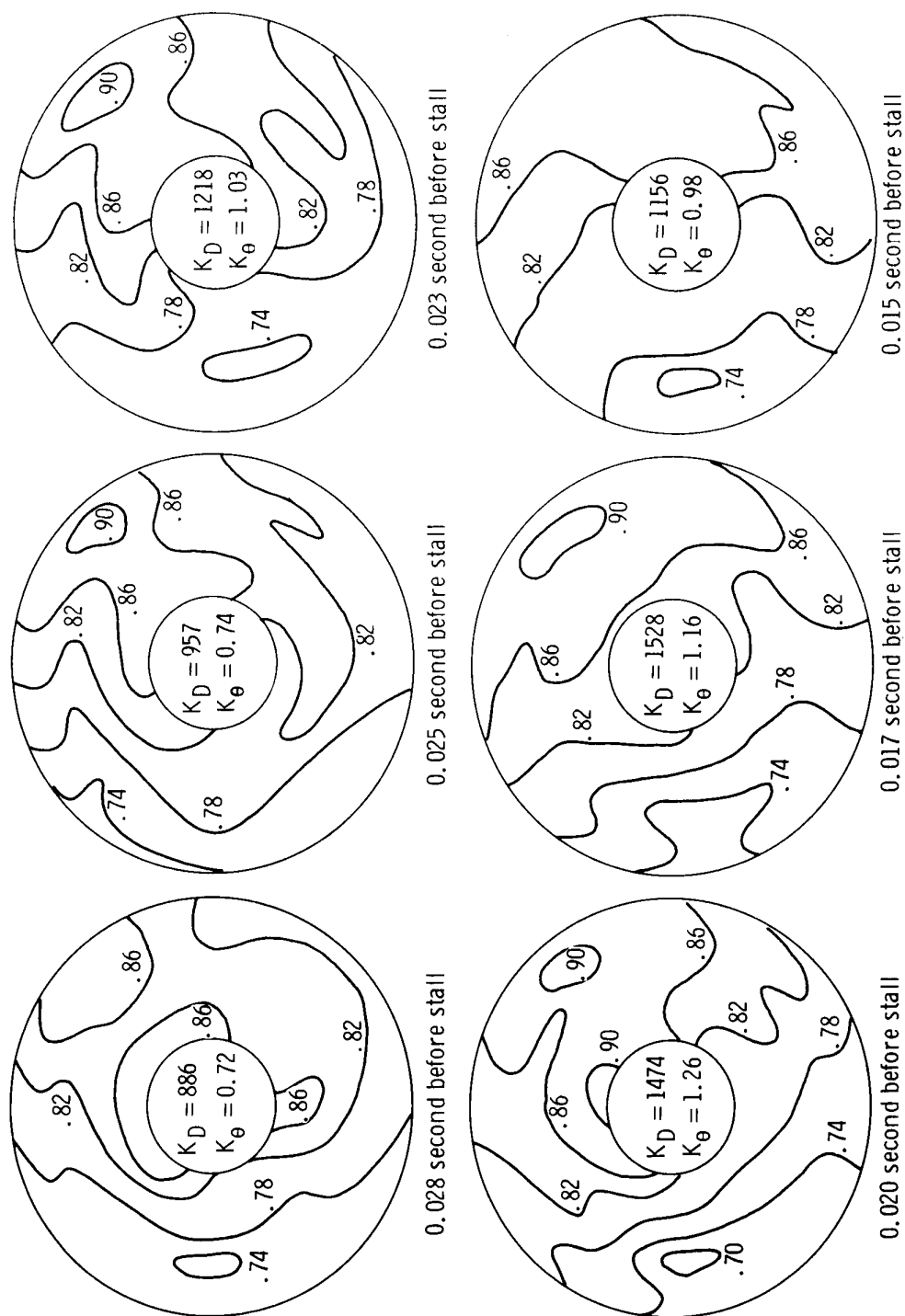
(b) Time histories of  $\eta_{2av}$  and instantaneous distortion factors.

Figure 47. Continued.



(c) Time histories of compressor face pressure probe recoveries prior to stall.

Figure 47. Continued.



(d) Instantaneous compressor face pressure recovery maps .

Figure 47. Concluded .

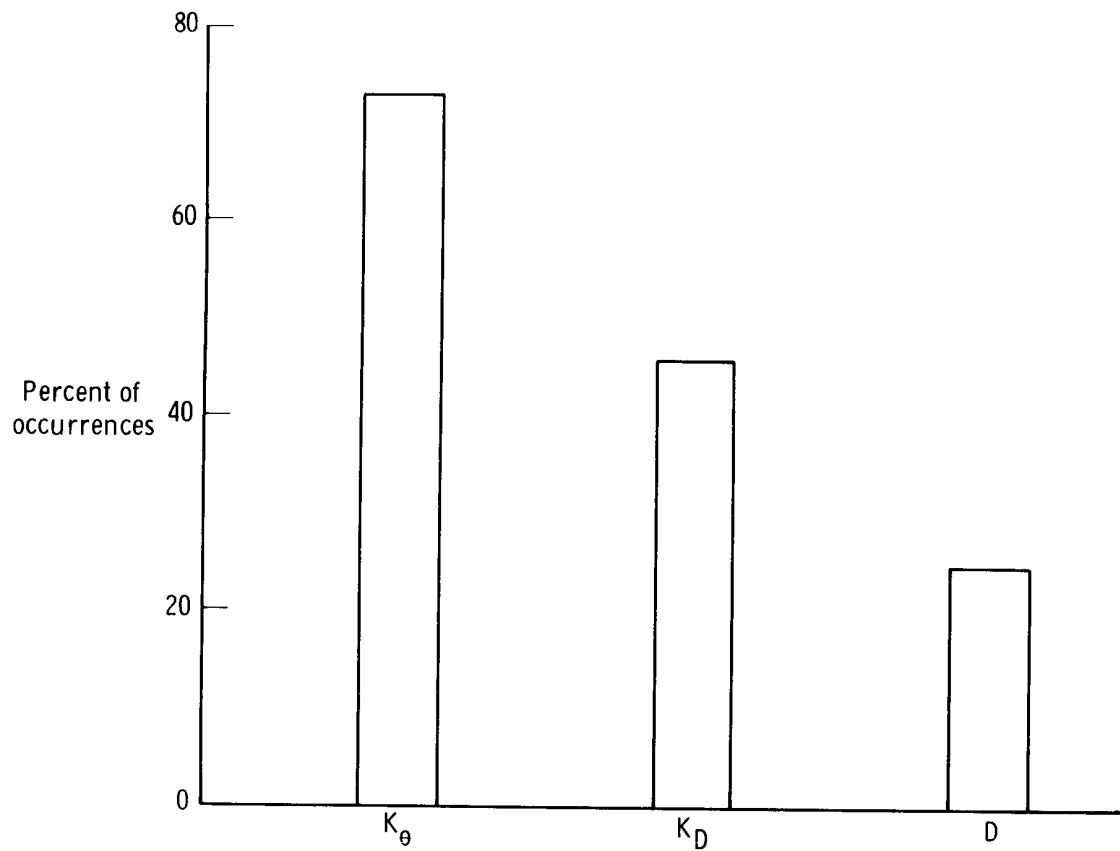


Figure 48. Comparison of the ratio of distortion at stall initiation to the peak distortion for  $K_\theta$ ,  $K_D$ , and  $D$  showing the percent of occurrences where the stall initiation peak value was equal to or greater than any previous peak values.

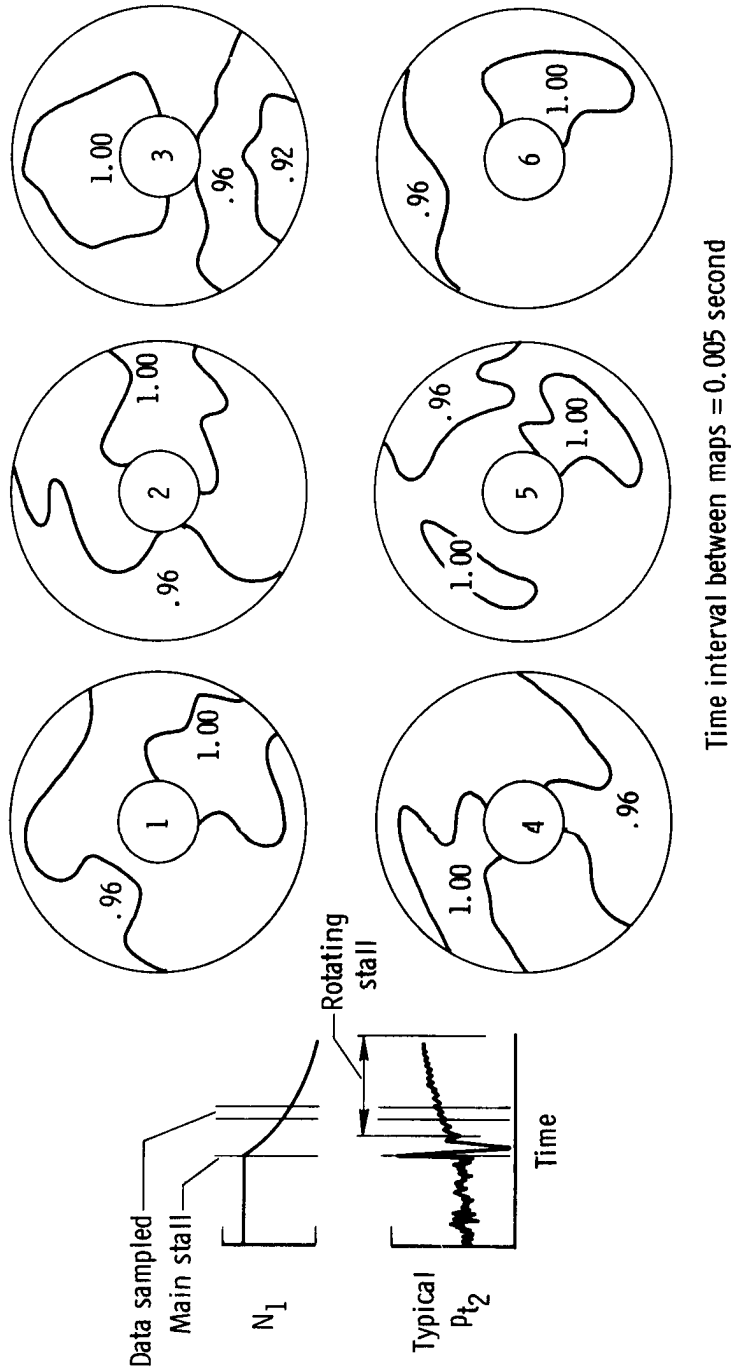


Figure 49. Compressor face instantaneous pressure recovery maps during rotating stall after main engine stall.  $M_\infty = 0.9$ ; F-111A number 12.



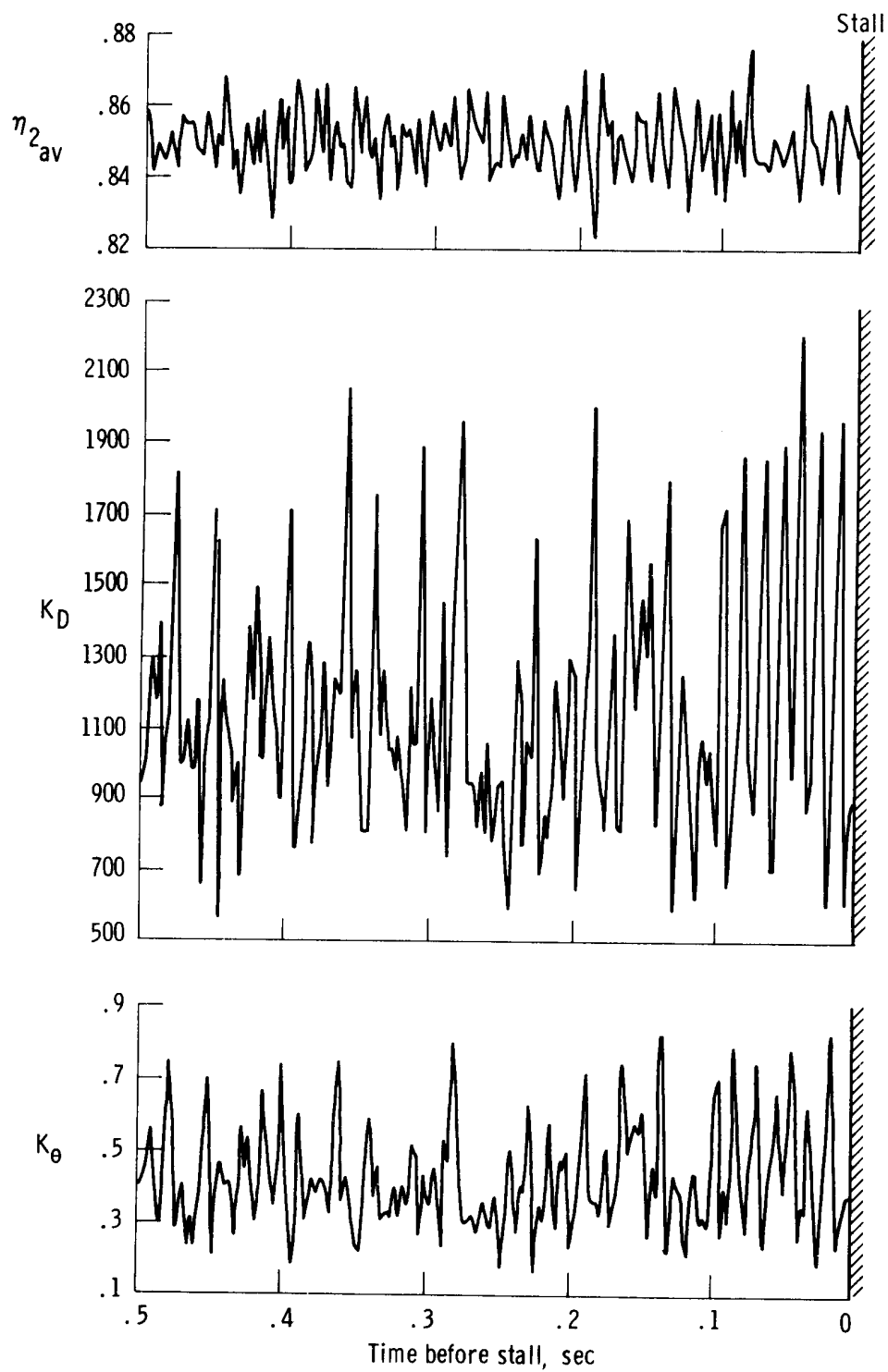
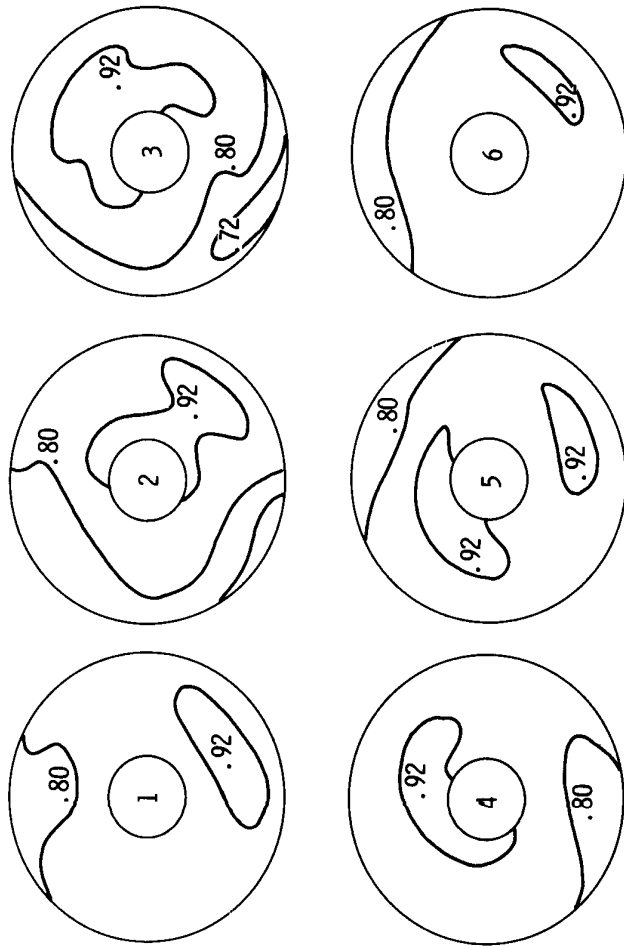
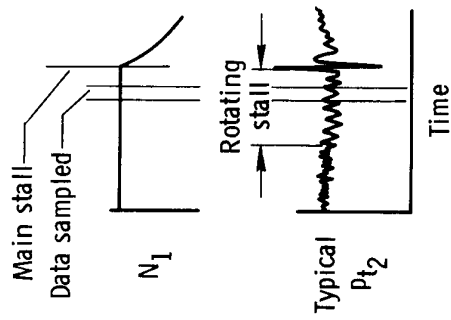


Figure 50. Effect of rotating stall prior to main engine stall on  $\eta_{2_{av}}$ ,  $K_D$ , and  $K_\theta$  caused by expanding the inlet cone.  $M_\infty = 0.9$ ;  $Tu_{av} = 0.047$ ; F-111A number 12.



Time interval between maps = 0.0025 second

Figure 51. Compressor face instantaneous pressure recovery maps during rotating stall prior to main engine stall.  $M_\infty = 0.92$ ; F-111A number 12.

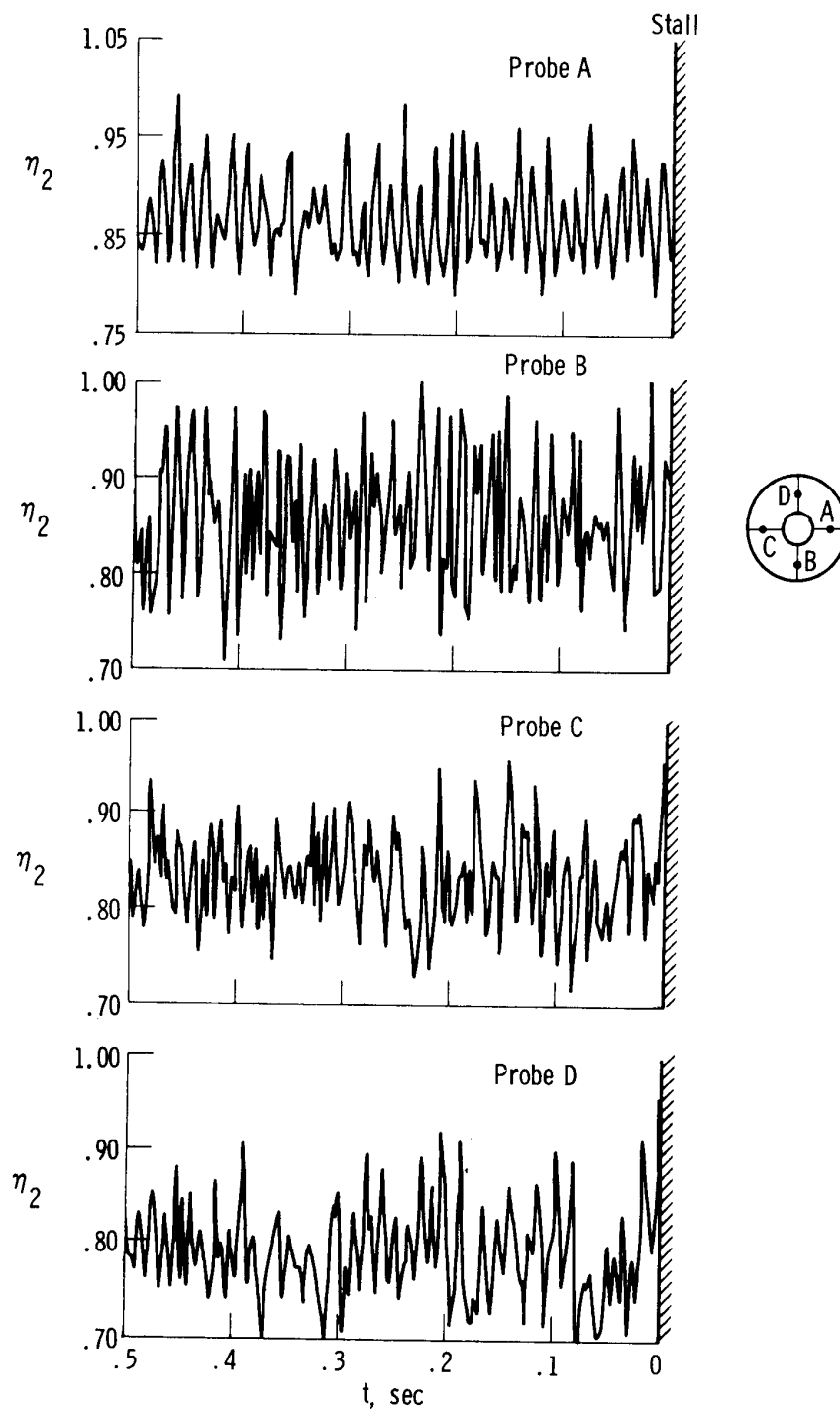


Figure 52. Time histories of compressor face pressure recoveries during rotating stall prior to main engine stall.  $M_\infty = 0.92$ ; F-111A number 12.

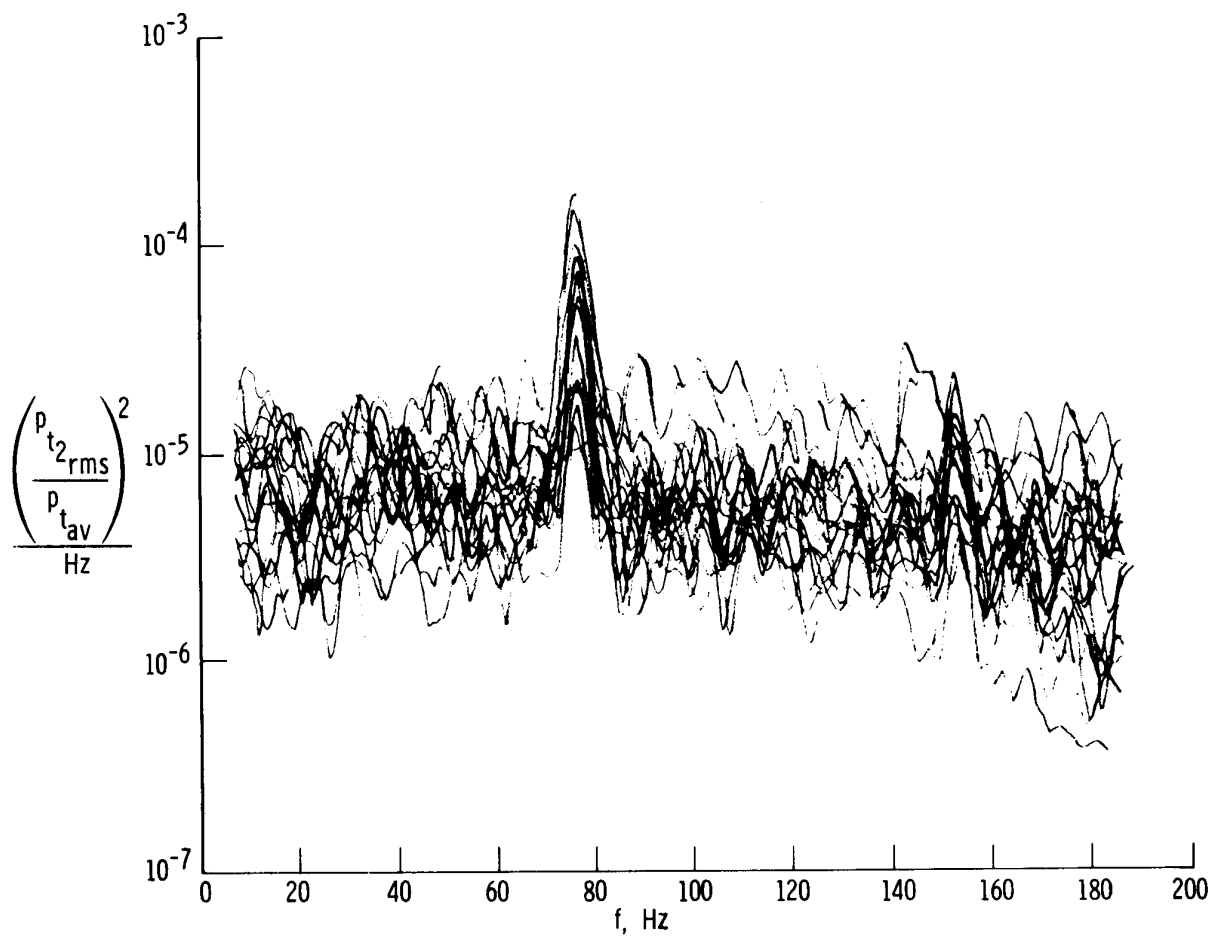


Figure 53. Power spectral density plots of compressor face pressures during rotating stall prior to main engine stall.  $M_{\infty} = 0.92$ ; F-111A number 12.

Source	Fundamental hertz	Harmonics, Hz				
		1	2	3	4	5
Duct resonance	27	54	81	--	--	--
Low rotor speed	145	290	435	580	725	870
High rotor speed	240	480	720	--	--	--
Electrical power	400	800	--	--	--	--

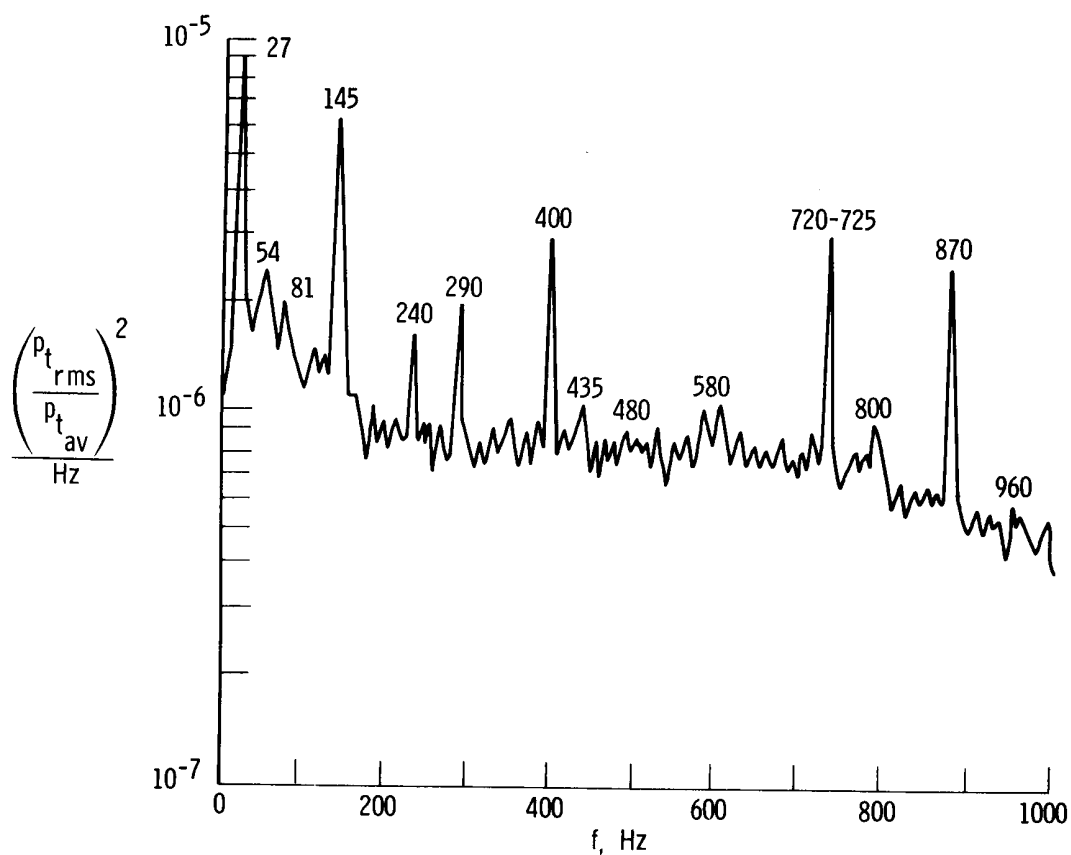
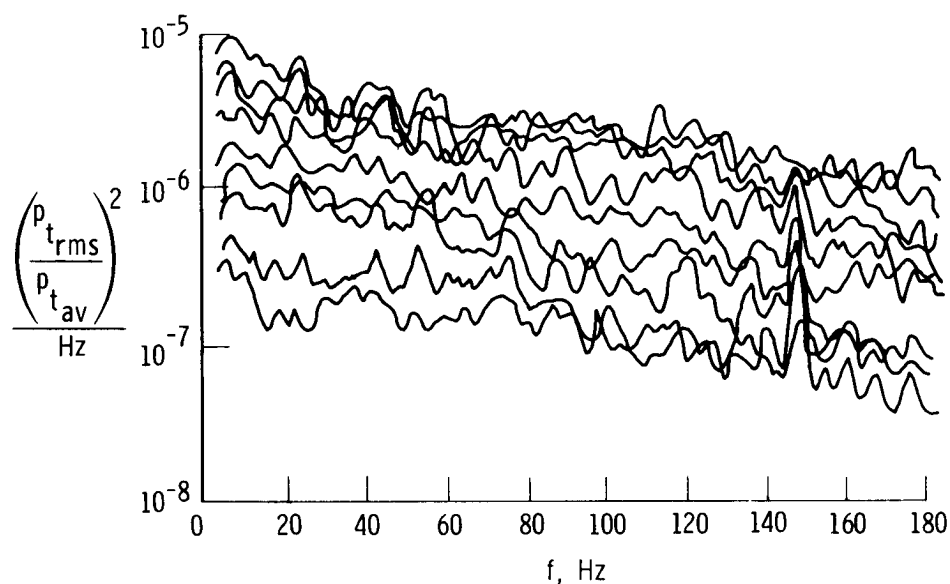
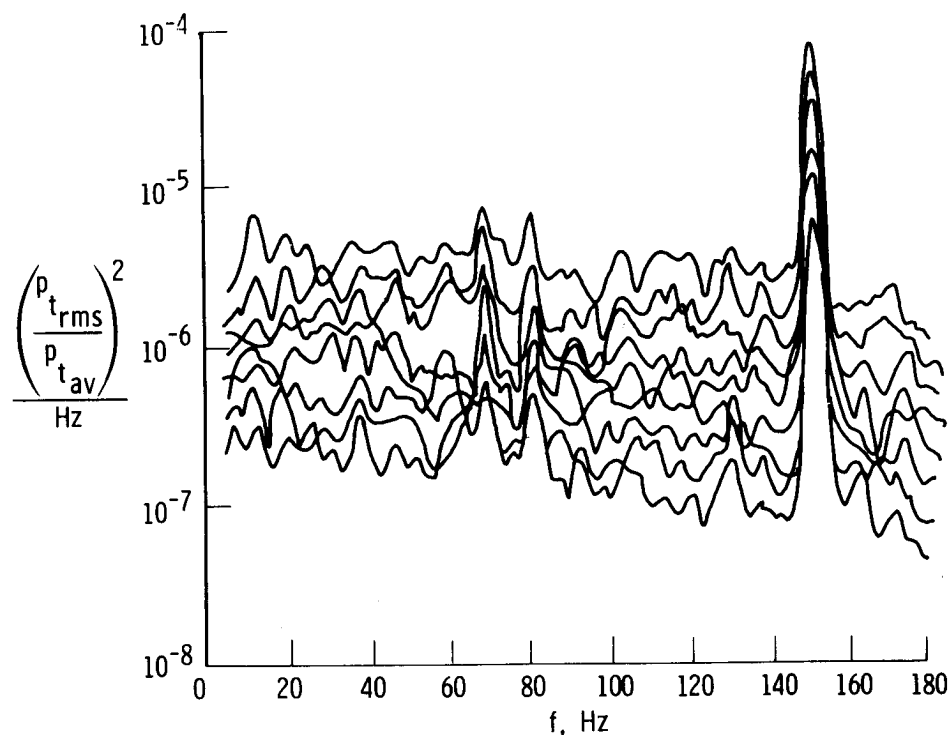


Figure 54. Analog power spectral density plot of a compressor face total pressure showing various peaks caused by duct resonance, rotor speeds, and power supply.  $M_\infty = 2.00$ ; F-111A number 6.



(a)  $h = 11,000$  meters (36,000 feet);  $T_{t_2} = 366^\circ\text{K}$  ( $659^\circ\text{R}$ );  $N_1 = 147$  rps.



(b)  $h = 13,700$  meters (45,000 feet);  $T_{t_2} = 350^\circ\text{K}$  ( $630^\circ\text{R}$ );  $N_1 = 152$  rps;  
 $N_2 = 234$  rps;  $N_2 - N_1 = 82$  rps;  $2N_1 - N_2 = 70$  rps.

Figure 55. Power spectral density plot of typical compressor face pressures showing rotor speed frequencies.  $M_\infty = 1.83$ ; F-111A number 12.